PART I

AN INVESTIGATION OF SHOCK STRENGTHENING IN A CONICAL, CONVERGENT CHANNEL

PART II

SPECTROSCOPIC INVESTIGATION OF STRONG SHOCKWAVES IN A CONICAL, CONVERGENT CHANNEL

Thesis by

Erik Storm

In Partial Fulfillment of the Requirements
For the Degree of
Doctor of Philosophy

California Institute of Technology
Pasadena, California
1972
(Submitted June 1, 1972)

To
Three Beautiful Ladies
Gale
Tania
Cristien

ACKNOWLEDGEMENT

The successful completion of the present research was greatly aided by the intellectual and physical contributions of many people, not the least of which was due to my advisor, Professor Bradford Sturtevant. His constructive criticism over the many years, combined with the proper amount of laissez faire policy provided the main motivation towards the completion of this thesis.

It is a pleasure to acknowledge my appreciation to Professors Hans Wolfgang Liepmann, Anatol Roshko and Donald Coles, the value of the many discussions with them can hardly be overestimated.

Special thanks go to Professor Gerald Whitham for his helpful suggestions during the investigation of the theoretical shock diffraction problem, and to Dr. Robert Setchell for both providing the shock velocity measurements to compare with the theory, and for his literary efforts in part I.

It is a pleasure to thank Mr. Lewis Balthasar and Mr. Ray Wagoner who tutored the author on the finer points of technicianship, and Mrs. Jacquelyn Beard for typing, retyping and retyping the many 'final', as well as *the* final version of the manuscript.

The author is indebted to the California Institute of Technology and the National Aeronautics and Space Administration for their generosity in financial assistance. The work in the 6" shock tube was supported by the National Aeronautics and Space Administration.

ABSTRACT OF PART I

The behavior of an initially plane, strong shock wave propagating into a conical convergence is investigated experimentally and theoretically. In the experiment a 10° half-angle cone is mounted on the end of a pressure-driven shock tube. Shock waves with initial Mach numbers varying from 6.0 to 10.2 are generated in argon at a pressure of 1.5 torr. During each run local shock velocities at several positions along the cone axis are measured using a thin, multi-crystal piezoelectric probe inserted from the vertex. This technique produces accurate velocity data for both the incident and reflected shock waves. In the corresponding analysis, a simplified characteristics method is used to obtain an approximate solution of the axisymmetric diffraction equations derived by Whitham (1959).

Both the shock velocity measurements and the axisymmetric diffraction solution confirm that the incident shock behavior is dominated by cyclic diffraction processes which originate at the entrance of the cone. Each diffraction cycle is characterized by Mach reflection on the cone wall followed by Mach reflection on the axis. These cycles evidently persist until the shock reaches the cone vertex, where the measured velocity has increased by as much as a factor of three. Real-gas effects, enhanced in the experiment by increasing the initial Mach number and decreasing the pressure, apparently alter the shock wave behavior only in the region near the vertex. Velocity measurements for the reflected shock within the cone show that the shock velocity is nearly constant throughout most of the convergence length.

ABSTRACT OF PART II

The thermodynamic conditions behind the incident and reflected shock wave close to the vertex of a convergent channel are investigated spectroscopically. The investigation was initiated in order to better determine the possible uses of such a geometrical device as a tool for high temperature plasma research. Using argon at an initial pressure of 1.5 torr, the shock Mach number prior to the entrance of the cone is 10.2. Two windows are mounted at $x/l = 0.9$ in the cone, where the Mach number has increased to 24, and the emitted radiation is monitored for both time-resolved (Monochromator - Photomultiplier) and time-integrated (Spectrograph) analysis. The relative line intensity method is used to measure the electron temperature. The Stark broadened profile of the 6965.4 Å neutral argon line, and continuum intensity measurements are used to determine the electron number density.

From initial values of 13200°K and 1.4×10^{17} cm^{-3}, both the electron temperature and number density profiles behind the incident shock are dominated by the previous shock diffraction processes. The general trend is a gradual increase, presumably due to the continuing compression of the gas shocked at successively earlier times. Superimposed upon this is the effect of hot slugs of gas from previous localized regions of very high Mach number. The reflected shock wave heats and compresses the gas even further. The subsequent expansion results in a series of rapid exponential decreases in temperature, density and pressure. Immediately after the reflected shock wave has passed, the gas appears to be in a nonequilibrium state with a population inversion among the upper excited atomic energy levels. There is an indication of the presence of a second reflected wave. The effects of self-absorption on Stark broadened lines is studied. An equation is derived, demonstrating the effect of individual corrections that are necessary before accurate interpretations of measured quantities can be made. Simple self-absorption correction schemes are demonstrated and shown to be self-consistent.

TABLE OF CONTENTS

TABLE OF CONTENTS (cont.)

TABLE OF CONTENTS (cont.)

TABLE OF CONTENTS (cont.)

Appendices

LIST OF FIGURES

PART I

AN INVESTIGATION OF SHOCK STRENGTHENING IN A CONICAL, CONVERGENT CHANNEL

By

Robert E. Setchell

Erik Storm *

and Bradford Sturtevant

---

* The theoretical investigation was conducted by Erik Storm

I. 1 INTRODUCTION

A shock wave propagating into a gradually converging channel experiences a progressive strengthening. This behavior is illustrated in figure 1, which depicts both the incident and reflected shock trajectories in a closed conical convergence. The earliest analysis of such a shock motion is the similarity solution of Guderley (1942) for converging cylindrical or spherical shock waves. This solution, later reworked with improved accuracy by Butler (1954), predicts a power-law increase in Mach number as the shock approaches the axis or point of symmetry. At the instant of shock collapse the solution is singular, but the subsequent reflected shock motion again follows a simple power law. Chisnell (1957) extended the linearized analysis of Chester (1954) to obtain an approximate, one-dimensional solution for local shock strength in channels with slowly changing cross-sectional areas. Whitham (1958) obtained an identical solution in an original manner by applying a simplified characteristics method. The Chester-Chisnell-Whitham formulation (hereafter referred to as "CCW theory") similarly predicts a a power-law increase in the Mach number of a strong shock wave as the surface area of the shock decreases. The power-law exponents found for wedge-shaped and conical channels closely agree with the exponents found in the similarity analysis for converging cylindrical and spherical shocks, respectively. Application of the CCW theory is restricted, however, by the assumption that the interaction between the shock wave and the converging channel is one-dimensional. In an experimental investigation involving a convergence mounted on a conventional shock tube, the possibility exists for shock diffraction at a discontinuity in wall slope. Whitham (1957, 1959) developed general equations for shock diffraction problems, and his two dimensional solution for diffraction by a wedge indicates that Mach reflection will occur at the entrance of a wedge-shaped or conical channel. The effect of this initial diffraction on the subsequent shock motion within the convergence remained to be determined.

The few experimental investigations into this shock behavior have been conducted using various contractions placed on standard shock tubes. Conclusions from these efforts were limited by a general inability to accurately measure shock velocities within the converging channel. Russell (1967) measured shock velocities in a constant-area channel downstream of a conical convergence, then estimated velocities at the exit of the convergence by extrapolation. His estimated values fell below the predictions of the CCW theory, and this disparity increased with increasing Mach number and decreasing pressure. A schlieren system and drum camera were used by both Bird (1959) and McEwan (1968) to obtain shock trajectories within two-dimensional convergences. Local shock velocities were estimated from the slope of the trajectories, and for smooth, gradual contractions they found values that roughly compared with the predictions of CCW theory[†]. This streak

---

[†] McEwan claimed velocity increases in a parabolic contraction that were greater than CCW theory predictions, and suggested an optimum geometry might be found. Initial investigations into the effects of wall shaping have been made by Milton and Archer (1969), Lau (1971), and Skews (1972).

photograph technique failed to show shock diffraction effects after the initial Mach reflection at the convergence entrance. Belokin' et al. (1965) noted that the diffraction in a wedge-shaped contraction would be a continuing pattern of Mach reflections, but their measurements were restricted to examining thermodynamic conditions near the vertex.

This paper summarizes an experimental and theoretical investigation of the behavior of an initially plane, strong shock wave propagating into a conical convergence. A particular objective of the study was to determine the extent to which the expected diffraction at the entrance affects the subsequent shock motion. Part 2 of the paper is a brief description of the experimental apparatus, which includes a new device for measuring shock velocities within the cone. Part 3 presents complete profiles of incident shock velocity for two cases of low and high initial Mach number. In part 4, an approximate solution of Whitham's axisymmetric diffraction equations is obtained for a converging conical geometry. The description of the incident shock motion provided by this solution is then compared with the measured velocity profiles. The investigation was concluded by examining the reflected shock behavior within the cone, and complete profiles of reflected shock velocity are presented in part 5.

I. 2 EXPERIMENTAL APPARATUS

The experiment was performed using a 10° half-angle conical convergence mounted on the end of a 15.3 cm diameter, pressure-driven shock tube (figure 2). The cone consists of two carefully machined sections, with the final section converging to a minimum diameter of 3.2 mm (an overall area reduction of 2300:1). A 3.2 mm hole remains at the vertex to allow insertion of instrumentation. The initial Mach number of the incident shock wave is measured using conventional, thin-film heat-transfer gauges mounted upstream of the cone entrance.

A new instrument designed to provide accurate shock velocity measurements along the centerline of the cone (Setchell 1971) is shown in figure 3. The probe contains four piezoelectric crystals in the form of cylindrical tubes, each 3.2 mm in diameter and 1 mm in length. The crystals are arranged in two closely-spaced pairs within the 3.2 mm diameter, axisymmetric support structure. The probe is inserted into the cone at the vertex and positioned along the axis of symmetry. The piezoelectric crystals are polarized between the inner and outer diameters; the radial compression produced by the shock pressure jump thus generates a sequence of signals as the shock passes the crystal positions along the probe. The signals are fed directly into two dual-beam oscilloscopes and recorded on polaroid oscillograms. Shock velocities are determined by measuring the time interval between signals produced by the adjacent crystals in each crystal pair. The resolution in measuring the time intervals is sufficient to obtain velocities accurate to 3% or better. The probe was tested in the straight shock tube where reference velocities could be measured with thin-film sidewall gauges; over a range of shock Mach numbers from 5 to 10 the probe-measured velocities were found to be within 1-4% of the reference values.

To obtain a complete shock velocity-versus-distance profile, a large number of runs must be made under identical conditions as the probe position within the cone is varied. The 15.3 cm diameter shock tube can consistently generate shock waves whose Mach numbers are reproducible to within 1% (Smith 1967).

I.3 SHOCK VELOCITY PROFILES

I.3.1 Mach Six Case

For the first shock velocity profile a relatively low initial Mach number and high test-gas pressure were needed to minimize deviations from ideal-gas behavior. Measurements made with an initial Mach number (M_o) of 6.0 in argon at a pressure of 1.5 torr are shown in figure 4. The data reveal that the shock velocity along the cone centerline does not display the gradual, monotonic increase predicted by the one-dimensional CCW theory for a conical channel (Whitham 1958). Instead there are a number of short intervals in which the centerline shock exhibits a very rapid acceleration. In the regions between these sudden jumps the shock first decelerates then accelerates. The measured velocity for the first 30% of the convergence is the same as the initial shock velocity. Near the vertex the velocity has increased by a factor of approximately 3.

The physical interpretation of the measured velocity profile (consistent with the analysis in part 4) is sketched in figure 5. Mach reflection of the initially plane shock occurs on the convergence wall[†], and subsequent diffraction processes continue throughout the length of the cone. The first velocity jump results from the arrival of the three-shock intersection at the cone centerline

---

[†] In Mach reflection the shock strength and propagation direction are discontinuous at the intersection of the original shock, the stem-shock, and the weak reflected shock. The three-shock intersection moves outward from the channel wall as the shock motion progresses.

(indicated by (iii) in the figure). Beyond this point Mach reflection of the stemshock on the cone axis occurs, and a "center shock" progressively grows until it fills the channel cross-sectional area. The process of Mach reflection on the cone wall by Mach reflection of the stemshock on the cone axis is then repeated, and this cycle evidently continues until the shock reaches the vertex.

I. 3. 2 Mach Ten Case

In order to observe the possible influence of "real-gas effects" on the shock diffraction process, a second velocity profile was measured with the initial Mach number increased to 10. 2. The test gas was again argon at a pressure of 1. 5 torr. For these initial conditions, the shock should be sufficiently strengthened after the first diffraction cycle to produce significant ionization in the heated argon. The data are plotted in figure 6, and show the same general features found in the Mach six case until the third stemshock intersection on the cone axis, where local Mach number jumps from 19. 1 to 23. 2. Beyond this point the high Mach number data show a rapid decline in the shock velocity. The jump at the fourth stemshock intersection is very weak, and a fifth intersection is not observed.

I. 3. 3 Variation of Initial Mach Number and Pressure

The shock diffraction theory (discussed in part 4) predicts that the local shock velocity at any particular location within the cone should scale with the initial velocity. Because the theory assumes ideal-gas behavior, a breakdown in this scaling is expected at higher Mach numbers and lower pressures when real-gas effects become important. Figure 7 shows a series of measurements made at fixed locations within the cone while the initial Mach number was varied from 6.0 to 10.2. The initial pressure was either 1.5 torr or 0.5 torr. As expected from the complete velocity profile measurements, no significant scaling variations are observed for a pressure of 1.5 torr except at a position between the third and fourth stemshock intersections (x/L = 0.86). At this location the scaling begins to fail at a local shock Mach number between 18.7 and 19.8. For a pressure of 0.5 torr the measured velocities at the same location are unexpectedly lower and show no variation with initial Mach number. The highest local Mach number measured at this pressure is 21.1.

I. 4 AXISYMMETRIC SHOCK DIFFRACTION SOLUTION

I. 4. 1 Whitham's Diffraction Theory

Whitham (1957, 1959) formulated an approximate theory for shock dynamics problems in which disturbances to the flow are treated as a wave propagation on the shock. In two-dimensional problems the successive shock positions and rays locally normal to these positions are used as orthogonal coordinates. One relation between local shock Mach number and distance between adjacent rays follows from geometry, and a second is obtained from the CCW theory (Whitham 1958) by assuming that adjacent rays act like solid channel walls. Combining the two relations results in a second-order, hyperbolic differential equation which predicts that disturbances on the shock display nonlinear wave motion analogous to waves in one-dimensional, unsteady gas-dynamics. Mach reflection at an inward wall inclination initially appears as a compressive "wave" on the incident shock, but this wave quickly breaks due to the nonlinearity to form a "shock-shock". This shock-shock represents the three-shock intersection characteristic of Mach reflection, and the theory is correct to the extent that the effects of the third (reflected) shock are negligible.

In axisymmetric problems the formulation is basically the same, except conventional cylindrical coordinates (x, r) prove to be more convenient than independent variables based on shock positions and rays. The diffraction geometry and the variables used in the analysis that follows are illustrated in figure 8. The shock surface at a particular time t is described by $a_o t = \alpha(x, r)$, where a_o is the sound speed in the undisturbed gas. If M is the local shock Mach number and $\theta(x, r)$ is the local angle between a ray and the symmetry axis, then

$$\alpha_x = \frac{\cos\theta}{M} \text{ and } \alpha_r = \frac{\sin\theta}{M}$$

so that

$$\frac{\partial}{\partial x}\left(\frac{\sin\theta}{M}\right) - \frac{\partial}{\partial r}\left(\frac{\cos\theta}{M}\right) = 0 \qquad (1)$$

If A is proportional to the area of a ray tube, then for purely geometrical reasons[†] A must satisfy

$$\frac{\partial}{\partial x}\left(\frac{r\cos\theta}{A}\right) + \frac{\partial}{\partial r}\left(\frac{r\sin\theta}{A}\right) = 0 \qquad (2)$$

Jump conditions across the surface of successive shock-shock positions (hereafter called the shock-shock trajectory) are obtained by considering a narrow ray tube which intersects this surface. The continuity of α and the conservation of $\frac{M\,\nabla\alpha}{A}$ results in the following:

$$\tan(\theta_1-\theta_0) = -\frac{\left((M_1/M_0)^2 - 1\right)^{\frac{1}{2}}\left(1 - (A_1/A_0)^2\right)^{\frac{1}{2}}}{1 + (A_1M_1/A_0M_0)} \qquad (3)$$

$$\tan(\chi-\theta_0) = \left(\frac{(M_1/M_0)^2 - 1}{1 - (A_1/A_0)^2}\right)^{\frac{1}{2}} \qquad (4)$$

where the subscripts "0" and "1" refer to conditions ahead of and behind the shock-shock trajectory, respectively, and $\chi(x, r)$

[†] Detailed derivations of equations 2-5 are given in the cited papers of Whitham.

is the local angle between the trajectory and the axis of symmetry. A final relation between A and M follows from the CCW theory; in the strong shock limit

$$A/A_0 = (M_0/M)^n \; ; \qquad n = \frac{\gamma + 2}{\gamma} + \sqrt{\frac{2\gamma}{\gamma - 1}} \tag{5}$$

where γ is the ratio of specific heats. After using (5) to eliminate A, (1) and (2) form a set of equations for the two dependent variables, M and θ, subject to the boundary condition at the wall $(\theta = \theta_w)$ and the jump conditions given by (3) and (4). To solve this system of equations, numerical techniques employing the method of characteristics are necessary (analogous to the procedures used in axisymmetric, steady, supersonic flow problems).

I. 4. 2 Solution for the Initial Shock-Shock Trajectory

The formidable computational work required to solve the full equations can be avoided by applying the simplified characteristics method used by Whitham (1958) in his formulation of the CCW theory[†]. This application is motivated by the analogy between Whitham's shock-shocks in two-dimensional shock wave propagation. For example, the linear shock-shock trajectory resulting from diffraction by a wedge (as viewed in a Cartesian plane) corresponds to the linear path of a shock wave produced by a piston impulsively started into steady motion (as viewed in a distance-versus-time

---

[†] The author is indebted to Professor Whitham for suggesting this simplification.

plane). When extended to the present axisymmetric case, this analogy calls for the initial shock-shock trajectory to behave like a shock wave produced by a converging cylindrical piston.

The first step in the solution is to write equations (1) and (2) in characteristic form (after eliminating A):

$$d\theta \pm \frac{\sqrt{n}}{M}\, dM + \frac{\tan\theta}{1 \pm \sqrt{n}\,\tan\theta}\,\frac{dr}{r} = 0 \qquad \text{(6a, b)}$$

$$\text{on} \quad \frac{dr}{dx} = \frac{1 \pm \sqrt{n}\,\tan\theta}{\pm\sqrt{n} - \tan\theta}$$

Equation (6b) is a differential relation that holds on characteristics which originate at the cone wall and arrive at the shock-shock trajectory. Following Whitham's method, this equation is applied to local shock wave conditions immediately behind the shock-shock. These conditions are then related to the initial values ahead of the shock-shock by means of the jump relations (3) and (4). After substitution and rewriting, the equation for the trajectory of the first shock-shock reduces to

$$\frac{r}{R} = \exp - \left[\int_{Z_{2-D}}^{Z} g(u)\left(G(u) + \frac{\sqrt{n}}{u}\right) du \right] \qquad (7)$$

$$\text{with} \qquad g(u) = \sqrt{n} + \frac{u\,(u^{n-1} + 1)}{\sqrt{u^2-1}\,\sqrt{u^{2n}-1}} \; ,$$

$$G(u) = \frac{u^{n-1}+1}{(u^{n+1}+1)^2}\,\frac{\sqrt{u^2-1}}{\sqrt{u^{2n}-1}} \left[n + u^2\,\frac{u^{2n}-1}{u^2-1} + (n-1)\,\frac{u^{2n}-1}{u^{n-1}+1} \right] ,$$

$$Z = \frac{M_1(x, r)}{M_0} \quad , \quad \text{and} \quad Z_{2-D} = \frac{\cos\,(\chi_{2-D}-\theta_w)}{\cos\,\chi_{2-D}} \, ,$$

where R is the initial cone radius, u is a dummy variable for Mach number, and χ_{2-D} is given by Whitham's solution for shock diffraction by a wedge with half-angle θ_w. The computational procedure is as follows:

1. A series of values for M_1/M_0 are chosen, and equation (7) is integrated numerically to find the corresponding r/R.
2. For each pair of values for M_1/M_0 and r/R, χ follows from equations (4) and (5).
3. For each set of M_1/M_0, r/R, and χ values, the corresponding x/R is obtained from

$$\frac{x}{R} = \int_{r/R}^{1} \frac{1}{\tan\chi} \, d(r/R)$$

These calculations give the initial shock-shock trajectory and the stemshock Mach number along this curve. The ray inclination along the trajectory (θ_1) is found at each point using equation (3). Information on conditions at other points along the stemshock or in the flow behind the shock is not provided by the solution.

The computed shock-shock trajectory is shown in figure 8, and local shock wave conditions along the trajectory are plotted in figure 9. The curves show that M_1, θ_1, and χ all increase monotonically as the cone axis is approached. In the limit $r/r \rightarrow 0$, $M_1 \rightarrow \infty$ while θ_1 and χ approach $\pi/2$. This singular behavior is evident in the numerical calculations only for extremely small values of r/R[†] .

I. 4. 3 Extension Beyond the Stemshock Intersection on the Cone Axis

An analytical procedure for bridging the singularity on the cone axis has not been obtained. Instead, the solution is extended by assuming a solid boundary exists at some small value of r/R (figure 8) . The minimum r/R chosen for the calculations shown in figure 9 corresponds to the radius of the shock velocity probe used in the experiment. The initial values of M_1 and χ required for computation of the second shock-shock trajectory are specified by assuming local two-dimensional diffraction at the minimum r/R . After the appropriate change in Z_{2-D} , the necessary calculation is again numerical integration of equation (7). For simplicity the origin of the coordinate system is shifted to the start of the second trajectory. A basic difficulty in the procedure now arises from the fact that the solution for the initial shock-shock trajectory does not provide information about local shock wave conditions at other points along the stemshock. Consequently, the initial conditions ahead of the second shock-shock (M_0 , θ_0 , and A_0) are unknown. This difficulty is treated by assuming that the actual variation in the shape and strength of the stemshock can be approximated by taking the rays to be straight and the Mach number between successive

---

[†] For example, when the shock-shock trajectory reaches $r/R = 10^{-4}$ the solution gives $\theta_1 = 63.4°$, $\chi = 64.6°$, and $M_1/M_0 = 2.33$.

rays to be constant[†] in the region between the first and second shock-shock trajectories. With this assumption the computation is similar to that for the first shock-shock trajectory, and results for the 10° half-angle cone are plotted in figure 9. The curves show that near the cone axis the shock-shock conditions change rapidly, with θ_1 and χ increasing while M_1 falls. These trends continue more gradually as the shock-shock approaches the cone wall.

The numerical calculation is discontinued when the second shock-shock reaches the wall, although remaining shock-shock trajectories can be computed in a similar manner. Subsequent cycles of Mach reflection on the cone wall followed by Mach reflection on the axis are approximated by assuming that in each cycle the center shock is initially plane and uniform. The diffraction is then geometrically similar to the first cycle, and the initial calculations are applied after appropriate scale changes. This procedure is made possible by the fact that the solution does not depend on the value of the initial Mach number M_0, provided this value is large enough ($M_0 \gtrsim 3$) for equation (5) to be valid.

An interesting final note on the diffraction solution would

[†] It might appear more consistent to assume the Mach number between successive rays satisfies equation (5). This would result in a gradually increasing Mach number along the rays, since the divergence of the straight rays and their decreasing radial position have the combined effect of slowly reducing A. The actual variation of A due to ray curvature is not known, however, and the approximation as stated gives better agreement with experimental results.

be a comparison between the Mach number averaged over the entire shock front (center shock and stemshock) at each position within the cone, and the Mach number variation predicted by the one-dimensional CCW theory. Such a comparison can be made easily for a wedge-shaped convergence[†], and in that case the averaged diffraction solution reduces identically to the curve predicted by CCW theory. Unfortunately, the simplified characteristics method used in the present axisymmetric case does not provide sufficient information to calculate the average Mach number. Rough estimates of such an average are found to depend on the choice and scaling of the minimum value of r/R. If R' represents the initial cone radius at the start of each diffraction cycle, then setting $(r/R')_{\text{min.}}$ equal to a small, fixed constant results in better agreement with the CCW theory than if $r_{\text{min.}}$ is fixed at some value such as the radius of the velocity probe. This difference is illustrated in figure 10, and will be discussed further in the following section.

I. 4. 4 Comparison Between the Diffraction Solution and the Shock Velocity Measurements

During each Mach reflection process, the variation in Mach number over the stemshock surface should be small compared to

---

[†] The solution for a wedge-shaped convergence follows directly from the solution for diffraction by a wedge (Whitham 1957), since the plane of symmetry acts like a solid boundary. A cyclic pattern of Mach reflections occurs, but in this case all shock-shock trajectories, stemshocks, and center shocks are straight.

the abrupt change at the three-shock intersection[†]. The center shock Mach number along the second shock-shock trajectory is therefore a good approximation to the corresponding Mach number on the cone axis (figure 8), and the diffraction solution can be compared with the velocity probe measurements. As shown in figure 10, the basic characteristics observed in the experiment are predicted by the diffraction solution with $r_{min.}$ set equal to the probe radius. In the first diffraction cycle the stemshock intersection on the cone axis is predicted to occur slightly ahead of the position observed experimentally, and the resulting shock velocity jump is somewhat larger. The solution qualitatively predicts the observed deceleration following the stemshock intersection, but not the gradual acceleration prior to the next intersection. The close comparison in subsequent diffraction cycles supports the assumption of geometrical similarity for the diffraction process after the first cycle. A comparison between the solution and the $M_0 = 10.2$ measurements shows greater disparities (as indicated by the velocity profiles in figure 6), but this is expected since the theoretical model assumes perfect-gas behavior.

The low Mach number measurements show that the velocity increase at the stemshock intersections (the difference between the initial and final values) is nearly constant. This constancy is also predicted by the diffraction solution with $r_{min.}$ set equal to a fixed constant (such as the probe radius). However, the

---

[†] This is evident in the solution for shock diffraction by a solid cone (Whitham 1959).

solution with $(r/R')_{\min.}$ fixed at some small value (curve (iii) in figure 10) predicts that the ratio of final to initial velocities at the intersections is constant, resulting in much higher velocities near the vertex. Since estimates of average Mach number using this method of scaling $r_{\min.}$ compare more favorably with CCW theory, this suggests that greater shock strengthening than indicated by the present measurements might occur in the convergence if the velocity probe were not present†.

---

†Nevertheless, in the experiment the diffraction process was found to be insensitive to the presence of the probe at the first stem-shock intersection. The probe dimensions prevented a similar investigation at later intersections.

I. 5 REFLECTED SHOCK BEHAVIOR

I. 5. 1 Shock Velocity Profiles

The behavior of the reflected shock within the convergence is governed by both the divergent geometry and the complex flow generated by the incident shock. The concluding phase of the present investigation was an examination of this complicated shock motion. The velocity probe was found to respond adequately to the reflected shock, thereby enabling shock velocity measurements to be made in the same manner as for the incident shock. An additional probe with an extended support rod was used to obtain data as far upstream as 13 cm into the constant-area shock tube. Complete velocity profiles for the two cases of Mach six and Mach ten initial shock waves are shown in figure 11. The most outstanding feature of the profiles is the nearly constant velocity observed over most of the convergence length. Small variations in the velocity are apparent near the vertex in both cases, and near the cone entrance in the $M_0 = 6.0$ case. Upon reaching the constant-area channel the shock decelerates towards the velocity corresponding to reflection from a plane end wall[†]. In the $M_0 = 6.0$ case the reflected shock could not be detected for $x/L > 0.84$, but a second reflected shock was observed in the region $0.74 < x/L < 0.92$ propagating with nearly the same velocity as the primary shock. The relative position of this

---

[†] The real-gas calculations of Arave and Huseby (1962) were used to find the velocities for reflection from a plane end wall.

second shock is indicated in figure 12, which shows the distance-versus-time behavior of both the incident and reflected shock waves.

I. 5. 2 Comparison With the Guderley Similarity Solution

The Guderley similarity solution for an imploding spherical shock wave (Guderley 1942, Butler 1954) predicts that the velocity of the subsequent reflected shock will vary with radial distance according to a simple power law. As indicated in figure 11, this power law obviously does not compare with the nearly constant shock velocity found in the experiment. The dissimilarity between the measurements and the similarity solution is primarily a consequence of the finite length of the cone, which results in fundamental differences between the experimental flow conditions and the conditions assumed in the similarity analysis. This can be shown by using the similarity solution for the flow behind the incident shock to calculate approximate particle paths for fluid initially within the convergence. Particle paths originating at the cone entrance are drawn in figure 12, and indicate that for $x/L \lesssim 0.66$ in the $M_0 = 6.0$ case, and for $x/L \lesssim 0.75$ in the $M_0 = 10.2$ case, the reflected shock propagates into fluid originally set into uniform motion by the incident shock wave in the constant-area channel upstream of the cone. In the similarity analysis the fluid in these regions has supposedly undergone a gradual, continuous compression after initially experiencing a much weaker shock, resulting in conditions ahead of the reflected shock that progressively deviate from the experimental flow conditions. A simplified model for the actual flow ahead of the reflected shock, together with an approximate solution for the corresponding shock motion in the $M_0 = 6.0$ case, can be found in the appendix.

I. 6 CONCLUSIONS

A comprehensive investigation has been made of the shock dynamics within a 10° half-angle conical convergence mounted on a conventional shock tube. Measured shock velocity profiles show that the incident shock behavior is dominated by cyclic diffraction processes which originate at the entrance of the cone. During each diffraction cycle the shock first undergoes Mach reflection on the cone wall, then Mach reflection on the axis. These cycles evidently persist until the shock reaches the vertex, where the measured velocity has increased by as much as a factor of three. Real gas effects, enhanced by increasing the initial Mach number and decreasing the pressure, apparently alter the shock wave behavior only in the region near the vertex.

The basic features of the incident shock behavior are described analytically by applying Whitham's axisymmetric shock diffraction equations (Whitham 1959) to the converging conical geometry. An approximate solution is obtained by using the simplified characteristics method applied by Whitham in his formulation of the CCW theory (Whitham 1958). The first two shock-shock trajectories are computed numerically, and subsequent diffraction cycles are assumed to be geometrically similar to the initial cycle.

Measured velocity profiles for the reflected shock within the cone show that the shock velocity is nearly constant throughout most of the convergence length. This behavior obviously contrasts with the power-law decline in velocity predicted by the

Guderley similarity solution (Guderley 1942, Butler 1954). Simple arguments show that this disparity is primarily a consequence of the finite length of the cone, which results in fundamentally different experimental flow conditions ahead of the reflected shock.

APPENDIX. Reflected Shock Propagating into Steady Subsonic Flow

An approximate analytical description of the reflected shock motion can be obtained by assuming a simplified model for the flow of fluid initially outside the cone entrance. The Mach number of the flow behind the Mach six and Mach ten initial shock waves is 1.26 and 1.31, respectively. At these Mach numbers the supersonic flow near the shock tube wall cannot be turned through the 10° angle at the cone entrance by means of a stationary, oblique shock. Consequently, as the initial shock enters the cone an upstream-facing shock locally normal to the wall must form outside the entrance[†]. An unsteady sonic surface behind this shock separates subsonic flow adjacent to the wall from the central supersonic stream. The subsonic region grows as the upstream-facing shock propagates outward from the cone entrance; eventually this region fills the channel cross-sectional area if the sonic surface reaches the axis. A simple, one-dimensional flow model which assumes that a uniform subsonic region is created by a plane upstream-facing shock is pictured in figure 13. The upstream shock is assumed to propagate at constant velocity, resulting in a subsonic flow which subsequently undergoes a steady, isentropic compression in the convergence. The reflected shock is assumed to start at some position upstream of the sonic point for this flow with an initial velocity given by the velocity probe measurements.

[†] This shock is an extension of the third (reflected) shock formed in the initial Mach reflection on the cone wall.

The reflected shock motion is found using Whitham's simplified characteristics method for one-dimensional shock propagation into non-uniform media (Whitham 1958) in a manner suggested by Chester (1960). The differential relation which holds along characteristics overtaking the reflected shock trajectory is applied to flow conditions immediately behind the shock. The Rankine-Hugoniot relations are then used to couple these conditions to the known distribution of flow variables in the steady compression ahead of the shock. The result is a first-order, ordinary, nonlinear differential equation for shock Mach number (or velocity) as a function of position that can be numerically integrated. The curves shown in figure 13 were obtained by performing the integration for several possible steady flow situations ahead of the $M_0 = 6.0$ reflected shock. The upstream-facing shock was required to be fairly strong (Mach number ~2) in order for the predicted sonic point of the subsonic compression to be sufficiently near the cone vertex. Although the theoretical curves show a gradual deceleration of the reflected shock within the convergence, the comparison with experimental results is still far better than can be made with the similarity solution[†]. It should be noted that Whitham's method neglects modification of the shock motion by re-reflected disturbances, and in the assumed flow model such disturbances could be important.

[†] The initial rise displayed by two of the curves results from starting the reflected shock close to the sonic point.

REFERENCES FOR PART I

ARAVE, R. & HUSEBY, O. 1962. Boeing Report No. D2-11238.

BELOKIN', V. A., PETRUKHIN, A. I. & PROSKURYAKOV, V. A. 1965. Soviet Physics JETP (Eng. Transl.) 21, 33.

BIRD, G. A. 1959. J. Fluid Mech. 5, 60.

BUTLER, D. S. 1954. Armament Research Establishment Report 54/54.

CHESTER, W. 1954. Phil. Mag. (7) 45, 1293.

CHESTER, W. 1960. Adv. Appl. Mech. VI, 120.

CHISNELL, R. F. 1957. J. Fluid Mech. 2, 286.

GUDERLEY, G. 1942. Luftfahrtforschung, 19, 302.

LAU, J. 1971. C.A.S.I. Trans. 4, 13.

McEWAN, A. D. 1968. Australian Defense Scientific Service Aerodynamics Note 298.

MILTON, B. E. & ARCHER, R. D. 1969. A.I.A.A. J. 7, 779.

RUSSELL, D. A. 1967. J. Fluid Mech. 27, 305.

SETCHELL, R. E. 1971. Ph.D. Thesis, California Institute of Technology.

SKEWS, B. W. 1972. A.I.A.A. J. 10, 839.

SMITH, J. A. 1967. Ph.D. Thesis, California Institute of Technology.

WHITHAM, G. B. 1957. J. Fluid Mech. 2, 145.

WHITHAM, G. B. 1958. J. Fluid Mech. 4, 337.

WHITHAM, G. B. 1959. J. Fluid Mech. 5, 369.

PART II

SPECTROSCOPIC INVESTIGATION OF STRONG SHOCKWAVES IN A CONICAL CONVERGENT CHANNEL

By

Erik Storm

II.1 INTRODUCTION

The behavior of a shock wave propagating into a conical convergence has been studied extensively at the GALCIT† facilities over the past few years (part I and Ref. 1-2). Both the theoretical investigation by the author, and the comprehensive experimental work by Setchell discussed in part I, indicate that a conical convergence can produce a small region of very hot, highly compressed fluid near the vertex. Setchell[2] limited his investigation to the measurement of centerline velocities in the 10° half-angle cone, but estimates show that temperatures can be achieved that are well above the typical range of pressure-driven shock tubes.

The shock behavior throughout the cone is dominated by multiple shock diffraction processes initiated by the geometry change at the cone entrance. Rapid increases in shock velocity occur along the cone axis, corresponding to the intersection of stemshocks formed by Mach reflection on the cone walls. The use of a conical convergence as a tool in conventional high temperature plasma research is therefore somewhat restricted, since the thermodynamic conditions produced behind the incident shock wave are nonuniform both as a function of time and position. Near the vertex, the reflected shock wave will leave the test gas in a high degree of excitation. The subsequent rapid expansion is likely to produce a nonequilibrium state with a possible

---

† Graduate Aeronautical Laboratories California Institute of Technology.

population inversion in the higher atomic energy levels. Due to the short optical path length available, it is unlikely that this inversion could be used to produce a useful gas dynamic laser. It does offer, however, an opportunity to study nonequilibrium gas dynamics and nonequilibrium radiation phenomena.

II. 1. 1 The Strengthening of a Shock Wave in a 10° Half-Angle Cone

Since a complete account of the shock dynamics in a 10° half-angle cone terminating a conventional pressure-driven shock tube can be found in part I and reference 2, only a summary of the aspects relevant to the present investigation will be given here.

Both the theoretical investigation and the shock velocity measurements show that for initial Mach numbers > 3, the incident shock behavior is dominated by the diffraction processes originating at the cone entrance. The main features of the shock wave pattern as it would appear at various times is indicated in figure 5, and the resulting centerline shock velocity as a function of distance into the cone is shown in figure 10. The constant centerline velocity for $x/L < 0.3$, and the corresponding diffraction pattern is a result of Mach reflection of the initially plane shock wave on the cone wall. The first velocity jump shown in figure 10, indicates the arrival of the three-shock intersection point on the cone axis. Mach reflection of the stemshock on the cone axis then occurs and a center shock progressively grows until at $x/L = 0.48$ it fills the cone. With the exception of the slight curvature of the center shock, the shock structure at this point is similar to the initial one, the only difference being a scale change. In the theoretical model this approximation is made, and the center shock is assumed plane and uniform. Subsequent diffraction cycles are then geometrically similar, and continue until the shock wave reaches the cone vertex. The fairly close agreement between theory and experiment seems to indicate that this simplified geometrical model is a reasonable one.

As long as real gas effects can be neglected, the entire process should scale with the initial Mach number. Figure 3 shows a comparison of shock velocity profiles for initial Mach numbers of 6.0 and 10.2. The diffraction pattern is essentially unchanged except for x/L past the 3rd stemshock intersection point, even though significant real gas effects (e.g., ionization in the case of argon) would be expected beyond the first stemshock intersection point in the $M_o = 10.2$ case. An examination of the local relaxation times, indicates that the scaling begins to break down when relaxation times become less than a characteristic time given by M/(dM/dt).

Reflected shock velocities were found to be nearly constant[2], indicating that the deceleration expected due to the divergent geometry is balanced by the effects of the nonuniform, unsteady flow generated by the incident shock.

II.1.2 Thermodynamic Conditions Expected Near the Cone Vertex

The approach to equilibrium following the viscous shock front, and the associated relaxation times in monatomic gases has been studied extensively (Refs. 3-6). Although there is still controversy concerning the theoretical treatment of the initial phase of the relaxation process, there exists an abundance of experimental data on relaxation times. Treating the shock wave as separating two regions of thermodynamic equilibrium, the problem of determining the state of the shock-heated plasma reduces simply to solving the Rankine-Hugoniot relations allowing for the effects of ionization and electronic excitation in the expression for the thermodynamic quantities.

With the exception of boundary layer effects, the near homogeneity of shock-heated plasmas in a direction perpendicular to the tube axis, is well known. In the case of the cone, where the shock dynamics are dominated by the diffraction processes, the situation is more complicated. In addition to variation of Mach number as a function of distance into the cone, conditions vary along the shock front itself. Excluding the immediate neighborhood of a stemshock intersection point, the value of the Mach number on the centerline may be taken as a first approximation to the Mach number averaged across the shock surface. If in addition, the local relaxation times are less than the cone radius (or some other measure of a typical diffraction length) divided by the shock velocity, then equilibrium calculations based on the local centerline Mach number should give a first estimate of thermodynamic conditions immediately following the shock wave. Taking an initial Mach number of 10.2 and a test gas of argon at 1.5 torr, and using relaxation times from reference 3, we find from figure 3 that the above criterion is satisfied beyond the third stemshock intersection point. Choosing x/L = 0.9 as an example, then immediately following the incident shock wave we would expect an equilibrium temperature of 14400°K, a degree of ionization of 0.47, an electron number density of 2.92×10^{17} cm^{-3} and a pressure of 1335 torr, corresponding to equilibrium conditions behind a Mach 23.7 shock wave.†

Unlike in a conventional shock tube where at any time the fluid passing an observation point has been heated by a constant Mach number shock wave, the thermodynamic conditions in the cone will again be dominated by the diffraction processes. From figure 3 we see that the fluid passing x/L = 0.9 shortly after the arrival of the incident shock, will have been processed by a shock wave of Mach number less than 23.7, whereas the fluid originally at x/L = 0.84 (i.e., the location of the 3rd stemshock intersection point) would have been heated by a shock wave of greater Mach number. Allowing for compression resulting from the convergent geometry, we would expect that at a given position near the vertex the thermodynamic conditions as a function of time will experience

---

†As part of the present investigation, a program was carried out to compute the thermodynamic state of a shock-heated multiply-ionized argon plasma. The details of the computational procedure are found in Appendix A.

a gradual increase in temperature, density, and pressure, upon which will be superimposed the effects of nonuniformities due to shock diffraction.

The arrival of the reflected shock wave increases the temperature, density and pressure even more and raises the fluid to a highly excited state. Since the fluid velocity ahead of the reflected shock is not known, only rough estimates of expected equilibrium conditions behind the reflected shock can be made, but temperatures in excess of $50,000^{\circ}K$ should be obtainable. The relevant relaxation time is now governed by the time needed to establish equilibrium in doubly ionized argon, and is less than the relaxation time associated with single ionization behind the incident shock wave. It is therefore quite plausible that the subsequent expansion (due to the divergent geometry) following the reflected shock will cause a rapid cooling of the plasma starting from complete second ionization equilibrium.

II. 1. 3 Measurement of Thermodynamic Properties in a High Temperature Shock-Heated Plasma

The composition of a plasma in thermodynamic equilibrium is uniquely determined once the temperature and electron number density are known. Experimental and theoretical techniques in plasma diagonostics have been discussed extensively in the literature (see for example references 7 - 11); the monograph by Griem[7] can perhaps be regarded as the standard textbook on plasma spectroscopy for laboratory work.

For a shock-heated plasma, the desirability of non-interference with the moving fluid gives preference to spectroscopic techniques. This is especially true near the vertex of a conical, convergent channel, where the physical dimensions become quite small. In the present investigation the choice was narrowed down even further, to emission spectroscopy. Emission spectroscopy deals only with the actual emission of the plasma itself, and the amount of information that can be deduced from a calibrated spectrum is very large. The distribution of spectral intensity in a line (bound-bound transitons) and its vicinity in theory supplies the following information about a plasma in a state of local thermodynamic equilibrium (the distinction between full and local thermodynamic equilibrium will be dealt with in Section II. 2. 1):

1. The wave length gives information that a certain element is present in a given stage of ionization.
2. The line profile can be used to determine the density of perturbing particles (pressure broadening

or the kinetic temperature of the emitting atom (Doppler broadening). See sketch below.

3. The excitation temperature and particle density can be deduced from the total energy emitted in the line.
4. Continuum intensity (free-bound and free-free transitions) may be used to find the electron number density and electron temperature.

Adding to this the fact that the emitted spectrum usually has several lines over a large range of wave lengths, one can easily understand the importance of emission spectroscopy as a tool in high temperature plasma diagnostics.

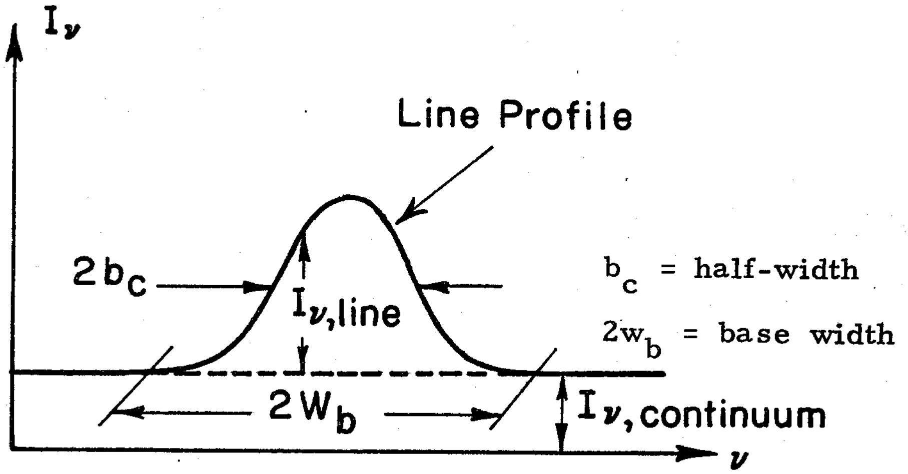

b_c = half-width

$2w_b$ = base width

II. 1. 4 Goals of the Present Investigation

The present investigation is a logical extension of the previous work on shock dynamics in convergent channels (Ref. 1, 2). The existence of high Mach numbers near the cone vertex had been established, but measurements of thermodynamic properties were needed in order to determine the possible uses of such a geometry in high temperature plasma research. The choice of emission spectroscopy as the experimental technique was discussed in the previous section. This method has been used successfully in connection with conventional shock tubes. In the present situation, however, large nonuniformities are present due to the method of shock intensification, so care must be taken in interpreting the experimental data.

The main objective of this report is an investigation into the possibility of using well-known spectroscopic techniques to determine the state of a shock-heated fluid near the vertex of a 10^o half-angle cone. Emphasis is placed on establishing the effect of shock diffraction on the thermodynamic properties behind the incident shock wave. The possible existence of sustained nonequilibrium conditions behind the reflected shock wave is also investigated. Finally, it is hoped that the present report is a step towards a better understanding of the effectiveness and accuracy of emission spectroscopy as a diagnostic tool in shock tube work.

II. 2 EMISSION SPECTROSCOPY

II. 2. 1 Local Thermodynamic Equilibrium

A very powerful concept used in plasma spectroscopy is that of local thermodynamic equilibrium (LTE). Whenever LTE prevails, the resulting stationary state can be described by the same laws which govern true thermodynamic equilibrium, with the exception of the emitted radiation. As long as collisions are dominant, LTE may even be reached in a plasma where self-absorption effects are negligible, i.e., an optically thin plasma. The relevant temperature is that which describes the distribution function of the species dominating the reaction rates. In dense laboratory plasmas, electrons play a dominant role, and the distribution of particles among excited energy levels is given by Boltzmann statistics, with the electron temperature as the appropriate parameter. Such a plasma is often referred to as a collision-dominated plasma.

The importance of LTE enters critically into the equations relating plasma parameters with observed spectral intensities. For an optically thin plasma, the observed intensities are directly related to the number of particles in a given excited state. Reducing this to knowledge of total number densities and electron temperature is only meaningful if LTE exists. When self-absorption is important the presence of LTE is essential. The ratio of emission and absorption coefficients, which must be known if corrections of the observed intensities are to be made, is equal to the Planck function only if LTE prevails.

For an optically thin plasma, LTE can be expected only if the electron collision rates greatly exceed the radiative decay rates. Following McWhirter[10] and Griem[7], and demanding that the collisional de-excitation rate (which, in equilibrium, is equal to the excitation rate) between quantum levels n and m $(n > m)$ exceed the spontaneous emission rate by a factor of 10 we find that, for hydrogen-like atoms, LTE is achieved, if for all levels n and m

$$N_e \geq 9.2 \times 10^{17} z^7 \sqrt{\frac{kT_e}{E_I}} \left(\frac{E_n - E_m}{E_I} \right)^3 . \qquad (1)$$

Here T_e is the electron temperature, E_n, E_m are the excitation energies of level n and m respectively, E_I is the ionization energy of the atom (ion) and z is the charge "seen" by the optical electron (i.e., $z = 1$ for neutral atoms, $z = 2$ for singly ionized atoms, etc.). Assuming the collisional excitation from the ground state to be the rate determining step in the chain of excitation processes leading to LTE, we find the condition for complete LTE by setting $(E_n - E_m)$ in equation (1) equal to the excitation energy of the first excited level (the resonance level). For neutral argon an electron density of

$$N_e \geq 1.42 \times 10^{17} \sqrt{T_e \times 10^{-4}} , \qquad (2)$$

with T_e in °K, would thus be sufficient to obtain complete LTE[†].

[†] Although Kolesnikov[12] has reported LTE in a free burning argon arc at atmospheric pressure and 10,000°K for $N_e > 10^{16}$ cm^{-3}.

If the plasma is optically thick with respect to the resonance line radiation, the criterion of equation (2) may be relaxed by an order of magnitude (Griem[7]).

It is also useful to consider partial LTE. This is defined by the condition that Boltzmann statistics gives the correct population densities for all energy levels above a certain value. Since $(E_n - E_m)$ decreases rapidly with increasing quantum number (for highly excited levels $(E_n - E_m) \propto 2/n^3$) partial LTE would be expected to exist for any $n > m$ if equation (1) is satisfied with $(E_n - E_m)$ equal to $(E_{m+1} - E_m)$. For neutral argon this implies that Boltzmann statistics with T_e as the relevant temperature would be valid down to, and including the first excited level if

$$N_e \geq 4.82 \times 10^{14} \sqrt{T_e \times 10^{-4}} \qquad (3)$$

with T_e in ^oK.

When the condition given by equation (2) is satisfied, the distribution of population number densities are given by the Boltzmann and Saha equations in the following form

$$\frac{N_n}{N_m} = \frac{g_n \exp(-E_n/kT)}{g_m \exp(-E_m/kT)} \qquad (4)$$

and

$$\frac{N_e N_z}{N_{z-1}} = 2 \frac{Z_z}{Z_{z-1}} \left(\frac{2\pi m_e kT}{h^2} \right)^{3/2} \exp\left(- \frac{E_I^{z-1} - \Delta E_I^{z-1}}{kT} \right) . \qquad (5)$$

Here N_n, N_m and g_n, g_m are number densities and statistical weights of state n and m , N_{z-1}, N_z are the total number densities of atoms or ions in two subsequent ionization stages (N_o signifying neutral atoms, N_1 singly ionized atoms etc.) and E_I^{z-1} is the ionization energy of state z -1 . Z and ΔE_I are the partition function and the reduction of ionization energy respectively and are discussed in appendix A. For complete LTE we also have $T = T_e = T_{ion} = T_{atom}$.

In the absence of complete LTE equation (4) is only valid for n, m > n* , where n* is lowest energy level that satisfies the criterion (1), and T_e must be substituted for T . The Saha equation in the form given by Eq. (5) is also no longer applicable. Instead, the following modified version (valid for n > n*) must be used.

$$\frac{N_e\, N_z}{N_n^{z-1}} = 2\,\frac{Z_z}{g_n^{z-1}}\left(\frac{2\pi\, m_e\, k\, T_e}{h^2}\right)^{3/2} \exp\left(-E_{nI}^{z-1}/k\, T_e\right). \qquad (6)$$

Here E_{nI}^{z-1} is the binding energy of the electron in state n . $\left(E_{nI}^{z-1} = E_I^{z-1} - \Delta E_I^{z-1} - E_n^{z-1}\right)$.

II. 2. 2 Line Broadening and Line Shift

Broadening and shift of spectral lines in a plasma is a complicated function of the plasma composition. The two major causes for line broadening are the Doppler and Stark effects. Doppler broadening is primarily a temperature effect, while Stark broadening is a special case of pressure broadening. Pressure broadening, as the name suggests, is caused by interactions of the emitting atom (ion) with surrounding particles. It is generally divided into 3 subclasses, resonance, Van der Waals and Stark broadening, depending upon whether the broadening is caused by particles of the same kind, particles of a different specie, or charged particles, respectively.

As long as the electron concentration comprises at least 1% of the total number density, Stark broadening is by far the dominant type of pressure broadening. In plasmas with electron number densities of about 10^{17} cm^{-3} and electron temperatures less than $40000^{o}K$, line broadening by the Stark effect is also greater than that due to Doppler broadening. Since the conditions cited above are precisely those encountered in the present investigation, the remainder of this section deals with the Stark effect and its influence on measured quantities in emission spectroscopy. For cases in which Doppler broadening is the most important, or when the two are of equal magnitude, the reader is referred to Unsöld[8].

As long as only natural line broadening (the effect of the Heisenberg uncertainty principle) is present, the distribution of energy in a spectral line is closely approximated by a delta function. All the energy can be said to be emitted at the line frequency ν_o . When other broadening mechanisms can no longer be neglected, the distribution of energy over frequency, or the line shape, must be taken into account. In the case of Stark broadening, the line shape is closely approximated by the Lorentzian or dispersion type profile[7-10]

$$I_\nu = I_\ell \frac{b_c/\pi}{(\nu-\nu_o)^2 + b_c^2} \equiv I_\ell \varphi(\nu) \tag{7}$$

where I_ℓ is the total integrated line intensity (i. e., $I_\ell = \int_{-\infty}^{\infty} I_\nu \, d(\nu-\nu_o)$) and b_c is the Stark half-width defined as one half of the frequency interval over which the intensity has decreased to one half of its maximum value. Measurements of total line intensities I_ℓ , comprise an important part of emission spectroscopy. If the intensity is determined from photo-multiplier measurements, inspection of (7) implies that even when the continuum intensity is properly accounted for, and the equivalent exit slit width is many times b_c , the measured intensity is still considerably less than the total intensity. Assuming the frequency range covered by the optical system to be $\nu_o \pm w$, a simple integration of (7) shows that

$$\frac{(I_\ell)\text{ measured}}{I_\ell} \equiv \frac{I_{\ell m}}{I_\ell} = \frac{\tan^{-1}(w/b_c)}{\pi/2} \quad . \tag{8}$$

For simple geometrical considerations, the following relationships can also be dervied,

$$\frac{I_{\ell m}}{I_{\ell}} = \frac{2}{\pi} \tan^{-1} \sqrt{\left(\frac{w}{b_c^m}\right)^2 - 2} \tag{9}$$

and

$$\frac{b_c^m}{b_c} = \sqrt{1-2\,\frac{b_c^m}{w_b}} \tag{10}$$

where b_c^m is measured half-width, and w_b is the base-width. The base-width is the wave length (or frequency) interval between two points on the experimentally determined profile where the background intensity is assumed, as indicated in the sketch on page 36. Equations (9) and (10) are plotted in figure 14. Note that even for $w/b_c^m = 10$, about 6% of the total line intensity is not included in the measured value. The correction to the measured half-width is less than the total line intensity correction, but it must still be taken into account.

In addition to broadening of the profile (the linear Stark effect), the interactions of the charged particles with the emitting atom (ion) may also result in an asymmetric effect (the quadratic Stark effect). This causes a net frequency shift of the emitted line radiation. For argon this effect is present, and the Stark shift must in general be included in the function $\varphi(\nu)$.

$$\varphi(\nu) = \frac{1}{\pi}\,\frac{b_c}{\left(b_s + (\nu-\nu_o)\right)^2 + b_c^2} \tag{11}$$

This represents a dispersion profile with the center of the line (Stark) shifted to $\nu_o - b_s$. When using the line shape function $\varphi(\nu)$ in the following sections, it will always be assumed that we have made a frequency transformation of the form $\nu_o - b_s \rightarrow \nu'_o$, and hence we will use $\varphi(\nu)$ as defined by equation (7).

The most important application of Stark broadening and Stark shifts is in the determination of electron number densities. A complete theoretical treatment can be found in Griem[7]. In this brief discussion it is sufficient to note that both the half-width and line shift are almost directly proportional to the electron number density, and only weakly dependent upon temperature. Complete line profiles have been calculated by Griem[7] for the most common hydrogen lines, ionized helium, and many isolated lines of heavier elements. In most cases, however, the electron number density can be determined accurately by measuring only the half-width or the line shift. The appropriate equations and formulas are found in reference 7.

II. 2. 3 Radiative Transfer in Collision-Dominated Plasmas

Under the assumption that the radiation field in a plasma can be treated as quasi-steady at any instant of time[†], following reference 11, the radiative transfer equation can be written as

$$\frac{dI_\nu}{ds} = \epsilon_\nu - \kappa'_\nu I_\nu \tag{12}$$

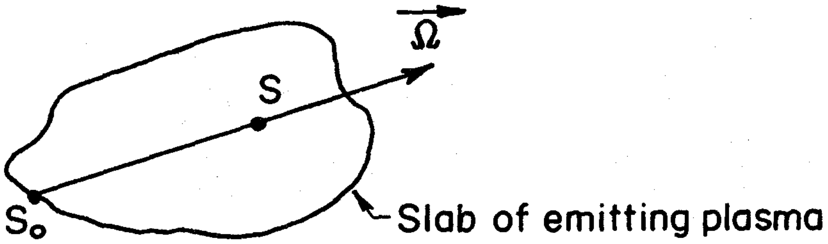

where, referring to the figure above, I_ν is the intensity of electromagnetic radiation (erg/sec/ster-cm^3-sec^{-1}) as a function of the coordinate s along a ray in the direction $\vec{\Omega}$, ϵ_ν is the emission coefficient and κ'_ν is the effective absorption coefficient[††]. The general solution to equation (12) is given by

$$I_\nu(s) = \int_{s_o}^{s} \epsilon_\nu \exp\left(-\int_{s'}^{s} \kappa'_\nu \, ds''\right) ds' + I_\nu^o \exp\left(-\int_{s_o}^{s} \kappa'_\nu \, ds''\right), \tag{13}$$

where I_ν^o is the intensity of external radiation incident upon the plasma. In the special case of a homogeneous plasma and $I_\nu^o = 0$, the solution of (13) is greatly simplified. Neglecting boundary

---

[†] True in general as long as the relevant fluid velocities are much less than the speed of light.

[††] Following the standard method of treating induced emission as negative absorption.

layer effects, this situation is very closely approximated by the emission from a shock-heated plasma, when viewed at right angles to the flow direction. Setting $s_o = 0$, $s = L$, where L is the dimension of the plasma in the direction along the ray, and carrying out the integration we find that the radiation intensity leaving the plasma is equal to

$$I_\nu = \frac{\epsilon_\nu}{\kappa'_\nu} \left(1 - \exp(-\kappa'_\nu L)\right) . \tag{14}$$

$\kappa'_\nu L$ is often referred to as the optical thickness. For the two limiting cases $\kappa'_\nu L \ll 1$ (optically thin) and $\kappa'_\nu L \gg 1$ (optically thick), equation (14) reduces to the well known

$$I_\nu = \epsilon_\nu L \qquad \text{for} \quad \kappa'_\nu L \ll 1 , \tag{15a}$$

$$I_\nu = \frac{\epsilon_\nu}{\kappa'_\nu} \qquad \text{for} \quad \kappa'_\nu L \gg 1 . \tag{16a}$$

If the plasma is in LTE, Kirchhoff's law relating the emission coefficient to the effective absorption coefficient in the form

$$\epsilon_\nu = I_{p\nu} \kappa'_\nu \tag{17}$$

may be used to obtain

$$I_\nu = I_{p\nu} \kappa'_\nu L \qquad \text{for} \quad \kappa'_\nu L \ll 1 \tag{15b}$$

and

$$I_\nu = I_{p\nu} \qquad \text{for} \quad \kappa'_\nu L \gg 1 \tag{16b}$$

where $I_{p\nu} = 2h\nu^3 (\exp(h\nu/kT) - 1)^{-1}/c^2$ is the Planck function.

In general a plasma will emit a line spectrum (bound-bound transitions) superimposed upon a continuous spectrum (free-free and free-bound transitions), refer to the figure on page 36. ϵ_ν and κ'_ν must then be written as a sum of two contributions

$$\epsilon_\nu = \epsilon_{\ell\nu} + \epsilon_{c\nu} \quad \text{and} \quad \kappa'_\nu = \kappa'_{\ell\nu} + \kappa'_{c\nu} ,$$

where the subscripts ℓ and c refer to line and continuum respectively. In an experimental situation the emitted radiation is often recorded over a frequency interval $\nu_o \pm \Delta\nu$, ν_o being the central frequency of a spectral line. This measured intensity is given by integration of (14) over said frequency interval,

$$I_{\text{measured}} \equiv I_m = \int_{-\Delta\nu}^{\Delta\nu} \frac{\epsilon_\nu}{\kappa'_\nu} [1 - \exp(-\kappa'_\nu L)]\, d(\nu-\nu_o) . \qquad (17)$$

The process of interpreting this measured quantity in terms of the local thermodynamic properties of the plasma is one of the fundamental functions of emission spectroscopy, and will be dealt with in the following sections.

II. 2. 3a Emission and Absorption in Spectral Lines

Let A_{nm}, $B_{nm}I_{\nu}$ and $B_{mn}I_{\nu}$ represent the transition probabilities per unit time for spontaneous emission, induced emission and absorption, respectively, of photons in the range ν to $\nu + d\nu$ for transitions between quantum levels n and m $(n > m)$, where A_{nm}, B_{nm} and B_{mn} are the familiar Einstein coefficients. Similarly, let $\varphi_{nm}(\nu)$, $\eta_{nm}(\nu)$ and $\eta_{mn}(\nu)$ be the line shape functions, or energy distribution functions† for spontaneous emission induced emission and absorption, respectively. If N_n and N_m denote the population number densities of states n and m , then for bound-bound transitions the right hand side of equation (12) will take on the form

$$\frac{1}{4\pi} h\nu\ N_n\ \varphi_{nm}(\nu)\ A_{nm} - \frac{1}{4\pi} h\nu \left(N_m \eta_{mn}(\nu)\ B_{mn} - N_n\ \eta_{nm}(\nu)\ B_{nm}\right) I_{\nu}.$$

The emission coefficient and effective absorption coefficient for bound-bound transitions are thus given by

$$\varepsilon_{\ell\nu} = \frac{1}{4\pi} h\nu\ N_n\ \varphi_{nm}\ (\nu)\ A_{nm} \tag{18}$$

and

$$\kappa'_{\ell\nu} = \frac{1}{4\pi} h\nu\ N_n\ \eta_{nm}(\nu)\ B_{nm} \left(\frac{N_m\ \eta_{mn}(\nu)\ B_{mn}}{N_n\ \eta_{nm}(\nu)\ B_{nm}} - 1 \right) . \tag{19}$$

Calculations of the transition probabilities using first-order perturbation theory by Griem[7], lead to the relationships

---

† Properly normalized such that $\int \varphi_{nm}\, d\nu = \int \varphi_{nm}\, d\nu = \int \eta_{mn} d\nu = 1$

$$\frac{A_{nm}}{B_{nm}} = \frac{2h\nu^3}{c^2} \tag{20}$$

and

$$\frac{B_{nm}}{B_{mn}} = \frac{g_m}{g_n} \quad . \tag{21}$$

For collision-dominated plasmas, the line shape functions $\eta_{nm}(\nu)$ and $\eta_{mn}(\nu)$ are equal[9], and from reference 11 we have the general result that the ratio of spontaneous to induced emission must be equal to $2h\nu^3/I_\nu c^2$. Combining this with equations (18) - (21) results in the following equations

$$\varphi_{nm}(\nu) = \eta_{nm}(\nu) \tag{22}$$

$$\epsilon_\nu / \kappa'_\nu = \frac{2h\nu^3/c^2}{(N_m \; g_n/N_n \; g_m \; - \; 1)} \quad . \tag{23}$$

Note that there have been no assumptions made concerning the existence of equilibrium in the derivation of equation (23). We see now that as long as partial LTE exists above the lower level m, equation (23) is identical to equation (17) with the temperature in the expression for the Planck function $I_{p\nu}$ equal to T_e. For partial LTE above the lower level m, the effective absorption coefficient is then

$$\kappa'_{\ell\nu} = \frac{A_{nm}}{8\pi} \frac{c^2}{\nu^2} N_n \left(\exp\,(h\nu/k\,T_e) - 1\right) \varphi_{nm}(\nu) \quad . \tag{24}$$

If complete LTE prevails, Boltzmann statistics are usually employed to replace N_n by $N_z \, g_n^z \exp\left(-E_n^z/kT_e\right)/Z_z(T_e)$.

Although in complete LTE $T = T_e = T_{ion} = T_{atom}$, the choice of T_e as the relevant temperature in collision-dominated plasmas is customary[†]. $Z_z(T_e)$, the electronic partition of the atom (ion) is given by

$$Z_z(T_e) = \sum_i g_i^z \exp(-E_i^z/kT_e) ,$$

where the usual care must be taken to truncate the sum at some appropriate level to avoid the otherwise purely mathematical singularity.

From equations (7), (15a) and (18) we find that, for an atom, the total energy emitted in a spectral line from an optically thin LTE plasma is given by

$$I_\ell = \frac{L}{4\pi} A_{nm} h\nu_{nm} g_n \frac{N_o}{Z_o(T_e)} \exp(-E_n/kT_e) . \qquad (25)$$

It is therefore in principle possible to determine the electron temperature from the absolute measurement of total emitted intensity in a single line, provided N_o is known. Measuring the relative intensities of several lines of a single emitting species, however, eliminates the need to know the number density and the partition function. From (25) we find that for each line

$$\ln(I_\ell/A_{nm} g_n \nu_{nm}) = -(E_n/kT_e) + \text{constant}. \qquad (26)$$

Plotting $\ln(I_\ell/A_{nm} g_n \nu_{nm})$ vs. E_n/k therefore gives a straight line of slope $-1/T_e$. When self-absorption effects become

---

[†] See discussion in section II. 2. 1.

important, the measured intensities can in principle be "corrected" to what they would have been if the plasma were optically thin. Note that this method is also valid for a plasma in partial LTE, as long as the partial LTE extends down to the lowest energy level of interest.

The electron temperature as determined by relative line intensities from the same stage of ionization, is in general not very accurate. The principal reason for this is the relatively small separation between the upper energy levels of the two lines, accentuating any uncertainty in either the transition probabilities or the experimental measurements. Using lines from successive stages of ionization results in principle in considerable improvement of the accuracy. From (25) and the Saha equation (5), the ratio of total line intensities from subsequent ionization stages (e. g., ion and atom), is given by

$$\frac{I_\ell^1}{I_\ell^o} = 2\,\frac{\left(A_{nm}\, g_n\, h\nu_{nm}\right)^1}{\left(A_{nm}\, g_n\, h\nu_{nm}\right)^o}\left(\frac{2\pi m_e k}{h^2}\right)^{\frac{3}{2}} \frac{T_e^{\frac{3}{2}}}{N_e}\,\exp\left(-\,\frac{E_I^o - \Delta E_I^o + E_n^1 - E_n^o}{kT_e}\right). \tag{27}$$

It is seen that E_I is added to the difference in excitation energies. This advantage is counterbalanced, however, by the appearance of N_e and ΔE_I in (27). N_e is a function of T_e and ΔE_I is a function of both T_e and N_e. The existance of full Saha equilibrium, i. e., complete LTE, is also necessary to obtain (27).

II. 2. 3b Continuum Emission and Absorption

A continuous emission or absorption spectrum is always formed when at least one of the respective quantum states is a free state, with a continuum of permitted energy levels. The most important continua for plasma spectroscopy are those caused by recombination (free-bound transition) and bremsstrahlung (free-free transitions). Following Zel'dovich and Raizer[11] the continuum emission coefficient for hydrogen-like ions can be formulated by deriving transition probabilities for free-bound and free-free transitions with only one equilibrium assumption, namely that the free electrons have a Maxwellian velocity distribution. Setting the quantum-mechanical Gaunt factors equal to one and replacing the sum over discrete energy levels by an integral[†], results in the classical expression for the continuum emission coefficient

$$\left(\varepsilon_{c\nu}\right)_c = \frac{1}{4\pi}\,\frac{128\pi^3}{3\sqrt{3}}\left(\frac{e^2}{hc}\right)^3\left(\frac{h^2}{2\pi m_e}\right)^{\frac{3}{2}}\frac{N_z N_e}{\sqrt{kT_e}}\,z^2 \qquad (28)$$

According to Biberman et al.[13], the approximate formula (28) can be used for an exact representation of $\varepsilon_{c\nu}$ for more complicated systems if it is multiplied by a correction factor $\xi_{z-1}(\nu, T_e)$, giving

$$\varepsilon_{c\nu} = C_1\,\frac{N_z N_e}{\sqrt{T_e}}\,z^2\,\xi_{z-1}(\nu, T_e) \qquad (29)$$

[†] Equation (28) is therefore only applicable for frequencies $\nu < \nu_g$ for which the approximation $\Sigma_n \rightarrow \int dn$ is valid. For neutral argon, $h\nu_g$ can be taken equal to 3.8ev[16], corresponding to $\lambda >$ 3260Å.

where $$C_1 = \frac{1}{4\pi}\,\frac{128\pi^3}{3\sqrt{3}}\left(\frac{e^2}{hc}\right)^3\left(\frac{h^2}{2\pi m_e}\right)^{\frac{3}{2}}\frac{1}{\sqrt{k}} = 5.45 \times 10^{-39} \text{ cgs units.}$$

Using equation (17), the expression for the effective absorption coefficient is obtained as

$$\kappa'_{c\nu} = C_2\,\frac{N_z N_e}{\sqrt{T_e}}\,\frac{z^2}{\nu^3}\,\xi_{z-1}\,(\nu, T_e)\left(\exp(h\nu/kT_e)-1\right), \qquad (30)$$

where

$$C_2 = \frac{16\pi^2}{3\sqrt{3}}\left(\frac{e^2}{hc}\right)^3\left(\frac{h^2}{2\pi m_e}\right)^{\frac{3}{2}}\frac{c^2}{h\sqrt{k}} = 3.69 \times 10^8 \text{ cgs units.}$$

In the literature $\xi(\nu, T_e)$ is known as the Biberman factor, and can be calculated by the quantum defect method[13, 14]. Values of ξ for the neutral rare gases (with the exception of helium) have been calculated by Biberman et al[13] and Schlüter[14]. On the average the value of ξ is close to unity. For argon in the visible region (4000 Å < λ < 7000 Å) $\xi \sim 1.5 - 2.5$ and shows a slight temperature dependence[14]. Experimental determination of ξ for argon from shock tube measurements by Coates and Gayden[15], and arc measurements by Wende[16] agree well with the calculations by Schlüter[14]. For a multiply ionized plasma, the total emission coefficient is obtained by summing (29) over z, i.e.,

$$\varepsilon_{c\nu} = C_1\,\frac{N_e}{\sqrt{T_e}}\sum_z N_z\, z^2\,\xi_{z-1}\,(\nu, T_e) \qquad (31)$$

For the case of a plasma consisting of neutral, singly and doubly ionized particles, equation (31) may be written as

$$\varepsilon_{c\nu} = C_1\,\frac{N_e^2}{\sqrt{T_e}}\,\xi_o\,(\nu, T_e)\left(1 + \frac{2\beta}{\alpha + 2\beta}\,\frac{\xi_1(\nu, T_e)}{\xi_o(\nu, T_e)}\right), \qquad (32)$$

where α and β represent the degree of single and double ionization, respectively.

From (31) the continuum emission for a singly ionized plasma ($\alpha \gg \beta$) is seen to be a sensitive function of electron number density, while being relatively insensitive to the electron temperature. An absolute measurement of continuum intensity therefore yields the free electron number density as long as an estimate of the electron temperature is available. Using the Saha equation (5), an expression for the ratio of total neutral line intensity to the intensity of an adjacent continuum band may be obtained. With the exception of the dependence of ΔE_I on both N_e and T_e, this provides an additional equation for determining T_e.

II. 2. 3c The Effect of Self-Absorption and Finite Frequency Interval on Measured Line Intensities.

As long as an LTE or partial LTE plasma is optically thin to the emitted radiation, there is a one-to-one correspondence between emission coefficients and observable intensities (e.g., equation 15a). If self-absorption is important, the measured intensities must be related to the plasma properties through the solution of (17).

The effective absorption coefficient for bound-bound transitions is given by (24)[†]. $\varphi_{nm}(\nu)$ will in general be sharply peaked

---

[†] For the remainder of II.2, unless otherwise stated, the plasma is assumed to be in partial LTE down to the lowest energy level of interest, ensuring the validity of equations (6), (17) and (24).

at $\nu = \nu_{nm} \equiv \nu_o$, falling rapidly to zero for $|\nu - \nu_o| >$ line half-width. It is therefore a good approximation to write

$$\kappa'_{\ell\nu} = K_o \, \varphi_{nm}(\nu) \tag{33}$$

where

$$K_o = \frac{A_{nm}}{8\pi} \frac{c^2}{\nu_o^2} \, N_n \left(\exp\,(h\nu_o/kT_e) - 1\right) \quad , \tag{34}$$

and consequently

$$\int_{-\infty}^{\infty} \kappa'_{\ell\nu} \, d(\nu - \nu_o) = K_o \quad . \tag{35}$$

The effective continuum absorption coefficient, on the other hand, as given by equation (30) can obviously only be taken as a constant evaluated at ν_o if the frequency interval of interest is small.

In an experimental situation the wave length or frequency interval is, of course, not infinite, but determined, for example, by the combination of monochromator dispersion and exit slit width. For a monochromator in which the detector looks at a frequency interval of 2w at the exit slit, the measured intensity (ignoring optical losses) would be given by

$$I_m = \int_{-w}^{w} I_\nu \, d(\nu - \nu_o) \quad , \tag{36}$$

with I_ν found from (14).

Before we go on to evaluate (36) a great deal can be learned by examining equation (14) more closely. Writing $\exp(-\,{}'_{\nu}L)$, which now is equal to $\exp\,(-\kappa'_{\ell\nu}L)\,\exp\,(-\kappa'_{c\nu}L)$,

as $\left(1 - (1 - \exp\,(-\kappa'_{\ell\nu}L))\right)\left(1 - (1 - \exp\,(-\kappa'_{c\nu}L))\right)$, we find that (14) can be expressed in the following form

$$I_\nu = I_{p\nu} \left(1 - \exp\left(-\kappa'_{\ell\nu} L\right)\right) + I_{p\nu} \left(1 - \exp\left(-\kappa'_{c\nu} L\right)\right)$$
$$- I_{p\nu} \left(1 - \exp\left(-\kappa'_{c\nu} L\right)\right) \left(1 - \exp\left(-\kappa'_{\ell\nu} L\right)\right) \quad . \tag{37}$$

Inserting this expression into (36) we now see clearly that the intensity measured by our gedanken detector is made up of:

1. Line emission with self-absorption included, as if continuum emission were not present.
2. Continuum emission with self-absorption included, as if line emission were not present.
3. A term which can be thought of as either
   a) the effect of the continuum absorption coefficient on the line emission, or
   b) the effect of the line absorption coefficient on the continuum emission.[†]

Determination of T_e by the method described in section II. 2. 3a, involves the measurement of the total relative line intensity. Subtraction of the underlying continuum is, in practice, done by making two intensity measurements, one with the frequency interval of the measuring instrument centered at ν_o , and the other far enough away to eliminate the effects of the line wings, but close enough to ν_o so that the continuum emission coefficient

---

[†] Which demonstrates the power of adding and subtracting 1 to make equations yield what previously has been "hidden".

can be assumed constant. Subtracting two such measurements, we find from (36) and (37)

$$\frac{I_{\ell m}}{I_{p\nu_o}} = \exp\left(-\kappa'_{c\nu_o} L\right) \int_{-w}^{w} \left(1 - \exp\left(-K_o L\, \varphi_{nm}(\nu - \nu_o)\right)\right) d(\nu - \nu_o)\,, \tag{38}$$

where $I_{p\nu_o}$ and $\exp(-\kappa'_{c\nu_o} L)$ are $I_{p\nu}$ and $\exp(-\kappa'_{c\nu} L)$ evaluated at $\nu = \nu_o$, and assumed constant over the range of integration. This is a good approximation due to the fact that $\exp(-K_o L\, \varphi_{nm}(\nu - \nu_o)) \rightarrow 1$ rapidly as $|\nu - \nu_o| >$ the line half-width. From equation (38) the importance of including the continuum absorption is clearly seen.

Deducing T_e from line intensities using equations (25) and (26) is based on the assumption that the plasma is 1) optically thin, and 2) the entire line emission is included. If these two criteria are met, equation (38) reduces to

$$\frac{\left(I_{\ell m}\right)^{\text{opt. thin}}_{w/b_c \rightarrow \infty}}{I_{p\nu_o}} = \frac{I_\ell}{I_{p\nu_o}} = K_o L\ .$$

In an actual plasma, however, the measured line intensity is usually less than this, the ratio of the two being given by

$$\frac{I_{\ell m}}{I_\ell} = \frac{\exp\left(-\kappa'_{c\nu_o} L\right)}{K_o L} \int_{-w}^{w} \left(1 - \exp\left(-K_o L\, \varphi_{nm}(\nu - \nu_o)\right)\right) d(\nu - \nu_o)\,. \tag{39}$$

In general $\varphi_{nm}(\nu - \nu_o)$ would be given by the Voigt profile[8, 9]. In this case, with $w \rightarrow \infty$, the integral in (39) reduces to the well known curves of growth[8, 9]. Numerical integration of (39) for finite w should pose no problem, however, with modern computers.

If Stark broadening is the dominant effect (as is the case in the present experiment), $\varphi_{nm}(\nu)$ is given by equation (7). Evaluation of (39) is now quite simple, and will be outlined below. Combining (7) and (39) and making the change of variables

$$z = \frac{K_o L}{2\pi b_c} , \quad x = \frac{\nu - \nu_o}{b_c} ,$$

(39) can be written in the following form:

$$\frac{I_{\ell m}}{I_\ell} = \exp\left(-\kappa'_{c\nu_o} L\right) \frac{g\ (w/b_c,\ z)}{z} \tag{40}$$

with

$$g\ (w/b_c,\ z) = \frac{1}{2\pi} \int_{-w/b_c}^{w/b_c} \left(1 - \exp\left(-\frac{2z}{1+x^2}\right)\right) dx . \tag{41}$$

Let us look at $g(w/b_c, z)$ in the limit as $w/b_c \to \infty$. Then following Ladenburg[17], the integral can be written as

$$\frac{1}{2\pi} \int_{-\infty}^{\infty} \left(1 - \exp\left(-\frac{2z}{1+x^2}\right)\right) dx \equiv f(z) = z \exp(-z)\left(J_o(iz) - i\, J_1(iz)\right) \tag{42}$$

where $J_o(iz)$ and $J_1(iz)$ are the Bessel functions of orders zero and one, with complex arguments. Combining (40), (41), and (42), we may now write

$$\frac{I_{\ell m}}{I_\ell} = \frac{f(z)}{z} \exp\left(-\kappa'_{c\nu_o} L\right) \frac{g(w/b_c, z)}{f(z)} . \tag{43}$$

Here $f(z)/z$ represents the self-absorption correction to the total line intensity for $w/b_c \rightarrow \infty$, and is shown in figure 15. The factor $\exp(-\kappa'_{c\nu_o} L)$ represents the added correction of emitted line radiation due to absorption in the underlying continuum. The ratio $g(w/b_c, z)/f(z)$ represents the effect of finite w/b_c, and is plotted in figure 16. When self-absorption effects are small (i.e., $z < 0.1$, say),

$$\frac{g\,(w/b_c, z)}{f\,(z)} \simeq \frac{\tan^{-1}(w/b_c)}{\pi/2} \tag{41a}$$

which is identical to the right hand side of (8). Equation (43) and figures 15 - 18 show that the error caused by neglecting w/b_c and/or absorption due to continuum are not necessarily negligible. If the continuum corrections can be neglected, and self-absorption effects are small but not negligible ($z = 0.4$, say), then even for $w/b_c = 10$, 8% of the line radiation falls outside $\nu_o \pm w$. Previous authors (References 15 and 18) apparently did not include this effect, even though the value of w/b_c reported was of the order of (or less than) 10.

II. 2. 3d Evaluation of the Effects of Self Absorption and Finite w/b_c

The effect of self-absorption on continuum emission can be found by evaluating (14)[†] with $\kappa'_\nu L = \kappa'_{c\nu} L$, taking $\kappa'_{c\nu}$ from equation (30). Since knowledge of $\xi_z(\nu, T_e)$ (both theoretical and experimental) is limited to <u>neutral</u> argon, only the case of a singly

---

[†] Having made use of equation (17) to replace ϵ_ν/κ'_ν by $I_{p\nu}$.

ionized argon plasma ($z = 1$ only, $\alpha \gg \beta$) will be discussed here. The value of $\xi_o(\nu, T_e)$ was found from the measurements by Coates and Gaydon[15], and L was taken as 1.5 cm (the diameter of the cone at the window). Dividing (14) by $\kappa'_{c\nu} L$ results in an expression for the ratio of the actual emitted continuum radiation to the emission expected for an optically thin plasma. This ratio is plotted as a function of N_e and T_e in figures 17 and 18 for $\lambda = 4000$ Å and 7000 Å. It is seen that self-absorption effects are important only for a combination of high electron number density and moderate electron temperature. It is only for $T_e \geqslant 26000^o$K and $N_e \leqslant 10^{18}$cm^{-3} (where the self-absorption effects are small anyway) that the term

$$\frac{2\beta}{\alpha + 2\beta} \; \frac{\xi_1 \, (\nu, T_e)}{\xi_o \, (\nu, T_e)}$$

should be included in the expression for the absorption coefficient.

When Stark broadening is the dominant effect, the non-dimensional parameter $z = K_o L / 2\pi b_c$ is of prime importance for self-absorption in spectral lines. For a plasma in complete LTE, equation (34) may be written as

$$K_o = \frac{A_{nm}}{8\pi} \frac{c^2}{\nu_o^2} \frac{N_o}{Z_o} g_n \left(1 - \exp(-h\nu_o / kT_e)\right) \exp(-E_m / kT_e), \quad (44)$$

where n and m denote the upper and lower states, respectively. Note that in references 15, 18 and 19 the integrated absorption coefficient is given incorrectly as

$$K_o = \frac{A_{nm}}{8\pi} \frac{c^2}{\nu_o^2} \frac{N_o}{Z_o} \frac{g_n}{g_m} \left(1 - \exp(- h\nu_o / kT_e)\right) \exp(-E_m / kT_e),$$

which by comparison with (44) has an extra factor of $1/g_m$. Since g_m can often be as large as 7, and Coates and Gaydon[15] found that large self-absorption corrections were necessary for some of their measured line intensities, the estimated errors on some of their transition probabilities must be accepted with some doubt. Figure 9 shows $K_oL/2\pi$ as a function of T_e computed for the 6965.4 and the 7067.2 Å neutral argon lines[†], with L taken as 1.5 cm. Values of N_o (total neutral number density) and Z_o (neutral partition function) as a function of T_e (electron temperature) and p (pressure) were taken from the equilibrium calculations described in Appendix A. Values of A_{nm}, g_n and E_m were taken from reference 20.

The simplest way of obtaining the electron temperature in an LTE plasma is the two line relative intensity technique. Letting subscripts 1 and 2 denote the quantities associated with each line, we see from a double application of (25) that

$$\frac{I_{\ell_1}}{I_{\ell_2}} = \frac{\left(A_{nm}\ h\nu_{nm}\ g_n\right)_1}{\left(A_{nm}\ h\nu_{nm}\ g_n\right)_2} \exp\left(-\frac{E_{n1} - E_{n2}}{kT_e}\right) \ . \tag{45}$$

Since the quantities A_{nm}, ν_{nm}, g_n and E_n are all known, a simple measurement of the emitted radiation at frequencies $\left(\nu_{nm}\right)_1$ and $\left(\nu_{nm}\right)_2$ suffices to determine T_e, provided:

1. the plasma is optically thin for the radiation at both frequencies.
2. the entire line radiation is included in the measurements.

[†] The curves for the two lines do not coincide, but the difference between them is less than the width of curve trace.

From the discussion in the previous section, however, we know that in an actual plasma, neither 1. nor 2. will in general be satisfied.

Assuming that the measurements are performed by an instrument that accepts a frequency range of 2w, we see from a double application of (43) that the intensity ratio we actually measure is given by

$$\frac{(I_{\ell m})_1}{(I_{\ell m})_2} = \frac{I_{\ell 1}}{I_{\ell 2}} \cdot \frac{\left(\frac{f(z)}{z} \exp\left(-\kappa'_{c\nu_o} L\right) \frac{g(w/b_c, z)}{f(z)}\right)_1}{\left(\frac{f(z)}{z} \exp\left(-\kappa'_{c\nu_o} L\right) \frac{g(w/b_c, z)}{f(z)}\right)_2} \quad . \qquad (46)$$

Equation (46) was solved for the ratio of the 6965.4Å and the 4200.7Å neutral argon lines, the result is shown in figure 20. The value for w was taken as 8.5 Å, the effective monochromator exit slit width in the present experiment. This was large enough to necessitate the inclusion of radiation from the neighboring lines of 6960.2Å and 6951.5Å for the 6965.4Å line, and 4190.7Å, 4191.0Å and 4198.8Å for the 4200.7Å line. For the 6965.4Å line this correction was almost negligible, whereas for the 4200.7Å line the contribution from the three lines added almost 50% to the radiation from 4200.7Å line alone. The contribution of the neighboring lines was simply found by successive applications of (43). Accounting for the fact that the neighboring lines were not centered in the 2w range was simply a matter of changing the limits of integration of (41). Both for this and for the final evaluation of (46), the values of b_c are needed. For the 6965.4Å line these were taken as the experimental values discussed in section II, 4. The values of

b_c for the blue lines were found by taking the ratio of Stark half-widths for the 6965.4Å line to that of the blue lines from Griem[7], and then scaling the experimental half-width accordingly.

Referring to figure 20, the effect of self-absorption and finite w/b_c is quite dramatic. Take a case of $p = 1335$ torr and an experimentally measured intensity ratio of 2.5. Assuming the gas to be optically thin and the entire line radiation to be included gives a temperature of 17000°K. Correcting for self-absorption only gives a temperature of 15000°K, whereas the true temperature is 18800°K. The somewhat unexpected effect of having the actual measured line intensity ratio greater than the optically thin ratio is simply due to the fact that Stark broadening of the blue lines is greater than the Stark broadening of the 6965.4 Å line.

II. 3 EXPERIMENT

II 3.1 The GALCIT 6'' Shock Tube

The experiments were performed in the GALCIT 6 inch shock tube[21], a facility designed for the production of strong shock waves under very reproducible conditions. The basic shock tube consists of a 6' long, 6.5'' diameter driver section, a diaphragm transition section, and a 36' long 6'' diameter test section (figure 12). The entire tube is type 321 stainless steel with a 0.5'' nominal wall thickness, and the inside surface is honed to a mirror finish. The reproducibility of the shock waves is achieved through a carefully designed diaphragm opening mechanism. A hydraulic system clamps the diaphragm in the diaphragm transition section, and a set of crossed knife blades mounted across the transition section cuts the diaphragm as the driver pressure is increased. The various diaphragm bursting pressures are repeatable to within a few psia, in general, resulting in shock waves with Mach numbers reproducible to within 1%.

The vacuum system consists of two mechanical pumps and a liquid nitrogen cold-trapped oil diffusion pump. The test section can be evacuated to a pressure of 2×10^{-5} torr in one half hour. With the shock tube isolated from the pumping system, the initial combined outgassing and leak rate is less than 2×10^{-4} torr per hou A thermocouple gauge and a cold-cathode ionization gauge are used to monitor the vacuum level. Initial test gas pressures are set using a calibrated control volume (1/29 of the test section volume) connected to a 0-50 torr, bellows-type Wallace and Tiernan gauge.

Incident shock velocities are measured using two platinum thin film heat transfer gauges mounted flush with the shock tube wall. The time needed for the shock wave to traverse the distance between the two gauges is recorded by a Beckman type 0.1 μsec counter.

Terminating the 6'' shock tube is a 10° half-angle cone, consisting of two sections. The first section (comprising 60% of the convergence length) was made by electroplating nickel to a 3/8'' thickness onto an aluminum mandrel. The second section was made from 2024 aluminum bar stock, using conventional machining methods. A 1/8'' diameter hole remains at the vertex of the cone to allow for insertion of the probe used to measure centerline shock velocities (discussed in part I).

In the present investigation room temperature hydrogen at 230 psia is used as driver gas to produce shock waves of an average initial (prior to entering the cone) Mach number of 10.15 in argon. Initial test gas pressure was 1.5 torr. The schematic shock tube configuration is shown in figure 21.

II 3.2 Spectroscopic Investigation

Provisions were made for mounting windows at x/L = 0.90 in the cone. The necessity of easy removal for cleaning purposes dictated the construction of two aluminum plugs, each with a .070" diameter hole, onto which were epoxied (Resiweld 7004) two quartz windows. The second section of the cone with one set of windows inserted at x/L = 0.90 is shown in figure 22. A small positioning pin on each "plug" aligning the inside window with the cone wall, ensured identical repositioning after removal.

The choice of x/L = 0.90 for the window position was a compromise involving several factors: getting as close to the vertex as possible to maximize the Mach number; having a reasonable cone diameter to minimize the window interference with the shock wave; obtaining sufficient time for a meaningful study of the plasma behind the incident shock; and positioning the window such that it did not coincide with a stemshock intersection point.

The arrangement of the equipment associated with the emission measurements is shown in figure 23. The components and their special uses will be outlined in the following sections.

II 3.2a Time-Integrated Photographic Measurements

The initial phase of the experiment was to determine the overall spectrum of the emitted radiation. The most convenient way of doing this is photographically. Light passing through one of the windows was focused on the entrance slit on a 1.5 meter Jarrell-Ash model 78-090 spectrograph. The reciprocal dispersion in the first order is 10.91 Å/mm at 4000 Å. Isolation of the higher orders was achieved by color filters. The film used was a very high speed Kodak recording film, type 2485, capable of speeds up to 10000 ASA with special handling, although the high speed properties were not essential for the time integrated studies. Even for an entrance slit width of 25μ, a neutral density filter of 0.8 was necessary to avoid overexposure of the film. The spectrograph was calibrated using hydrogen, mercury and argon spectral lamps. This allowed the small deviation from dispersion linearity to be found, so that identification of the shock tube spectrum could be performed quite accurately.

II.3.2b Time-Resolved Photographic Measurements

An attempt was made to produce a time-resolved spectrum through the use of a 1 μsec Kerr-cell shutter. Here, however, even the 10000 ASA speed proved inadequate to produce a spectrum in one exposure. The main reason being the relatively poor transmission of the combination Kerr-cell/polarizers, especially at wave lengths close to 4000 Å.

Ten exposures were sufficient to produce a readable spectrum under certain conditions, but the original plan of using these "snapshots in time" as a means of gaining additional quantitative information on the spectral intensity distribution was abandoned. In the region around 4000 Å, the number of runs necessary would simply have been too impractical. Three Kerr-cell-shuttered spectra were obtained, all at a time close to that of maximum luminosity. Beyond confirming that the spectra seen in the time integrated studies were indeed due to emission behind the incident shock wave, no further results were obtained.

II 3.2c Time-Resolved Photomultiplier Measurements

The advantages of a photomultiplier over photographic techniques in quantitative spectroscopy are many. By its very nature the photomultiplier results in a time-resolved measurement; its response is linear over an extremely large range of intensities; the sensitivity to low light levels is generally greater than that of photographic materials; and finally, it has a very rapid time response. The rise time of any photoelectric detecting system will almost never be limited by the photomultiplier. The principal disadvantage is the limited spectral region that can be monitered by a photomultiplier. One solution to this might be the use of multichannel photoelectric systems. Another is to rely upon the reproducibility of the shock tube (and the endurance of the experimenter), as was the case in the present investigation.

Light from the shock-heated plasma was focused on the entrance slit of a 1/2 meter Jarrell-Ash Ebert type monochromator. The optical train was collimated by two 1 mm optical stops to ensure good spatial resolution. To a good approximation, the light admitted by the monochromator entrance slit originated from a cylindrical slab of plasma less than 1mm in diameter located at right angles to the cone axis. For a typical shock velocity of 8 mm/μsec, this resulted in a shock tube/optical geometry rise time of less than 120 nsec. Neutral density filters were used to avoid over-saturation of the photomultiplier (RCA type 8645 with S-20 spectral response), and color filters provided separation of the various orders of the monochromator. The entrance slit was fixed at 20 μ throughout the investigation. With an exit slit width of 20 μ (equivalent to 0.32 Å, and an actual instrument half-width of 0.5 Å), the profile of the 6965.4 Å neutral argon line was investigated. An exit slit width of 1 mm (equivalent to 17 Å) was used for the relative line intensity measurements.

For the shock tube measurements, the photomultiplier anode current was fed into a 500 Ω load resistor across the input of a home-made amplifier[†] with a gain of 60 and a frequency response that was flat from 10 Hz to 2 MHz. The amplified signal was then monitored by three Tektronix type 555 dual-beam oscilloscopes. The final rise time associated with the photo-electric measurements was less than 130 nsec.

The seemingly excessively large number of oscilloscope traces was deemed necessary in order to gain the most information possible per shock tube run. The traces were recorded at a variety of sweep speeds and voltage settings to minimize the reading errors. Since we were limited to one photomultiplier, this was also a safeguard against wasting a run when a new wave length was monitored for the first time, and the expected photomultiplier output current was unknown.

[†] The author is grateful to Dr. Steve Barker for his help in this matter.

II. 3. 3 Experimental Procedure

Making an accurate quantitative investigation of line intensities and spectral line profiles in a shock-heated plasma when only one photomultiplier is available demands a high degree of reproducibility both of the shock tube and the optical system in general. In the present investigation more than 80 shock tube runs were used to monitor 15 different wave length regions for the relative line intensities, and 34 runs were used to investigate the 6965.4 Å neutral argon line.

The GALCIT 6'' shock tube was designed to produce shock waves with Mach numbers reproducible to within less than 1%. For the spectroscopic investigation this was even improved somewhat to give an initial Mach number of 10.15 with a 0.3% rms deviation. The necessary overall reproducibility was achieved by adherence to a strict schedule prior to each run. The test section was evacuated to 0.03×10^{-3}, torr and allowed to outgas/leak up to 0.05×10^{-3} torr before the test gas was admitted. During this period of outgassing/leaking, typically taking 10 minutes, a final check on the optical alignment and wave length setting of the monochromator was performed. Following this, the test gas was admitted to the desired pressure and within minutes the shock tube was fired.

Setting the monochromator at any desired wave length was achieved through the use of spectral lamps and a 6 inch diameter protractor mounted on the grating adjustment knob. The central line frequency was determined by monitoring the photomultiplier anode current as a function of frequency on a Leeds-Northrup type 8003 recorder. In this manner it was felt that even off-line frequencies could be set to within ±0.03 Å.

Some early measurements of emitted radiation revealed an abnormal drop in intensity after a few runs. Upon removing the windows, it was found that they were almost covered with a "soot like" substance. Measurements of the variation of Mach number at $x/L = 0.90$ using Setchell's[2] velocity probe also revealed a previously unobserved effect. This can be seen in figure 24, which shows the effect on the shock velocities of not cleaning the cone. After 10 runs, the last 20% of the cone was also covered by the same "soot like" substance. Obviously, neither the coating of the windows nor the drop in Mach number could be tolerated in the present investigation.

As a diaphragm bursts, small fragments of it are carried along with the contact surface and eventually settle near the end of the shock tube. In the present case, this meant that small aluminum particles would gather near the vertex of the cone. This was indeed observed, and the "coating" phenomenon was apparently associated with these aluminum fragments. It was found that simply removing the second section of the cone after each run and blowing out the small aluminum particles with an air hose completely eliminated the "coating" problem. As an added precaution towards retaining an identical optical system from run to run, the windows were also cleaned with a strong NaOH solution after each run. Taking these measures resulted in the necessary reproducibility for spectroscopic measurements. It meant, however, that a complete realignment of the optical system was needed after each run, bringing the total turn-around time up to a disagreeable $2\frac{1}{2}$ hours.

II. 3. 4 Data Reduction

II. 3. 4a Calibration of the Optical System

The emitted radiation is measured experimentally by a photomultiplier monitoring the intensity at the exit slit of a monochromator. The frequency or wave length range $\Delta\lambda$ "seen" by the detector is determined by the monochromator dispersion and the exit slit width. Let $i(\lambda_o)$ denote the photomultiplier output current with the monochromator centered at a wave length λ_o . Then $i(\lambda_o)$ is related to the shock tube luminous intensity I_λ by

$$i(\lambda_o) = \int_{\Delta\lambda} I_\lambda \quad \eta_w(\lambda, t) \cdot \eta(\lambda) \cdot \theta_1 \, d\lambda \quad , \tag{47}$$

or assuming $\Delta\lambda \ll \lambda_o$

$$i(\lambda_o) = \eta_w(\lambda_o, t) \cdot \eta(\lambda_o) \cdot \theta_1 \cdot \int_{\Delta\lambda} I_\lambda \, d\lambda \ . \tag{48}$$

Here θ_1 accounts for the solid angle admitted by the entrance slit; $\eta_w(\lambda_o, t)$ accounts for the possibility that the transmission of the window exposed to the plasma may vary as a function of time; $\eta(\lambda_o)$ is a product of the transmissions of all the lenses and filters, the losses associated with the monochromator, and the sensitivity of the photomultiplier. The calibration of this optical system was performed by removing the second section of the cone and placing a calibrated tungsten strip lamp on the cone axis. Viewing the tungsten filament through the identical optical system, we may write

$$i_{s\ell}(\lambda_o) = I_{s\ell}(\lambda_o) \cdot \eta(\lambda_o) \cdot \eta_w(\lambda_o, t_o) \cdot \theta_2 \tag{49}$$

for the photomultiplier current associated with the lamp. Here θ_2 denotes the fact that even though the tungsten strip lamp was seen through the shock tube window, the geometry of the lamp meant that the solid angle accepted was different. $\eta_w(\lambda_o, t_o)$ indicates that the recording of the tungsten strip lamp current as a function of λ was done at one specific time. The intensity $I_{s\ell}(\lambda_o)$ of the tungsten strip lamp is given sufficiently accurately $(\Delta\lambda \ll \lambda_o)$ by

$$I_{s\ell}(\lambda_o) = I_{p\lambda}(\lambda_o, T_{s\ell}) \cdot \epsilon_{s\ell}(\lambda_o, T_{s\ell}) \cdot \Delta\lambda \quad . \tag{50}$$

Here $I_{p\lambda}$ is the Planck function in wave length notation, $T_{s\ell}$ is the true temperature[22] of the tungsten filament, and $\epsilon_{s\ell}$ is the emissivity[23] of the tungsten ribbon. The tungsten strip lamp was calibrated with an optical pyrometer[†], giving the color temperature as a function of lamp current. References 22 and 23 give the necessary relationships between color temperature, true temperature, and the tungsten emissivity. Taking the ratio of (47) and (48), we find

$$I(\lambda_o) \equiv \int_{\Delta\lambda} I_\lambda d\lambda = I_{s\ell}(\lambda_o) \frac{i(\lambda_o)}{i_{s\ell}(\lambda_o)} \cdot \frac{\eta_w(\lambda_o, t_o)}{\eta_w(\lambda_o, t)} \cdot \frac{\theta_2}{\theta_1} \quad . \tag{51}$$

The values of $\eta_w(\lambda_o, t)$ were found by measuring the photomultiplier output at the wave length in question, first through the window, and then through a dummy window holder identical to the ones used in the cone but without any window. In principle any light source could be used for this relative measurement, but in practice it was found convenient to use the tungsten strip lamp. The transmission of a new window exposed to the plasma was found to decrease from typically 0.9 to 0.8 within a few runs, and thereafter experience a very gradual and slow decrease down to

---

[†] The assistance of Mr. O'Connor at the Standards Laboratory at J. P. L. is gratefully acknowledged.

typically 0.76. There were two probable reasons for this: 1) it was not possible to completely eliminate the "coating" effect described in the previous section, 2) the windows became slightly scratched as time progressed, presumably due to the aluminum fragments from the diaphragm.

Knowledge of θ_2/θ_1 would now suffice to determine the absolute intensity of the emitted radiation. In the present experiment, however, relative measurements were used whenever possible. From (51) we see that

$$\frac{I(\lambda_1)}{I(\lambda_2)} = \frac{I_{s\ell}(\lambda_1)}{I_{s\ell}(\lambda_2)} \cdot \frac{i(\lambda_1)}{i(\lambda_2)} \cdot \frac{i_{s\ell}(\lambda_2)}{i_{s\ell}(\lambda_1)} \cdot \frac{\eta_w(\lambda_1, t_o)}{\eta_w(\lambda_2, t_o)} \cdot \frac{\eta_w(\lambda_2, t_i)}{\eta_w(\lambda_1, t_j)} \cdot \qquad (52)$$

Here all the factors on the right hand side are either measured or, in the case of $I_{s\ell}$, found from knowledge of the Planck function and tungsten emissivities. The factor on the left hand side can be related to the plasma properties through the equations developed in section II. 2.

II. 3. 4b Treatment of Oscilloscope Traces

The experimental quantity measured as not the photomultiplier anode current but the corresponding voltages recorded on oscillograms. Rather than reading data directly from the traces, it was decided to digitize the information by mounting the polaroid pictures on a Hewlett Packard x-y recorder and follow the trace with a set of cross hairs. The voltage inputs to the x-y recorder required to set the cross hairs were digitized, stored on magnetic tape, and processed by an IBM 360/75 computer. A typical oscilloscope trace is shown in figure

25. The y coordinates, corresponding to the emitted intensity, were normalized according to the procedure outlined in the previous section. The x coordinates, proportional to time, were first corrected for variation in sweep speeds associated with the various oscilloscopes, and then normalized with the initial shock velocity. After this normalization and scaling, the oscilloscope traces were essentially retraced by a CalComp plotter on a greatly expanded scale. An example of the finished result is shown in the lower portion of figure 26. The apparent double trace is the result of treating two oscilloscope traces of different voltage sensitivity and different time scale. It is included here only to show the accuracy and reproducibility of the digitizing technique. The upper figures show the result of smoothing the recorded profile, in order to reduce the quantum noise from the photomultiplier, and the electronic noise associated with the amplifier. A common time base for all the traces was found by taking the arrival of the reflected shock wave at the window position to coincide for all profiles. This point is the almost vertical increase of the intensity at t = 30 μsec. The discrepancy between the lower and upper trace of run number 1657 is not real. An error in the initial data reduction program caused 2 μsec to be subtracted from all the normalized times. This was later corrected, but the unsmoothed profiles were not replotted.

Figure 16 also shows the noticeable effect of shifting the observed wave length region from a position centered on a spectral line to one where only continuum intensity was observed.

II. 4 EXPERIMENTAL RESULTS

II. 4. 1 The Shock Wave

With initial conditions $p_1 = 1.5$ torr argon, $p_4 = 230$ psia hydrogen, and $T_1 = 298^{\circ}K$ the shock Mach number measured upstream of the entrance to the cone was 10.15, with a 0.3% rms deviation. Using the velocity probe designed by Setchell[2], the Mach number at $x/L = 0.9$ was found to have increased to 23.7. Equilibrium conditions behind a shock wave of this Mach number were calculated (for details see appendix A). The resulting plasma should be 47% singly ionized, with an electron number density of 2.92×10^{17} cm^{3} and electron temperature of $14400^{\circ}K$. Relaxation times estimated from reference 3 were of the order of 0.3 μsec. As the reflected shock wave emerges from the cone and propagates upstream, it collides with the approaching contact surface. The resulting wave pattern consists of a transmitted shock wave, and a rereflected shock wave (followed by a new contact surface) propagating back into the cone. The arrival of this shock wave at $x/L = 0.90$ determines the available test time. Figure 27 shows the emission from the H_{α} line on a long time base. The first light pulse is due to emission behind the incident and reflected shock waves. The appearance of the second pulse signifies the arrival of the rereflected shock wave at the window position. The available test time is seen to be of the order of 600 μsec, clearly sufficient to have no influence on the plasma parameters determined during the first hundred microseconds.

II. 4. 2 Time-Integrated Spectrum

A portion of a typical time-integrated spectrum is shown in figure 28. Since the main purpose of the time-integrated study was to determine what lines were sufficiently intense to warrant time-resolved study, a detailed investigation of the spectrum was not performed. Beyond the expected neutral argon lines, the spectrum is largely comprised of the typical shock tube impurities of Ca, Cr, Fe, Na and Al. Inspection of the neutral argon lines revealed that they were appreciably broadened and shifted. The strong continuum radiation is primarily a result of the (later-determined) elevated electron number densities just before and after the reflected shock wave. The absence of ionized argon lines, or rather the inability to detect them in the spectrum, was at first puzzling. Lines that were initially thought to be from ionized argon had to be rejected due to the presence of strong impurity lines at almost identical wave lengths (e. g., 4226.7 Å Ca_I and 4226.9 Å A_{II}). When the variations of electron temperatures and electron number densities as a function of time were found by relative line measurements and Stark broadening, it became clear that only for a short time interval prior to and after the passage of the reflected shock wave would the ion lines be sufficiently intense to dominate the emitted radiation[†]. The time-integrated study served its purpose, however, as it enabled determination of neutral argon lines sufficiently strong to stand out against the background continuum intensity.

[†] A series of three runs were made monitoring the 4806.0 Å A_{II} line, confirming this.

II.4.3 A Study of the 6965.4 Å Neutral Argon Line

Before relative line measurements were made, it was decided to obtain the line profile of one neutral argon line. The reasons for first undertaking this measurement were two-fold. Since only one wave length would be monitored per shock tube run, this measurement would be a severe test of the overall repeatability of both the shock tube and the photoelectric/optical detection system. Secondly, the ratio of slit width to line half-width is a critical factor in obtaining meaningful results in total line intensity measurements. Measurements of the line half-width would therefore give an indication of the effective slit-width that should be used in the line measurements.

The 6965.4 Å neutral argon line was chosen for this study on the basis of its brightness in the time-integrated spectrum, and available theoretical information on its half-width and shift. A total of 34 runs were made with the monochromator exit slit set at 20 μ. Figure 29 shows oscilloscope traces with the monochromator adjusted to (6965.4 + 0) Å and (6965.4 - 2.0) Å respectively. The effect of Stark broadening on the spectral intensity is evident. Figures 30-32 give the resulting line profiles at various times after the shock passes $x/L = 0.90$. The data were reduced and normalized according to the procedure described in section II 3.4. Figure 30 shows all the data at 25 and 70 μsec, respectively. The equivalent width of the oscilloscope trace is also indicated. The largest deviations from run to run were anticipated close to the maximum intensity where the line profile is steepest. The fact that even here the run-to-run scatter hardly exceeds the equivalent width of the oscilloscope trace is a measure of the reproducibility of the shock tube and measuring system as a whole. The curve labeled 'monochromator broadening' was determined by scanning the 6965.4 Å line emission from an argon spectral lamp. The only broadening expected there would be the natural broadening, which is of the order of 10^{-4} Å. The resulting profile is therefore an adequate representation of the monochromator/photomultiplier response to a delta-function intensity input. Figures 31 and 32 show the data points averaged and the continuum subtracted. The arrows indicate the full half-widths. Corrections due to instrument broadening, finite w_b/b_c^m (refer to figure 14), and self-absorption, and reduction of half-widths to electron number densities are discussed in the following section. Keeping in mind, however, that the half-width and line shift are only weakly dependent on temperature and almost directly proportional to electron number densities, the general trend is clearly seen. Figure 31 shows that the line broadens and shifts progressively further into the red as a function of time behind the incident shock wave. This process is reversed in figure 32, which gives the line profiles at various times after the reflected shock wave passes the window.

II. 4. 4 Determination of Electron Number Density

II. 4. 4a Stark Broadening

The electron number density could in principle be found from either the measured half-width (the linear Stark effect) or the measured line shift (the quadratic Stark effect). Using the line shift is the most appealing method from the experimental standpoint, since the line profiles in figures 31 and 32 would not have to be corrected for instrument broadening or self-absorption. However, the use of shifts in argon is only recommended if they are as large or larger than the half-widths[9]. The line profiles shown in figures 31 and 32 must be corrected before meaningful half-widths can be determined. Since neither the measured line nor the monochromator broadening have a Gaussian type distribution, unfolding of the convolution integral below is, in principle, required.

$$\varphi_m(\nu-\nu_o) = \int_{-\infty}^{\infty} \varphi_o(\nu'-\nu_o)\ \varphi_\ell((\nu-\nu_o)-(\nu'-\nu_o))\, d(\nu'-\nu_o)\ . \qquad (53)$$

Here φ_m is the measured line shape, φ_ℓ the true line shape and φ_o the monochromator broadening. In practice, the solution of (53) is usually done by matrix operation. Let L_ℓ, L_m, and L_o be the matrix representations of the true line profile, the measured profile, and the monochromator broadening effect, respectively. The matrix representation of (53) is then given by

$$L_m = L_o L_\ell \quad , \qquad (54)$$

and L_ℓ is found by inversion of (54) to be

$$L_\ell = L_o^{-1} L_m \quad . \qquad (55)$$

For the range of electron temperatures and electron number densities expected in the present investigation, the dominant broadening is due to the Stark effect. The true line shape is therefore, to a good approximation, given by a Lorentzian profile. Performing the matrix operation indicated in (54), the effect of the monochromator broadening on a series of Lorentzian-type profiles were computed. Three of these are shown in figure 33a, with the increase in half-width due to the monochromator broadening indicated. The effect of self-absorption on a Lorentzian-type line profile can be found by combining equations (7), (14) and (33), and is shown in figure 33b. Part (i) of the figure represents $\kappa'_\nu L$ for a Lorentzian line profile for various z ($z = K_o L/2\pi b_c$), keeping b_c constant. Part (ii) is simply a graph of $(1-\exp(-\kappa'_\nu L))$ vs. $\kappa'_\nu L$, with the dashed line indicating the optically thin result. Part (iii) shows the resulting distribution of line intensity, normalized by the Planck function $I_{p\nu}$. The effect of self-absorption on both the line profile and apparent half-width is seen to increase with increasing value of z.

Since complete knowledge of the line profile is not necessary for determining electron number densities, the matrix inversion process indicated by equation (55) was not performed. The true line profile was instead assumed to be Lorentzian, and the correction to the measured half-width was taken from the appropriate curves, similar to the ones shown in figures 33a and 33b. Corrections due to the finite value of w_b/b_c^m (discussed in section II. 2. 2) were also included in the final evaluation of half-widths.

The values of z needed for the self-absorption corrections were taken from the results of the temperature self-absorption corrections discussed in section II. 4. 5c. Since these latter corrections depend upon the half-width of the 6965. 4 Å line, the process is an iterative one. A complete account of the self-absorption iteration scheme is given in section II. 4. 5c. The electron temperatures, which are needed before the half-widths can be converted into electron number densities, were also taken from this section.

The resulting electron number density as a function of time is shown in figure 34. The number densities were normalized by the value of N_e at $t = 5$ μsec after the incident shock passed the window. The reason for this and estimates of the absolute values of N_e will be discussed in section II. 4. 4c.

II. 4. 4b Continuum Intensity

In order to obtain electron number densities from continuum emission, the absolute intensity must be measured. Since relative measurements were used throughout the present investigation, only relative values of the electron number densities are directly available. From equation (32) of section II. 2 we see that although the electron number density is only weakly dependent upon the temperature, an estimate of T_e is needed. Since the temperature depends upon self-absorption corrections, which in turn depend peripherally on N_e, an iteration process involving both N_e and T_e must, in principle, be performed. This was done as a self-consistency control of the self-absorption corrections described in this chapter, and is discussed in Appendix B. The relative values of N_e shown in figures 34 and 38 were instead determined in the manner described below.

Using measured intensities and T_e from section II. 4. 5c, values of N_e/N_e (t = 5 μsec) were found from equation (32) (with $\alpha \gg \beta$). Absolute values of N_e were found using the results from section II. 4. 4c, and the continuum intensities were then corrected for self-absorption using figures 17 and 18. These corrected intensities were then employed to find corrected values of N_e. Repeating the process twice was found to give sufficient accuracy. The resulting relative electron number densities based on continuum emission at 4130 and 7000 Å are shown in figures 34 and 37. As will be mentioned in section II. 5. 2, experimentally determined values of the electron temperatures during the first 10 μsec after the reflected shock wave are not available. Since the temperature appears as $(T_e)^{1/4}$ in equation (32), however, a straight line extrapolation of the temperature vs. time curve on figure 37 was felt to be sufficient to give an estimate of N_e during these 10 μsec. The increasing difference between N_e/N_e(t = 5 μsec) as found from the continuum at 4130 and 7000 Å will be discussed in section II. 5. A prominent feature of the electron number densities as found from the continuum intensity measurement is the rapid exponential decrease behind the reflected shock wave, apparently followed by a second and a third exponential fall off, but with different time constants. The significance of this will be discussed further in section II. 5.

II. 4. 4c Absolute Electron Number Densities

The accuracy of Griem's[7] theoretical expression for the Stark half-width of the 6965. 4 line is not known. Gericke[23] measured Stark half-widths of several argon lines around 4000 Å and found agreement to within 20% with Griem's theoretical values. Unfortunately Gericke[23] only measured the Stark shift of the 6965. 4Å line. In comparison with his measurement, the theoretical prediction was found to be too large by a factor of 1. 5. The value of N_e at t = 2. 5 μsec (from the Stark width) was found to be 9.5×10^{16} cm^{-3}, in contrast with the estimated value of 2.92×10^{17} cm^{-3} based on equilibrium conditions behind the incident shock wave. Even allowing for a correction similar to the one Gericke[23] found for the line shift, there is still a large discrepancy. Before any conclusions are drawn concerning the accuracy of either the measurements or the theory, an additional important point must be considered. The gas passing the window at t = 2. 5 μsec was not processed by a shock wave of Mach number 23. 7 corresponding to the measured shock velocity at x/L = 0. 9. Extrapolating backwards in time shows that it originated at x/L = 0. 88, where the centerline Mach number was 19. 7. Equilibrium conditions based on this shock strength are $T_e = 13100^\circ K$ and $N_e = 1.52 \times 10^{17}$ cm^3!

The presence of H_α radiation (seen in the time-integrated spectrum) was used to obtain a profile of the H_α line. Since the H_α emission prior to the contact surface is due to inherent impurities in the test gas, the emitted radiation was measurably stronger than the continuum intensity only for the first few microseconds. It was sufficiently strong to obtain a profile of the H_α line at 2.5 μsec, and the half-width was found to be 11 ± 1 Å. Converting this to electron number density yields the value $1.35 \pm 0.15 \times 10^{17}$ cm^{-3}.

The normalization procedure outlined in section II.3.3 allows for absolute intensity measurements if the ratio of θ_2/θ_1 is known. This ratio was estimated from the geometrical configuration, and the absolute continuum intensity at 7000 and 4000 Å at $t = 2.5$ μsec was determined. Using values of ξ found from the measurements by Coates and Gayden[15], and the electron temperature determined from the relative line intensity measurements (13350°K) results in a value of $N_e = 1.30 \times 10^{17}$ cm^{-3} from the continuum at 7000 Å, and $N_e = 1.41 \times 10^{17}$ cm^{-3} from the continuum at 4000 Å.

In light of the above considerations it was decided that the state of the gas passing the window at 2.5 μsec corresponded closely to gas shocked at $x/L = 0.88$. The absolute value of N_e at 2.5 μsec was taken as 1.4×10^{17} cm^{-3}, the average of the values mentioned above.

The reason for plotting normalized electron number densities was mentioned in section II.4.4b. It might appear more consistent to normalize by the value of N_e at $t = 2.5$ μsec. The Stark half-width at 2.5 μsec, however, was not felt to be as accurate as the ones at later times. Normalizing by N_e at $t = 5$ μsec.

also gave better agreement between N_e as determined by Stark broadening and continuum intensities. Using an average value of the ratio of N_e (5 μsec)/N_e(2.5 μsec) from continuum measurements gives a value of N_e (5 μsec) = 1.98×10^{17} cm^{-3}, which should be used in converting values from figures 34 and 37 to absolute electron number densities.

II. 4. 5 Determination of Electron Temperature Using Relative Line Intensities of Neutral Argon Lines.

II. 4. 5a Line Intensity Measurements

The theoretical background for determining electron temperatures from relative line intensities was discussed in section II. 2. 3. In principle, one need only measure the intensity of two lines to infer the electron temperature. However, in order to minimize errors associated with experimental scatter and uncertainties in transition probabilities, it is advisable to use several lines and find an average temperature. In the present investigation a series of 85 shock tube runs were made, and with the monochromator exit slit opened up to 1mm (equivalent to 17Å) the radiated emission from 7 strong neutral argon lines were monitored as a function of time behind the incident shock wave. The choice of an effective slit width of 17Å was a compromise between having w/b_c as large as possible and still avoiding superimposing the radiation from too many neighboring lines. The choice of lines monitored were dictated by: 1) their presence in the time-integrated spectrum, 2) available data on transition probabilities, and 3) the importance of having a large difference in the upper energy levels of the lines.

In the red we used the 6965. 4 Å and 7067. 2 Å lines with the upper energy level in the 107000 cm^{-1} range. With the monochromator set at 7000 Å and 6918 Å, the corresponding continuum intensity was monitored. In the blue we used the 4200. 7 Å, 4198. 3 Å and 4158. 6 Å lines with upper energy levels in the 118000 cm^{-1} range. The corresponding settings for continuum intensities were 4240, 4130, 4105 and 4000 Å . In addition, two lines in the red but with upper energy levels in the 118000 cm^{-1} range were also measured. These were the 6871.3 and 6752.8 Å lines with continuum at 6785 and 6730 Å. The effect of weak neighboring lines were accounted for in all the measurements by the method described in section II. 2. 3d.

Figure 25 gives typical oscilloscope traces. Each picture shows the photomultiplier output with the monochromator set at the indicated wave length. The only difference in the upper and lower beam is the voltage sensitivity. The upper and middle pictures are from the same run, showing the effect of different time scales. The importance of having a variety of voltage sensitivities and time scales is obvious. In the top two pictures, for example, the upper beam in the upper picture would be used for times after the incident shock passed the window (the incident shock arrival is seen as the first small "glitch" in the trace). The lower beam of the middle picture would be used for times shortly after the reflected shock wave, while the upper beam on the same picture would be used for later times. Figure 35 gives two examples of the traces from the third oscilloscope. Here the lower beams show the photomultiplier output when displayed at 1 μsec/cm. The two small, vertical "discontinuities" at approximately 2 and 2.5 μsec in the 7067.2 Å case, and approximately 3.2 and 3.7 μsec in the 4158.6 Å case were taken to be associated with the stemshock and the center shock passing the window. Referring to figure 11 we see that a stationary observer sitting to the left of a stemshock intersection point would first see the stemshock and then, a short time later, the center shock. The two initial discontinuities occurred distinctly in all the traces, and were well correlated with the arrival of the shock wave at $x/L = 0.90$ found by using the velocity probe from reference 2.

II. 4. 5b The Optically Thin Case

A minimum of 3 and a maximum of 7 runs were made at each wave length. Grouping the runs at one wave length, the oscilloscope traces were reduced and normalized as described in section II. 3. 4. Values were then taken from the CalComp plots every 2.5 μsec up to 40 μsec, and every 5 μsec from then on with additional readings at 3.75, 16.25, 18.75, 31.25, 33.75, 42.5, 52.5 and 57.5 μsec, and a simple averaging performed at each time. The electron temperature as a function of time was first determined under the assumptions that 1) the gas was optically thin, and 2) the entire line emission was measured by the effective exit slit width of $2w = 17$ Å.

The effect of weak neighboring lines was included by assuming their line shape to be Lorentzian, and compute the fraction of their radiation "seen" by the exit slit (half-widths of these lines were appropriately scaled by the method described in section II. 2. 3c). Following the method outlined in section II. 2. 3a, the values of $\ln(I_{\ell m}/A_{nm}\, g_n\, \nu_{nm}\, \psi)^{\dagger}$ were plotted versus E_n/k.

[†] Values of g_n, E_n and A_{nm} were taken from reference 20, and ψ is the correction factor accounting for neighboring lines.

A least-squares straight line was fitted through the points, and the slope was taken as $-1/(T_e)_{\text{optically thin}}$.

II. 4. 5c Correction Due to Self-Absorption and Finite w/b_c.

Assuming full LTE, the optically thin temperatures defined above and electron number densities from Stark broadening and continuum intensities determine a first estimate of the complete thermodynamic conditions. In principle, a series of curves similar to those of figure 20 could then be prepared, one for each possible relative line intensity combination, and an iterative process of self-absorption corrections could be carried out. Besides being a rather formidable project, this method also has the disadvantage of requiring full LTE to relate total neutral number density, Stark half-width and pressure to electron number density and temperature. Instead, an absorption correction scheme was developed that essentially eliminated the use of the full equilibrium equations relating T_e, N_e, N_o and p. This method relies almost entirely upon the measured quantities, and the only equilibrium restriction is that partial LTE exists above the lowest energy level of interest to ensure the validity of equations (6), (17) and (24). For the present experiment, this meant partial LTE above the 1st excited level.

Let the ratio of absolute measured intensity ($I_{\ell m}$) to normalized relative intensity (V) be denoted by ζ. The normalization procedure outlined in section II. 4. 3c allows ζ to be determined if the ratio of θ_2/θ_1 is known. Using the same value of θ_2/θ_1 employed to find absolute continuum intensities, the absolute measured intensity of the 6965.4 Å line at $t = 2.5$ μsec was determined to be 1.56 x 10^7 (cgs units). The final value of electron temperature at 2.5 μsec found by the self-absorption corrections discussed in Appendix B was 13300°K. Using $N_e = 1.4 \times 10^{17}$ cm^{-3} (from section II.4.3c), the measured value of Stark half-width, and equations (25) and (43), the value of emitted radiation that should have been measured was computed to be 1.59 x 10^7 (cgs units). The relatively small difference between prediction and experiment lent credibility to the experimentally determined value of ζ and the self-absorption correction scheme given below.

1. "Correct" the measured relative intensities of the 6965.4 and 4200.7 Å lines to fall on the least-squares straight line fit to all the measured intensities.
2. Find the absolute intensity of the lines $I^1_{\ell m} = V_1 \zeta$, $I^2_{\ell m} = V_2 \zeta$, where superscripts 1 and 2 stand for the 6965.4 and the 4200.7 Å lines, respectively.
3. Using b_c from Stark measurements (corrected for finite w_b/b_c^m and instrument broadening), determine w/b_c. For times when b_c was not measured, the good agreement between N_e (continuum) and N_e (Stark) was relied upon to interpolate for b_c. The first time through, the self-absorption correction to b_c was neglected.
4. Solve

$$\frac{V_1}{V_2} = \frac{\left(A_{nm}\ h\nu_{nm}\ g_n\right)_1}{\left(A_{nm}\ h\nu_{nm}\ g_n\right)_2} \exp\left(-\ \frac{E_{n1} - E_{n2}}{kT_e}\right) \frac{\left(g(w/b_c, z)/f(z)\right)_1}{\left(g(w/b_c, z)/f(z)\right)_2}$$

for T_e. This amounts to finding the correction to electron temperature due to finite w/b_c, still assuming the gas to be optically thin.

5.[†] From equation (43), the intensity that should be measured for an optically thin gas is $(I^{1}_{\ell m})_{\text{opt. thin}} = (Ip_{\nu}(T_e)\ K_oL)_1 \times (g(w/b_c, z)/f(z))_1$. Solve this for $(K_oL)_1$ using equation (41a) for $g(w/b_c, z)/f(z)$ for an optically thin gas (the first time through the iteration use $(I^{1}_{\ell m})_{\text{opt. thin}} = V_1\zeta$).

6. Knowing K_oL, find the corrected value b_c and $(f(z)/z)_1$ from figures 15, 16 and 33a.

7. If the temperature determined in step 4 and the values of K_oL, $f(z)/z$ and $g(w/b_c, z)/f(z)$ found from steps 5 and 6 are correct, the equation below should be satisfied:

$$(\text{Actual measured intensity})_1 \equiv V_1\zeta = \left(I_{p\nu}K_oL\right)_1 \left(\frac{f(z)}{z}\right)_1 \left(\frac{g(w/b_c, z)}{f(z)}\right)_1 .$$

If not, determine $\left(I^{1}_{\ell m}\right)_{\text{opt. thin}} = (I_{p\nu}\ K_oL)_1\ \left(g(w/b_c, z)/f(z)\right)_1$, which is the new estimate for the intensity we would have measured in an optically thin gas (including the effects of w/b_c). From this find the corresponding value of the relative line intensity $V_1^{\text{opt. thin}} = (1/\zeta)\ (I^{1}_{\ell m})_{\text{opt. thin}}$ and substitute this new value into the equation in step 4.

8. Repeat steps 4 - 7 until the equation for the actual measured intensity in step 7 is satisfied.

The iteration process was found to converge adequately after 3-4 cycles, and the resulting values of electron temperatures as a

---

[†] The correction scheme in this form assumes that self-absorption for the 4200.7 Å line is negligible, which is the case in the present investigation. Including self-absorption for the 4200.7 Å line would only mean a few more steps.

function of time after the incident shock passes the window are shown in figure 36.

As a self-consistency check a more traditional self-absorption correction process was carried out, and is described in appendix B. The difference in the two schemes amounted to less than 200°K in most cases, and never more than 500°K (at times shortly after the reflected shock wave).

II. 4. 6 Determination of Electron Temperature Using Relative Line to Continuum Intensities

As discussed in section II. 2. 3 this involves the assumption of complete LTE, knowledge of the quantum mechanical correction factor $\xi(\nu, T_e)$ and the reduction in ionization energies before temperatures can be determined. Consequently, this method was felt to be less accurate than using relative line intensities. Nevertheless, the ratio of the 6965. 4 Å line to the adjacent continuum were determined at a few time intervals behind the incident shock wave. With the exception of values for $t = 40$, 42. 5 and 45 μsec, the temperatures were found to lie well within the experimental uncertainty of T_e as found by the relative line intensity method described in the previous section.

II.5 DISCUSSION

II.5.1 Validity of LTE

The existence of LTE, or at least partial LTE above the first excited level is crucial if meaningful interpretation of the measured radiation is to be made in the present experiment. Theoretical conditions for full and partial LTE were discussed in section II.2.1. Substituting the experimentally determined values of N_e and T_e into equations (2) and (3) offers a self consistency check on the assumption of full or partial LTE. With the exception of t = 2.5 μsec, the criterion of equation (2) is amply satisfied at all times. However, since the resonance line is strongly self-absorbed at t = 2.5 μsec the criterion (2) may be relaxed by an order of magnitude[7], resulting in a sufficient electron number density for full LTE at this particular time as well. The criterion (2), however, is necessary but not sufficient for full LTE. A more stringent verification of LTE involves comparing temperatures and electron number densities as determined by different methods. One such comparison might be between T_e and N_e as found from relative and total line intensities, assuming full LTE, and N_e from continuum intensity and Stark broadening, both of which are practically independent of LTE. Another would be between T_e from relative line intensities (requiring only partial LTE) and T_e from relative line to continuum intensities (requiring full LTE). The good agreement between computed and measured absolute intensities of the 6965.4 Å line at 2.5 μsec supports the existence of full LTE at this time. Similar comparisons at later times, combined with the results from the two self-absorption correction schemes and T_e from relative line and relative line to continuum intensities, indicate the existence of full LTE up until the arrival of the reflected shock and during the later stages of the expansion ($t \gtrsim 45$ μsec). The rapid expansion following the reflected shock appears to result in a progression starting from full equilibrium immediately following the reflected shock, to a period of population inversion among the energy levels of the neutral argon atoms (to be discussed further in section II. 5. 5), then relaxing to a state of partial LTE by $t \simeq 40$ μsec, and finally back to full LTE for $t \gtrsim 45$ μsec.

II. 5. 2 Electron Temperature vs. Time at $x/L = 0.90$

The shock velocity profiles in figures 4 and 6 show that the shock behavior is dominated by the multiple shock diffraction processes originating at the cone entrance. In a similar manner the temperature vs. time profile in figures 36 and 37, and the electron number density profile in figure 34 show that the thermodynamic conditions near the cone vertex are dominated by similar effects.

As the incident shock wave propagates towards the cone vertex, it produces localized regions of gas distinguished by considerably higher temperatures and electron number concentrations than the surrounding fluid. These regions originate as point discontinuities at the locations where the center shock collapses and the stemshock intersects the cone axis; subsequently, the regions propagate towards the vertex with the local fluid velocity. Effects of diffusion and convection gradually produce the localized regions of hot gas mentioned above.

The centerline Mach number at the stemshock intersection points are found from figure 3. Using the equilibrium calculations described in appendix A, the corresponding values of the equilibrium velocity of the shock-heated fluid, u_2 , can be found. Assuming that the gas originally at the intersection point propagates up the cone with constant velocity along stream lines, gives one estimate of the arrival time of this gas at $x/L = 0.90$. Another estimate can be found by assuming the gas behind the incident shock wave to behave according to the similarity solution for an imploding shock wave. An account of this is given in reference 2.

Combining these estimates gives a probable upper and lower bound on the times when the gas regions, originally located at the stemshock intersection points on the cone axis, pass the window. These times are indicated in figure 36. Δt_1 is the time associated with the gas originally at $x/L = 0.89$, and is seen to be within the relaxation time expected at these conditions. Δt_2 and Δt_3 are the times associated with the gas originally at $x/L = 0.825$ and $x/L = 0.64$ respectively. The gas originally at the first stemshock intersection point, $x/L = 0.30$, does not reach the window prior to the arrival of the reflected shock wave. The appearance of peaks in the temperature profile coinciding closely with the time intervals Δt_2 and Δt_3 lends credibility to the concept of localized regions of gas with thermodynamic conditions exceeding that of the surrounding fluid.

Immediately following the stemshock intersection point at $x/L = 0.825$ there is a region where the centerline shock velocity experiences a rapid deceleration, and consequently there is a rapid decrease in the temperature of the shock-heated gas. For a stationary observer sitting at $x/L = 0.90$ this is seen as an increase of gas temperature in time, approaching a maximum when the gas originally at $x/L = 0.825$ passes the window; these features are indeed seen between $t \doteq 2.5$ and $t = 5$ μsec in figure 36. The gradual increase in centerline Mach number from approximately 17 at $x/L = 0.7$ to 18 at $x/L = 0.825$, and the sudden jump to a value of 24.9 at the intersection point would be seen as a continuing decrease in temperature by our stationary observer. This is presumably the reason for the decrease in temperature between $t = 5$ and $t = 15\ \mu sec$. From figure 3, the variation of Mach number in the region prior to and after the stemshock intersection point at $x/L = 0.64$ should produce another cycle of, first, increase and then decrease in temperature as a function of time at the window position. The second peak in the temperature profile of figure 36 between $t = 15$ and $t = 20\ \mu sec$ is probably this region.

Superimposed upon these detailed features is seen to be a gradual heating of the fluid, presumably caused by the compressive effect of the convergent geometry. This can be seen by comparing the equilibrium temperatures of the gas produced at the stemshock intersection points with the measured values at the time when this gas should pass the window. At $x/L = 0.825$ the centerline Mach number was 24.9 giving an equilibrium temperature of $14900^{o}K$. The corresponding values at $x/L = 0.64$ are 19 and $13000^{o}K$. The temperatures from figure 36 are 19230 and $19980^{o}K$, respectively. In view of the fact that the measured temperature is averaged across the cone, it can be concluded that these results clearly show the effect of compressive heating. The gradual rise of temperature from $t = 22.5\ \mu sec$ until the arrival of the reflected shock is most likely associated with compressive effects on the gas originally in the region between $x/L = 0.40$ and $x/L = 0.55$. Gas heated by the incident shock wave prior to this would not reach the window before the reflected shock.

The reflected shock wave leaves the gas in a highly excited state. The appropriate relaxation time is now dictated by the time needed to reach equilibrium among electrons, singly and doubly ionized argon atoms. Using expressions from reference 11, one concludes that this relaxation time is of the order of 10^{-7} seconds or less.

From the relative line intensity method, the electron temperature varied from -10^{6} °K to 10^{5} °K during the first 8 μsec after the reflected shock wave. Since the temperatures were in principle determined by least squares fitting a straight line to measured relative intensities (see section II. 4. 4b), the negative temperature has two possible explanations: 1) the assumption of Boltzmann statistics used in relating line intensities to temperature is invalid (i. e., the plasma is in a nonequilibrium state), or 2) large amounts of scatter and/or uncertainties exist in the measured intensities. These possibilities are discussed in section II. 5. 5.

Following this 8 μsec interval the temperature is seen to drop dramatically. This behavior is best seen in figure 37, which shows temperature vs. time on a semilog plot. The temperature appears to fall exponentially with a time constant of 14. 8 μsec. At $t = 55$ μsec there is a sudden jump in temperature (this will be discussed in the next section), apparently followed by a second exponential drop in temperature. On the same figure is shown the relative electron number densities from the continuum intensity measurements, indicating a similar behavior. Some recent measurements with a piezoelectric pressure probe mounted in the wall of the cone at $x/L = 0.90$ have produced pressure vs. time curves, also of a similar nature.[29] Following the reflected shock, the pressure appears to decay with three distinct time constants of 21.6, 14.5 and 33.0 μsec over time intervals coinciding closely with the ones identifiable on figure 37.

From figure 37 we find a cooling rate of 2 x 10^9 °K/sec from t = 40 to t = 55 μsec, and 6 x 10^8 °K/sec from t = 55 to t = 80 μsec. Cooling rates of this order should be rapid enough to offer a possible application in producing prolonged population inversion between vibrational energy levels in molecular gases.

II. 5. 3 Electron Number Density as a Function of Time at $x/L = 0.90$

The comments made in section II. 5. 2 concerning the effects of diffraction and convergent geometry are directly applicable to the electron number density profiles of figures 34 and 37. However, since the electron number density varies as the $\frac{1}{4}$ power of temperature the dramatic peaks seen in figure 36 are not evident. A change of slope in the curve seems to have taken their place e. g. , the change of slope at t = 55 μsec and the plateaus at t = 10 and 20 μsec. Compressive effects are clearly seen. Using the absolute scaling from section II. 4. 4c, the electron number density of the gas passing the window at t = 25 μsec is found to be 7.1×10^{17} cm^{-3}, whereas the equilibrium value of N_e at the time this gas was shocked was of the order of 8×10^{16} cm^{-3}.

In the reduction of continuum intensities to N_e discussed in section II. 4. 4, the Biberman factor ξ $(\nu_1\ T_e)$ was assumed independent of T_e. Following Schlüter[14], however, there is a slight temperature dependence for ξ in the case of argon. Specifically, $\xi(\lambda_1, T_1)/\xi(\lambda_1, T_2) > \xi(\lambda_2, T_1)/\xi(\lambda_2, T_2)$ for $T_1 > T_2$ (λ_1 = 4130 Å, λ_2 = 7000 Å), with the difference increasing with increasing temperature. This is most likely the explanation for the growing discrepancy between N_e as found from I_c (7000 Å) and I_c (4130 Å) shortly after the reflected shock.

The recent pressure measurements (mentioned in section II. 5. 2) produced a pressure vs. time history that agreed well both quantitatively and qualitatively with the values of T_e and N_e shown in figures 34, 36 and 37.

II. 5. 4 Conditions Shortly After the Reflected Shock

As indicated in figure 36, direct computation of electron temperature based on relative line intensities for short times following the reflected shock wave yields temperatures ranging from -10^6 to 10^5 °K. The obvious question is whether this is due to experimental scatter, or to a possible population inversion in the upper excited levels of the neutral argon atoms.

The line intensities were found by subtracting the measurements of continuum alone from the measurements of line and underlying continuum. Shortly after the reflected shock, the normalized intensities were both large numbers, differing only slightly. Typical numbers are 15.36 for the 6865.4 Å line and continuum, and 12.95 for the continuum alone. This indicates a greater possible experimental error than for the remainder of the data, where a typical set of values is 3.354 and 1.026 for the same line. On the basis of the reproducibility of the measured values, however, it is felt that experimental scatter alone is not sufficient to change the above mentioned temperatures to reasonable values.

Population inversion is said to exist if

$$\frac{N_i/g_i}{N_j/g_j} > 1^{\dagger} \qquad (i > j) \quad . \tag{56}$$

If partial LTE exists above the level j ,

$$\frac{N_i/g_i}{N_j/g_j} = \exp\left(- \frac{E_i - E_j}{k\,T_e} \right) \quad .$$

---

† In this expression it has been assumed that the line shape profiles φ_{nm}, η_{nm} and η_{mn} are equal, see section II. 2. 2.

Since self-absorption in the neutral argon lines is negligible at the high temperatures existing shortly after the reflected shock wave, equation (56) can be rewritten in the form

$$\mu_{ij} \equiv \frac{N_i/g_i}{N_j/g_j} = \frac{I^i_{\ell m}}{I^j_{\ell m}} \frac{\left(\frac{1}{4}\pi\ h\nu_{nm}\ A_{nm}\ g_n\right)_j}{\left(\frac{1}{4}\pi\ h\nu_{nm}\ A_{nm}\ g_n\right)_i} \psi_{ij} \frac{g(w/b_c,\ z)_j}{g(w/b_c,\ z)_i} . \qquad (57)$$

Here ψ_{ij} accounts for the effect of neighboring lines as discussed in section II. 2. 3. In writing this equation, use has been made of the fact that even in a nonequilibrium situation, the amount of energy emitted in a spectral line is directly proportional to the number density of the upper level. Using the measured line intensities of the 6965. 4 Å, and the 6871. 3 and 6752. 8 Å lines, the values of μ_{ij} for the upper levels of each line were evaluated at several time intervals shortly following the reflected shock wave. The result is given in the table below, which indicates that there is indeed a possibility for population inversion shortly after the reflected shock wave. To see whether a population inversion is realistic we follow Hurle and Hertzberg[25], they investigated rapid expansions as a means of producing population inversion between two electronic energy states. The two states must be optically connected, and the upper state must have a radiative lifetime that is considerably longer[†] than the lifetime of the lower state. Hurle and Hertzberg concluded that in the case of two electronic states in xenon having radiative lifetimes of 10^{-6} and 10^{-9}, respectively, a cooling rate of 10^9 °K/sec would be

---

[†] Preferably several orders of magnitude.

sufficient to preserve the initial population in the upper state while the lower state decays by emission. Experimental efforts to verify the inversion, however, were unsuccessful.

In the present case, while the condition on radiative lifetimes is only marginally satiesfied[†], the cooling rate is of the order of 2 x 10^9 °K/sec during the exponential fall at $t > 40$ μsec, and presumably even greater in the immediate region behind the reflected shock. A linear extrapolation of the temperature vs. time curve showni in figure 37 gives a cooling rate of 4.5 x 10^9 °K/sec during the first 10 μsec after the reflected shock.

The population inversion thus comes about as a result of radiative depopulation of the lower energy levels, while collisional excitations keep the upper states in equilibrium with the electrons. As the temperature falls the increasing effect of self-absorption reduces the effective depopulation rate of the lower levels, and in particular the first excited level. The transition from a nonequilibrium state to a state of partial LTE above the first excited level for $t \geqslant 40$ μsec is most likely a result of this.

[†] See the table on page 108

TABLE I

Population index μ as a function of time.

t (μsec)	30	33.75	35	37.5	40
$\mu_{\lambda_1,\lambda_2}$	1.8	1.7	1.4	1.1	0.70
$\mu_{\lambda_1,\lambda_3}$	2.1	1.4	1.6	0.90	0.68

Optical Connections and Lifetimes

λ_1 = 6965.4 Å, E_n = 107496 cm^{-1} ; λ_2 = 6871.3 Å, E_n = 118651 cm^{-1}

Optical connection is the 8962.2 Å line, with

E_{upper} = 118651 cm^{-1}, E_{lower} 107496 cm^{-1}

Life time of 107496 level is ~ 5 x 10^{-8} sec

Life time of 118651 level is ~ 2 x 10^{-7} sec

λ_1 = 6965.4 Å, E_n = 107496 cm^{-1} ; λ_3 = 6752.8 Å, E_n = 118907 cm^{-1}

Optical connection is the 8605.8 Å line, with

E_{upper} = 118907 cm^{-1}, E_{lower} 107496 cm^{-1}

Life time of 107496 level is ~ 5 x 10^{-8} sec

Life time of 118907 level is ~ 2 x 10^{-7} sec

II. 5. 5 The Second Reflected Wave

In the measurements of reflected shock velocities in the 10° half-angle cone mentioned in part I, Setchell noticed the appearance of a second reflected shock wave. Figure 12 shows this in the x - t diagram reconstructed from the velocity measurements. The second reflected shock was only detected in $M_o = 6$ case. Recent pressure measurements (mentioned in section II. 5. 2), also failed to detect a second reflected shock at $x/L = 0.90$ in the $M_o = 10.2$ case. However, they did show a definite change of slope in the pressure vs. time profile at $t = 55$ μsec, analogous to the behavior of both the electron number density and electron temperature profiles as shown in figures 36 and 37. The absence of a pressure increase (at $t = 55$ μsec), coupled with the definite jump in temperature may be indicative of a contact surface, rather than a shock wave, passing the window at this time.

In his thesis, Setchell[2] speculated that the second reflected shock in the $M_o = 6$ case was a result of interactions between sharp gradients in the degree of ionization, and the first reflected shock wave near the vertex. Although the region of ionized gas near the vertex is much larger in the $M_o = 10.2$ case[2], interactions between the reflected shock and ionization gradients might still produce waves that propagate to the vertex and reflect.

The behavior of T_e, N_e and p at $t = 55$ μsec, is more likely due to the localized regions of gradients in T_e and N_e produced at the previous stemshock intersection points (discussed in section II. 5. 2). The peak in T_e at $t = 15$ μsec is associated with the passing of the localized gradient produced at the stem-shock intersection point at $x/L = 0.64$. This hot "slug" of gas then moves towards the vertex, interacts with the reflected shock, and subsequently propagates upstream. The only slightly longer time delay (40 μsec) between the "second reflected wave" and the peak in T_e at 15 μsec, and the time interval (30 μsec) between the incident and reflected shock suggests that the "second reflected wave" is indeed a result of the stemshock intersection point at $x/L = 0.64$. Further experimentation is needed before any conclusive decision can be reached. It is quite clear, however, that the "second reflected wave" is yet another examples of the fact that the entire flow situation in the cone is dominated by the shock diffraction effects initiated at the cone entrance.

II. 6 CONCLUDING REMARKS

The successful use of emission spectroscopy as a diagnostic tool towards a better understanding of the shock dynamics in a convergent channel has been demonstrated. Relative line intensities of several neutral argon lines were monitored to determine electron temperatures as a function of time. The Stark broadened profile of the 6965.4 Å neutral argon line was used to determine electron number densities. Continuum intensity measurements provided an added check on these quantities. A condition of full LTE behind the incident shock was indicated at most times.

Previous theoretical and experimental work had provided a comprehensive description of the motion of the incident shock wave. The theoretical prediction by the author, of a cyclic shock diffraction pattern initiated at the convergence entrance was verified experimentally. Estimates of thermodynamic conditions close to the vertex based on centerline Mach numbers indicated that one might expect electron number densities and temperatures well in excess of standard shock tube performance. Measurements of reflected shock velocities close to the vertex indicated the importance of previous nonuniformities produced by the incident shock wave. Since the expected rapid expansion behind the reflected shock wave could not be measured, estimates of cooling rates were uncertain.

The present investigation confirmed the expectation of a highly compressed, high temperature plasma near the vertex of the 10° half-angle cone. Electron temperatures measured as a function of time showed a temperature profile dominated by the incident shock diffraction processes. Compressive heating caused by the convergent geometry was a superimposed effect. In the region immediately following the reflected shock wave temperatures found by relative line intensities were meaningless. Comparing intensities of two selected lines, a possibility of population inversion was indicated. An exponential decrease in temperature, confirmed by a similar drop in electron number densities, indicated cooling rates in excess of 2×10^9 K^o/sec at later times. A "second reflected wave" was observed, and a qualitative explanation was discussed.. Electron number density measurements confirmed the results discussed above.

A comprehensive study of self-absorption effects for Stark broadened spectral lines was undertaken, and a simple method for separating individual correction effects was demonstrated.

The nonuniformities (both in temperature and electron number densities) caused by the conical convergence limits its applicability in conventional high temperature plasma research. The rapid cooling associated with the reflected shock wave offers a definite possibility for the study of nonequilibrium plasmas. A final conclusion and recommendation that can be drawn from the present investigation is the need for a multichannel optical system, capable of wave length separations of less than one Ångstrom, if further spectroscopic investigation is considered. A one channel system is sufficient but comparatively time consuming.

APPENDIX A

Equilibrium Conditions in a Multiply Ionized Argon Plasma Produced by a Strong Shock Wave

Equilibrium conditions behind a strong shock wave in xenon have been computed by Zhurin and the author[26]. Following a similar approach[†], we calculate equilibrium parameters of a multiply (singly, doubly and triply) ionized argon plasma. We present first the assumptions, and necessary approximations. This is followed by a presentation and discussion of the governing equations, and a few points on the computational procedure.

Assumptions and Approximations

1. Thermodynamic equilibrium will exist in the gas; i.e., the temperatures of the free electrons, atoms, ions and bound electrons in an excited state are all equal, from which it follows that,

2. The distribution of particles behind the shock wave is taken to be described accurately by the Boltzmann distribution function.

3. The thickness of the viscous shock and non-equilibrium zone is less than the shock-heated gas region.

4. In the energy balance calculations radiation is necessarily neglected, because the inclusion of radiation would require not

---

[†] With two main differences, in the present investigation the effect of reduction in ionization energy is included and the computations are carried out continuously as a function of equilibrium temperature.

only knowledge of the functions that accurately characterize the radiation, but also exact knowledge of the size of the shock-heated gas region.

5. The tendency of Coulomb interactions to lower the ionization potential has been included. The formulation derived by Ecker and Weizel[27] was used to relate the lowering of the ionization potential to the plasma parameters.

6. The inconsistency in the mathematical singularity of the diverging series representation of the electronic partion function Z(T) is avoided by truncating the series at values of n where the binding energy of the electron is equal to the reduction of the ionization potential.

Equations

We represent the multiply ionized atom by

$$A_{i-1} \rightleftarrows A_i + e \qquad (i = 1, 2, \ldots) \tag{1}$$

(i = 1 for neutral atoms, i = 1 for singly ionized, . . .) The common law of mass action is given by

$$\frac{N_i N_e}{N_{i-1} N} p = K_i(T) \tag{2}$$

Here N_e, N_i, p, T, K_i stand for electron number density, the number density of the i^{th} specie, pressure, temperature and the equilibrium constant for the i^{th} specie respectively, and

$$N = N_e + \sum_i N_i \quad . \tag{3}$$

From the condition of quasi-neutrality, we have

$$N_e = \sum_i iN_i \quad . \tag{4}$$

Let χ_i represent the degree of the i^{th} step of ionization, then

$$\chi_i = N_i/N_t \quad , \tag{5}$$

where

$$N_t = \sum_i N_i \tag{6}$$

is the total number of atoms and ions. The common form of the Saha equation for a multiply ionized gas is given by

$$\frac{\chi_i \sum_i^{\ell} i\,\chi_i}{\chi_{i-1}(1+\sum_i i\chi_i)}\, p = K_i(T) \quad , \tag{7}$$

where $\chi_o = 1 - \sum_i^{\ell} \chi_i$ and ℓ is the highest step of ionization. The equation of state for a multiply ionized gas will take on the form

$$p = \rho(1 + \sum_i i\ \chi_i)\ \frac{R}{\mu}\, T \quad , \tag{8}$$

where ρ, R and μ are the density, universal gas constant and atomic weight. The conservation equations for mass, momentum and energy across a normal shock wave propagating into a gas at rest, are the usual

$$\rho_1 U_s = \rho_2(U_s-u_2) \tag{9}$$

$$p_1 + \rho_1 U_j^2 = p_2 + p_2(U_s-u_s)^2 \tag{10}$$

$$H_1 + \tfrac{1}{2} U_s^2 = H_2 + \tfrac{1}{2}(U_s-u_s)^2 \tag{11}$$

Here U_s is the shock velocity, u_2 is the flow velocity behind the shock and H is the specific enthalpy. Subscript 1 and 2 refer to conditions ahead of and behind the shock respectively.

The system of equations (9)-(11) consists of $\ell + 4$ equations, and has $\ell + 4$ unknowns: T_2, p_2, p_2, u_2, χ_1, $\chi_2 \cdots \chi_\ell$. Making use of standard expressions for the electronic partition functions Z(T), the law of mass action (2) may be written as

$$K_i(T_2) = 2\left(\frac{2\pi m_e}{k^2}\right)^{\frac{3}{2}} \frac{Z_i}{Z_{i-1}} (k T_2)^{5/2} \exp\left(- \frac{\varepsilon_{Ii}-\Delta\varepsilon_{Ii}}{kT_2}\right) \tag{12}$$

where ε_{Ii} and $\Delta\varepsilon_{Ii}$ are the ionization and the reduction of ionization energy, respectively.

The general expressions for the enthalpy as a function of T_2, where the excitation of the electronic levels is included, can now be written as

$$\begin{aligned} H_2(\chi_1, \chi_2, \ldots \chi\ , T_2) &= \frac{5}{2}\Big(1+\sum_i^{\ell} i\chi_i\Big) \frac{R}{\mu} T_2 + \frac{N}{\mu} \sum \chi_i \varepsilon_{Ii} \\ &+ \frac{N}{\mu} \sum_i \chi_i \frac{\sum\limits_j^{j_{max}} g_{ji}\varepsilon_{ji} \exp(-\varepsilon_{ji}/kT_2)}{\sum\limits_i^{j_{max}} g_{ji} \exp(-\varepsilon_{ji}/kT_2)} \end{aligned} \tag{13}$$

where N is the Loschmidt number, and j_{max} is defined as discussed in point 6. In this expression the first term gives the energy of the translational degrees of freedom, the second term denotes the energy of the multiply ionized states, and the third term expresses the energy which goes into the excited states of the neutral and multiply ionized atoms.

Computation

Let $\ell = 3$, i.e., the highest stage of ionization considered will be triply ionized particles. If we also denote χ_1, χ_2, and χ_3 by α, β and γ respectively, the three Saha equations will take on the form

$$\frac{\alpha(\alpha+2\beta+3\gamma)}{(1-\alpha-\beta-\gamma)(1+\alpha+2\beta+3\gamma)}\, p_2 = K_1(T_2) \tag{14}$$

$$\frac{\beta(\alpha+2\beta+3\gamma)}{\alpha(1+\alpha+2\beta+3\gamma)}\, p_2 = K_2(T_2) \tag{15}$$

$$\frac{\gamma(\alpha+2\beta+3\gamma)}{\beta(1+\alpha+2\beta+3\gamma)}\, p_2 = K_2(T_2) \quad . \tag{16}$$

Combining (14) and (15) we find

$$\alpha = \frac{-r\beta + \sqrt{r^2\beta^2+4r\beta(1-\beta-\gamma)}}{2} \tag{17}$$

or

$$\beta = \frac{(1-\alpha-\gamma) - \sqrt{(1-\alpha\alpha)^2 - 4\,\frac{\alpha^2}{r}}}{2} \quad , \tag{18}$$

where

$$r = K_1(T_2)/K_2(T_2)$$

Equations (15) and (16) yield

$$\gamma = \frac{\beta^2}{\alpha} \frac{K_3(T_2)}{K_2(T_2)} \quad . \tag{19}$$

Combining (9), (10), and (11) results in the familiar Hugoniot relation

$$\left[H_2(\alpha,\beta,\gamma,T_2) - H_1(T_1)\right] = \frac{1}{2}\left[p_2(\alpha,\beta,\gamma,T_2)-p_1\right]\left[\frac{1}{\rho_1} + \frac{1}{\rho_2}(\alpha,\beta,\gamma,T_2)\right] \tag{20}$$

Where $H_2(\alpha,\beta,\gamma,T_2)$ is found from (13) using $\ell = 3$. With the use of the equation of state, now in the form

$$p_2 = \rho_2(1+\alpha+2\beta+3\gamma)\frac{R}{\mu} T_2 \quad , \tag{21}$$

and equations (14) (19), the Hugoniot relation can be expressed as an equation for either α, β or γ with the equilibrium temperature T_2 as a parameter[†]. Once α (or β or γ) is found, appropriate use of equations (17) - (19) and (14) - (16) will yield p_2. Equation (21) can then be solved for ρ_2, which together with p_2 and (9) and (10), will determine u_2 and U_s. From p_2, T_2, ρ_2 and α, β and γ, any other equilibrium quantities can be computed.

The process described above was carried out for a test gas of argon at 293°K and a series of initial pressures from 0.1 to 100 torr. At the same time, a series of cross correlations

---

[†] Assuming, of course, that the conditions ahead of the shock, p_1, ρ_1 and T_1 are known.

were carried out, to produce tables of N_e, N_o, N_1, N_2 and N_3 as a function of pressure and temperature. Starting with $T_2 = 5000^\circ K$ (increasing in steps of $100^\circ K$), the equations were solved for α. Since equations (18) and (19) (which were iterated to find β and γ from α) depend upon the reduction of ionization energy (which depends upon T_2 and N_e), the solution is a doubly iterative process. It was found convenient to change to β as the unknown when α reached a maximum. In this case (15) was used to substitute for p_2 in (20) and (21), and (17) and (19) were used to find α and γ as a function of β. The computations were stopped before it became necessary to switch to γ as the main unknown.

The computations were carried out on the Caltech IBM 360/75 system, with heavy use of the CalComp plotter. Values for g_{ni}, ε_{ni} and ε_{Ii} were taken from the compilation by Moore.[28]

A sample of the calculations are shown in figures 38-39.

APPENDIX B

Additional Correction Scheme for Self-absorption and Finite w/b_c

The optically thin temperature from section II. 4. 5b, and electron number densities from Stark broadening and continuum intensities (not corrected for self-absorption) determine a first estimate of the complete thermodynamic conditions. In principle, a series of curves similar to figure 20 could then be prepared, one for each possible relative line intensity combination, and an iterative process of self-absorption corrections carried out. This formidable project was not undertaken. The simplified process used instead can be described as an idealized two-line intensity correction and is outlined below.

1. Determine the pressure using the optically thin temperature (from II. 4. 5b), N_e (from II. 4. 4) and the equilibrium calculations from appendix A.
2. With the "corrected" (used here in the same sense as in point 1. in section II. 4. 5c) measured intensity ratio of the 6965. 4 and 4200. 7 Å lines, and the pressure from 1. or 4., use figure 20 to find an improved value of T_e .
3. Use this T_e and equations from section II. 2 to find self-absorption corrections to N_e (Stark) and N_e (continuum).
4. Use these values of N_e and T_e to find a new improved value of the pressure p .
5. Repeat steps 2., 3. and 4. until the values of T_e, N_e and p converge.

This iteration process also converged adequately after 3 - 4 cycles.

REFERENCES FOR PART II

1. Storm, E., Paper presented at AIAA 20th Annual Region VI Student Conference, San Luis Obispo, California (May, 1970).
2. Setchell, R. E., Ph. D. Thesis, California Institute of Technology (1971).
3. Petscheck, H., and Byron, S. R., Ann. Phys., **1**, 270 (1957).
4. Wong, H., and Bershader, D., J. Fluid Mech., **26**, 459 (1966).
5. Chapin, C. E., Purdue University Report, AA & ES 67-9.
6. Biberman, L. M., and Yakubov, I. T., Sov. Phys. Tech. Phys., **8**, 1002 (1964).
7. Griem, H. R., *Plasma Spectroscopy*, McGraw-Hill, New York (1964).
8. Unsöld, A., *Physik Der Sternatmosphären*, Springer Verlag, Berlin (1955).
9. Lochte-Holtgreven, W. (ed.), *Plasma Diagnostics*, North-Holland Publishing Co., Amsterdam (1968).
10. Huddlestone, R. H., and Leonard, S. L. (eds.), *Plasma Diagnostic Techniques*, Academic Press, New York (1965).
11. Zel'dovich, Ya. B., and Raizer, Yu, P., *Physics of Shock Waves and High-Temperature Hydrodynamic Phenomena,* Vols. I & II, English Translation edited by W. O. Hayes and R. F. Probstein, Academic Press, New York (1966).
12. Kolesnikov, V. M., Tr. Fiz. Lust. Akad., Nauk SSSR, **30**, 66 (1964).
13. Biberman, L. M., and Norman, G. E., J. Quant. Spectrosc. Rad. Transfer, **3**, 221 (1963).
14. Schlüter, D., Z. Astrophysik, **61**, 67, (1965).
15. Coates, P. B., and Gaydon, A. G., Proc. Royal Society, **A293** 452 (1966).
16. Wende, B., Z. Physik, **198**, 4 (1967).
17. Ladenburg, R., and Reiche, F., Ann. Physik, **42**, 181 (1913).
18. Levy, A., UTIAS Tech. Note No. 119 (1967).

REFERENCES FOR PART II (cont.)

19. Olsen, H. N., J. Quant. Spectrosc. Rad. Transfer, 3, 59 (1963).

20. "Atomic Transition Probabilities," Vol. II (a critical compilation for the elements sodium through calcium), NSRDC-NBS (1969).

21. Smith, J. A., Ph. D. Thesis, California Institute of Technology (1967).

22. deVos, J. C., Physica, 20, 690 (1954).

23. Rutgers, G. A. W., and deVos, J. C., Physica 20, 715 (1954).

24. Gericke, W. E., Z. Astrophys., 53, 68 (1961).

25. Hurle, I. R., and Hertzberg, A., Phys. Fluids, 8, 1601 (1965).

26. Zhurin, V. V., and Storm, E., GALCIT Internal Report (1968).

27. Ecker, G., and Weizel, W., Ann. Physik, 17, 126 (1956).

28. Moore, C. E., Atomic Energy Levels, National Bureau of Standards, Circular N467 (1949).

29. Setchell R. E., Private Communication.

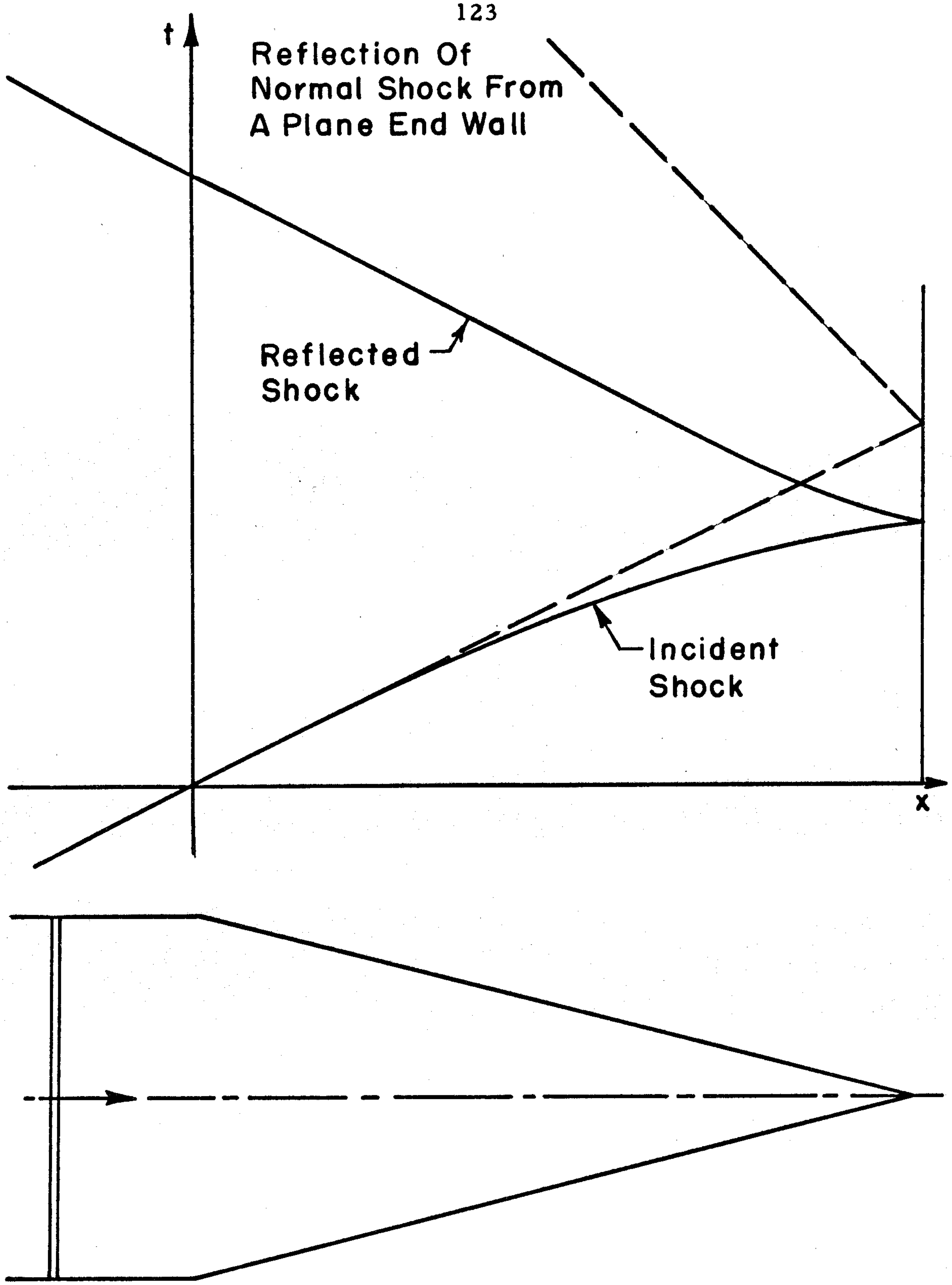

FIG. I INITIALLY PLANE, STRONG SHOCK PROPAGATING INTO A CONICAL CONVERGENCE

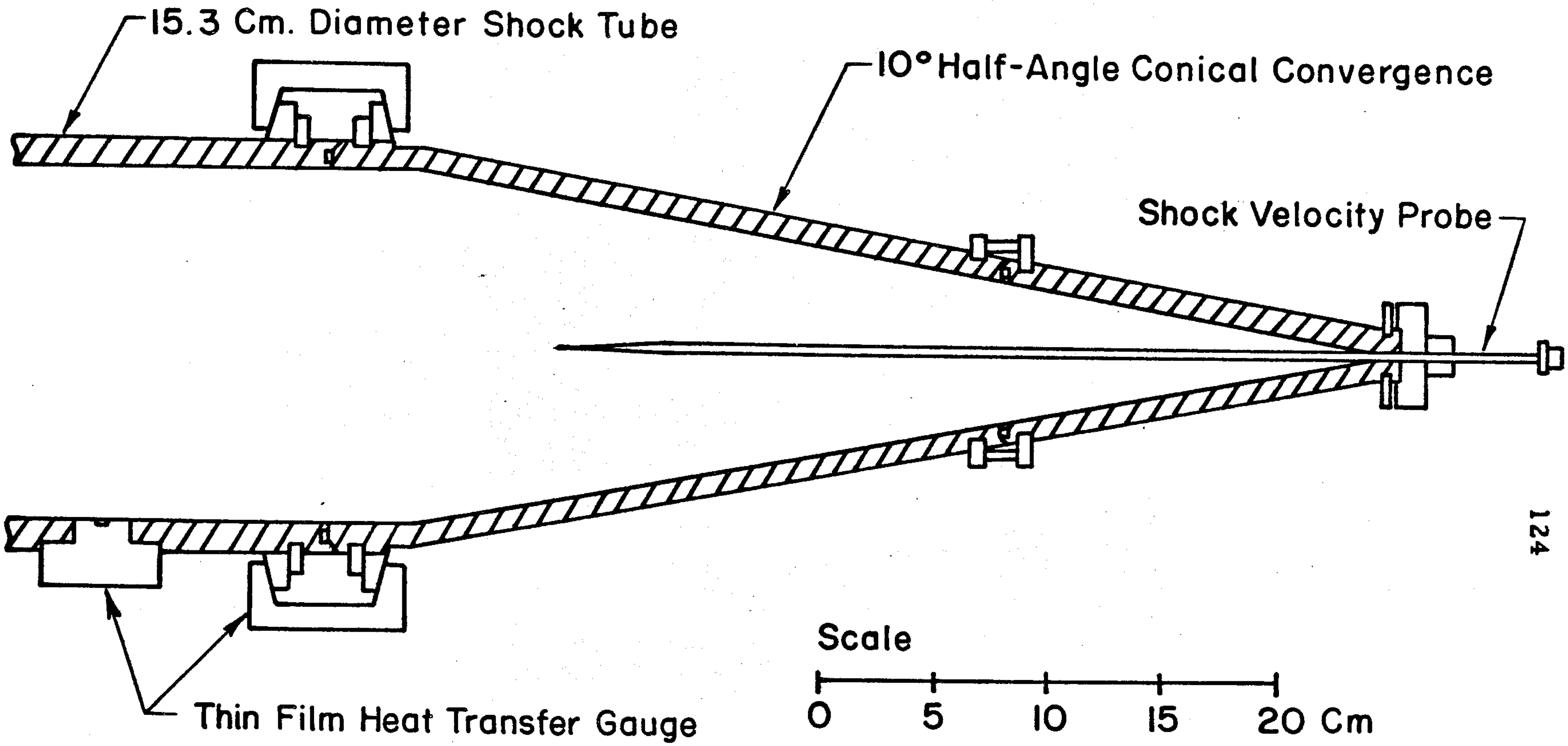

FIG. 2 EXPERIMENTAL APPARATUS

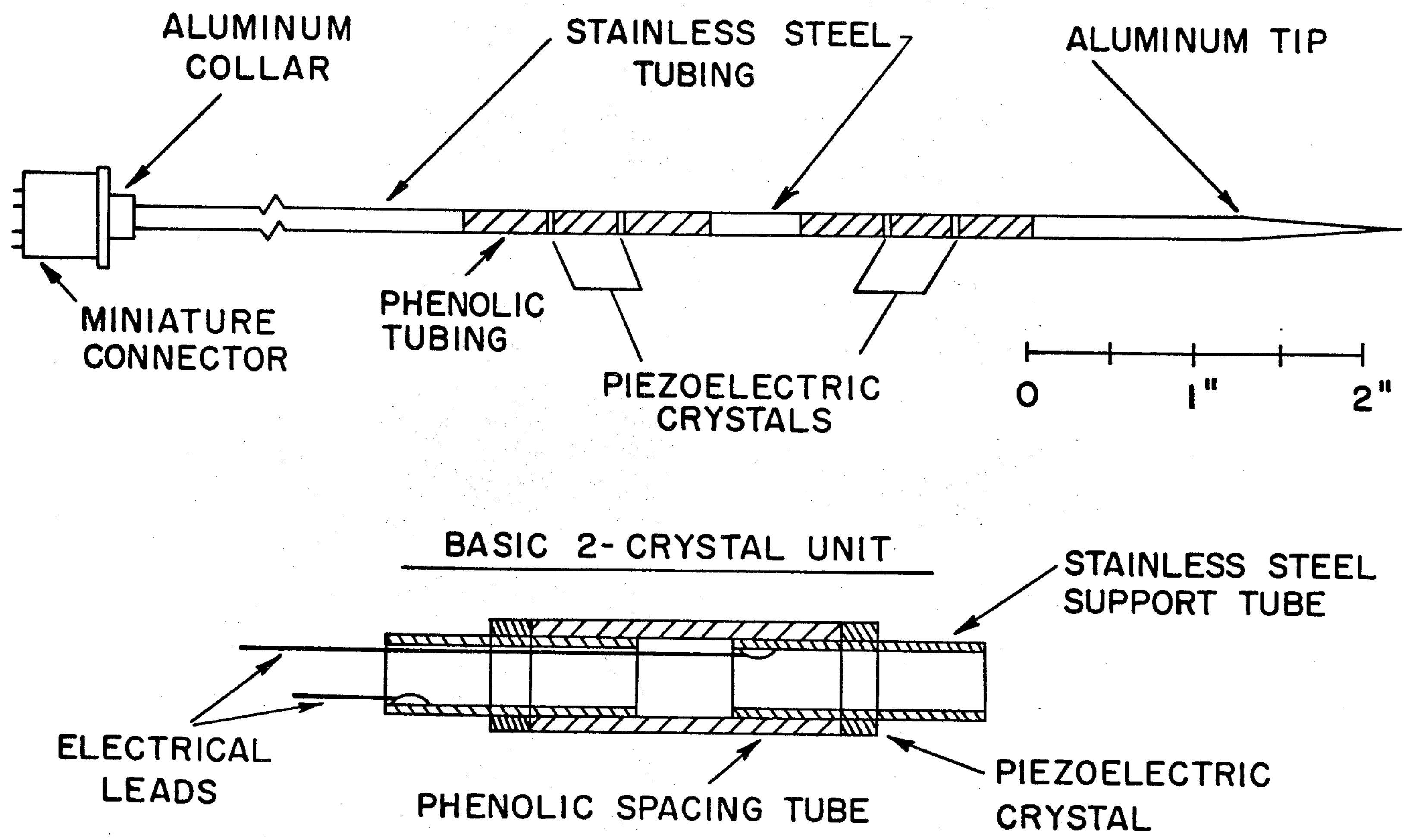

FIG. 3 SHOCK VELOCITY PROBE

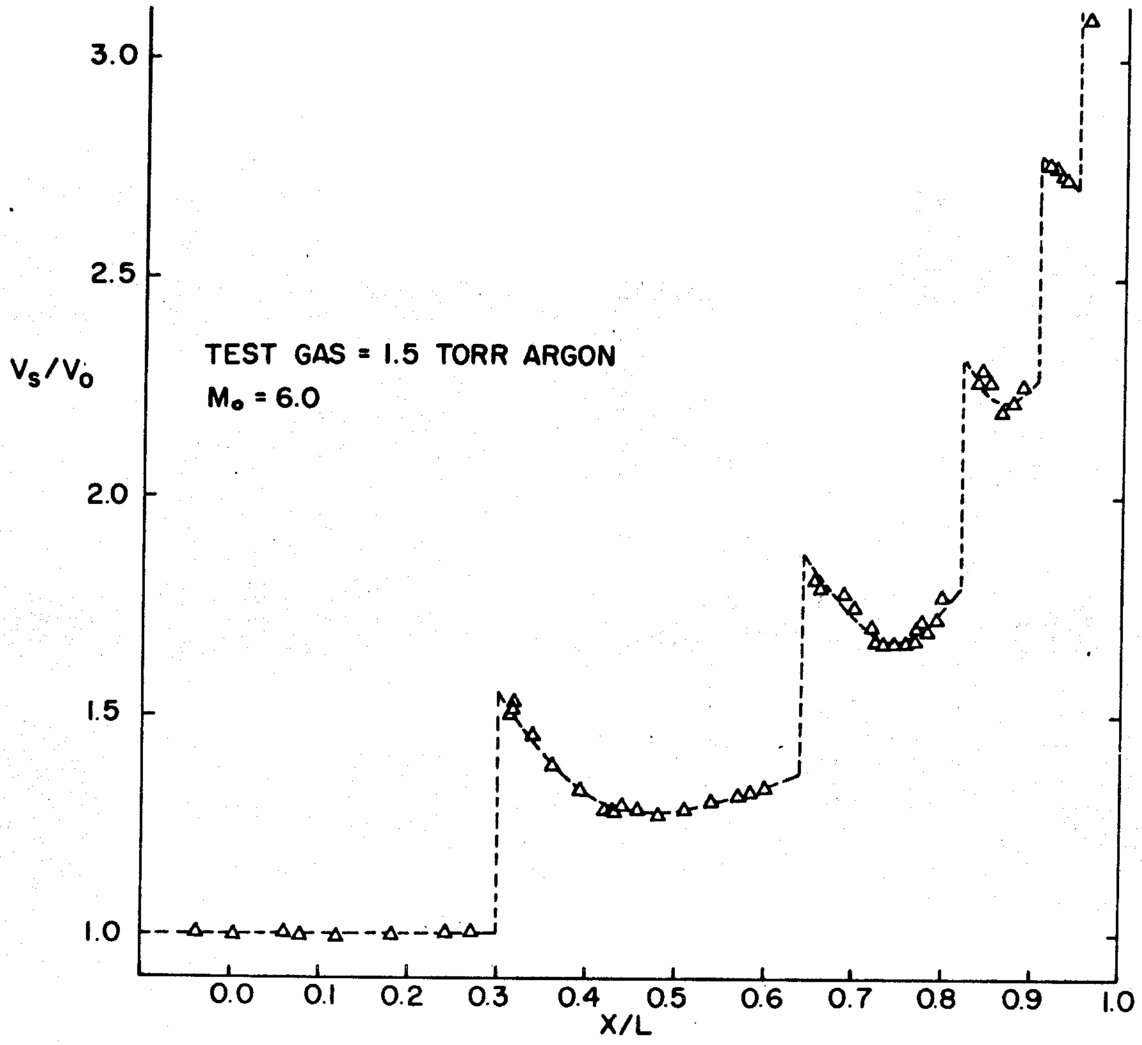

FIG. 4 CENTERLINE SHOCK VELOCITIES IN THE 10° HALF-ANGLE CONE

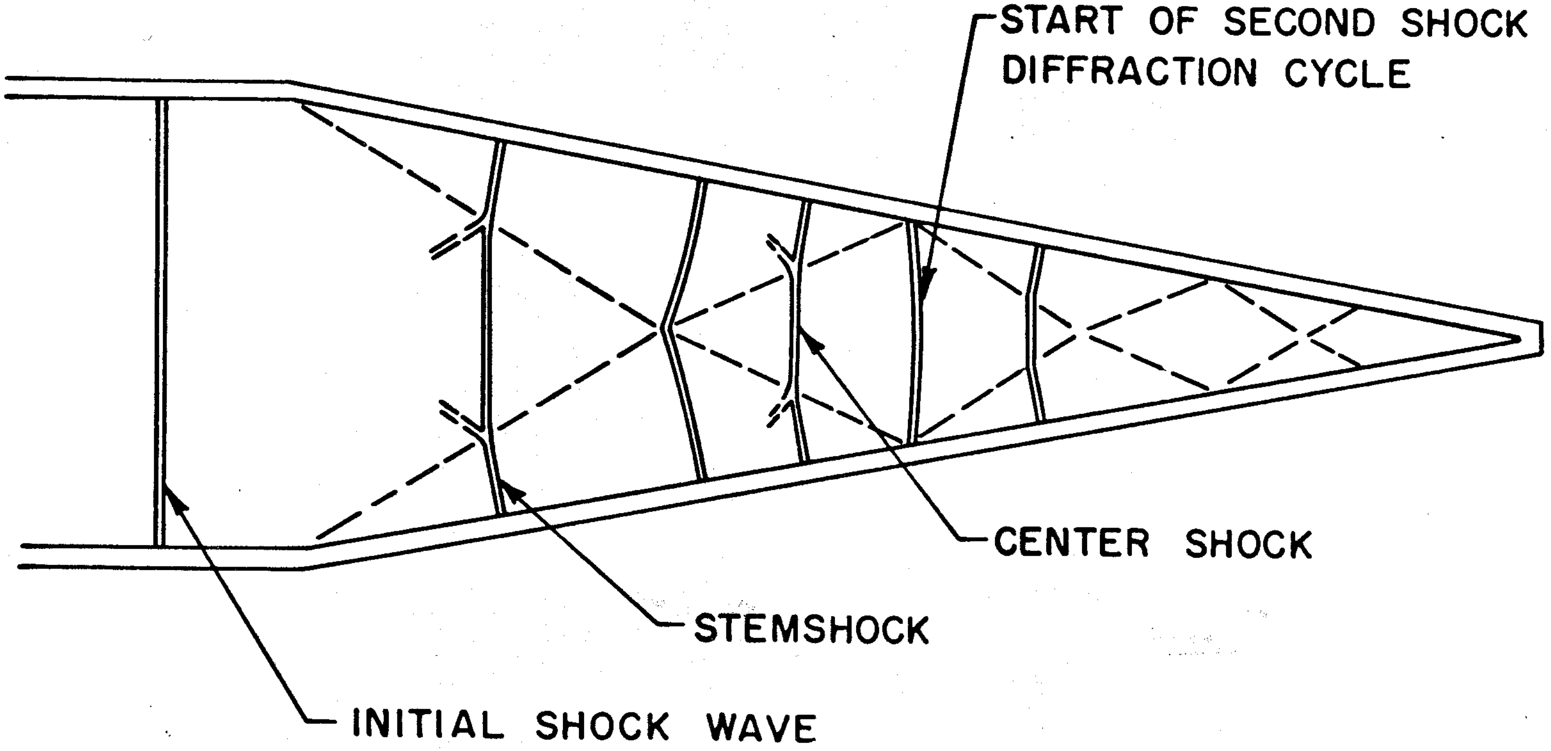

FIG. 5 SHOCK DIFFRACTION PATTERN IN A CONE

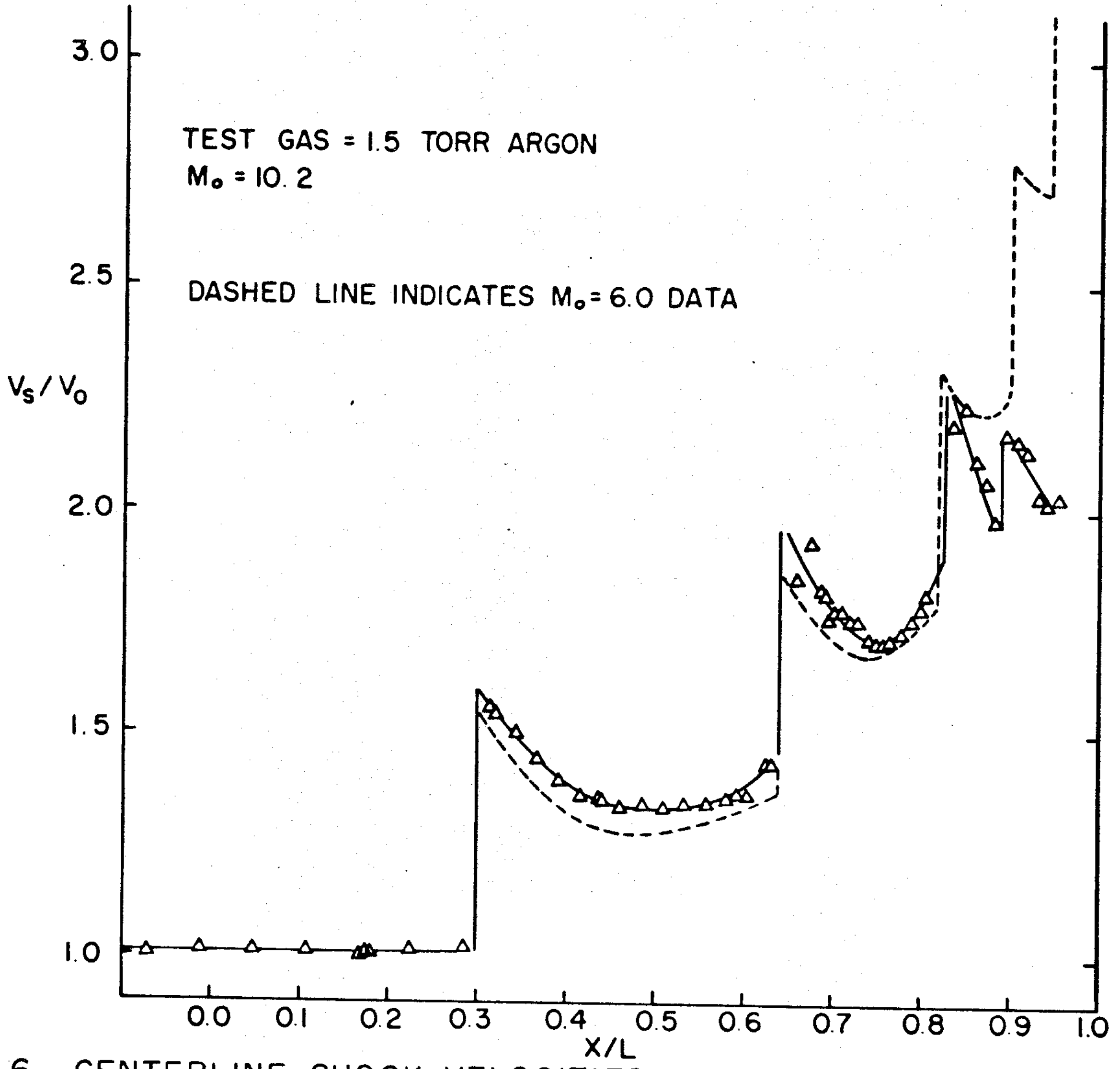

FIG. 6 CENTERLINE SHOCK VELOCITIES IN THE 10° HALF-ANGLE CONE

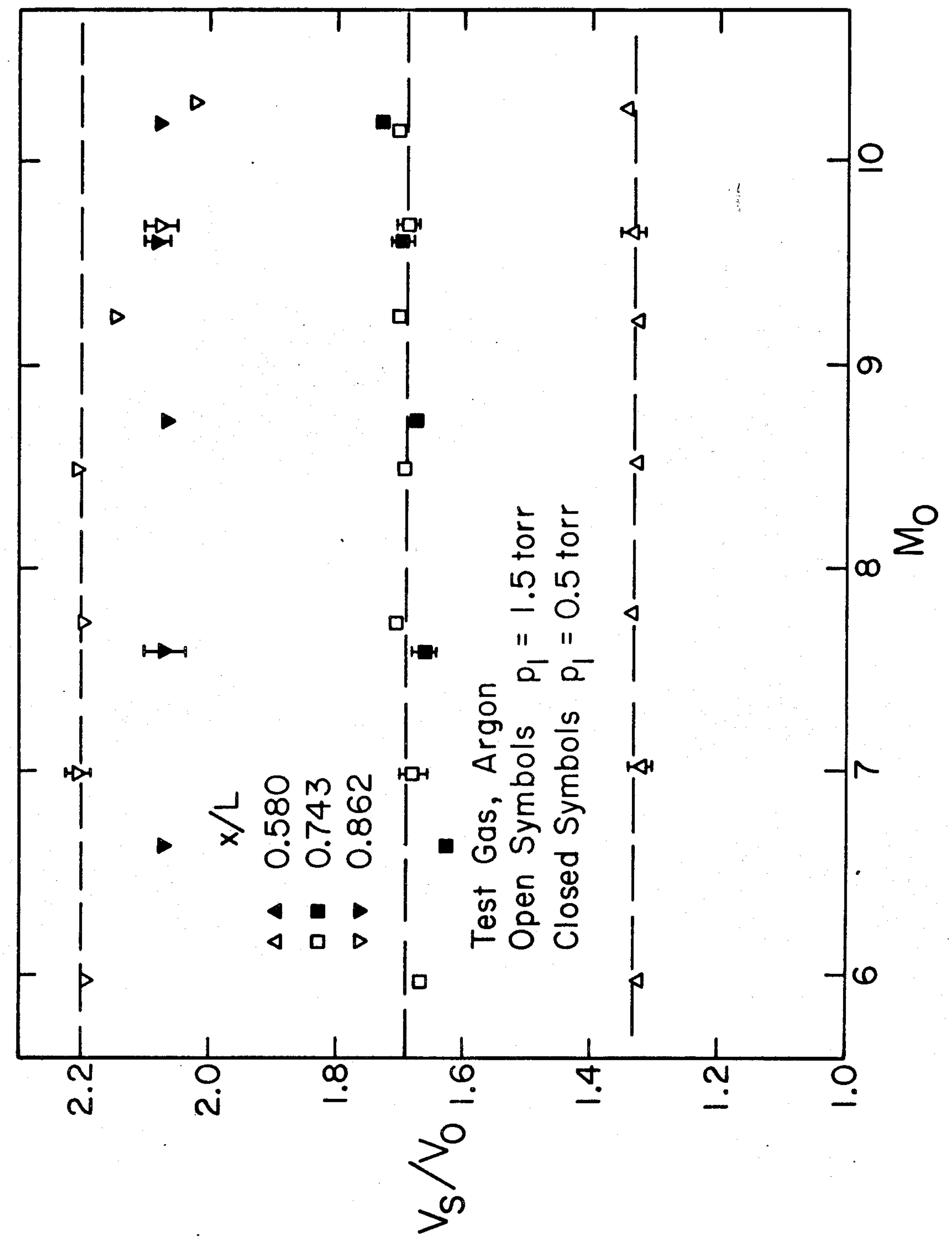

FIG. 7 VARIATION OF INITIAL MACH NUMBER AND PRESSURE

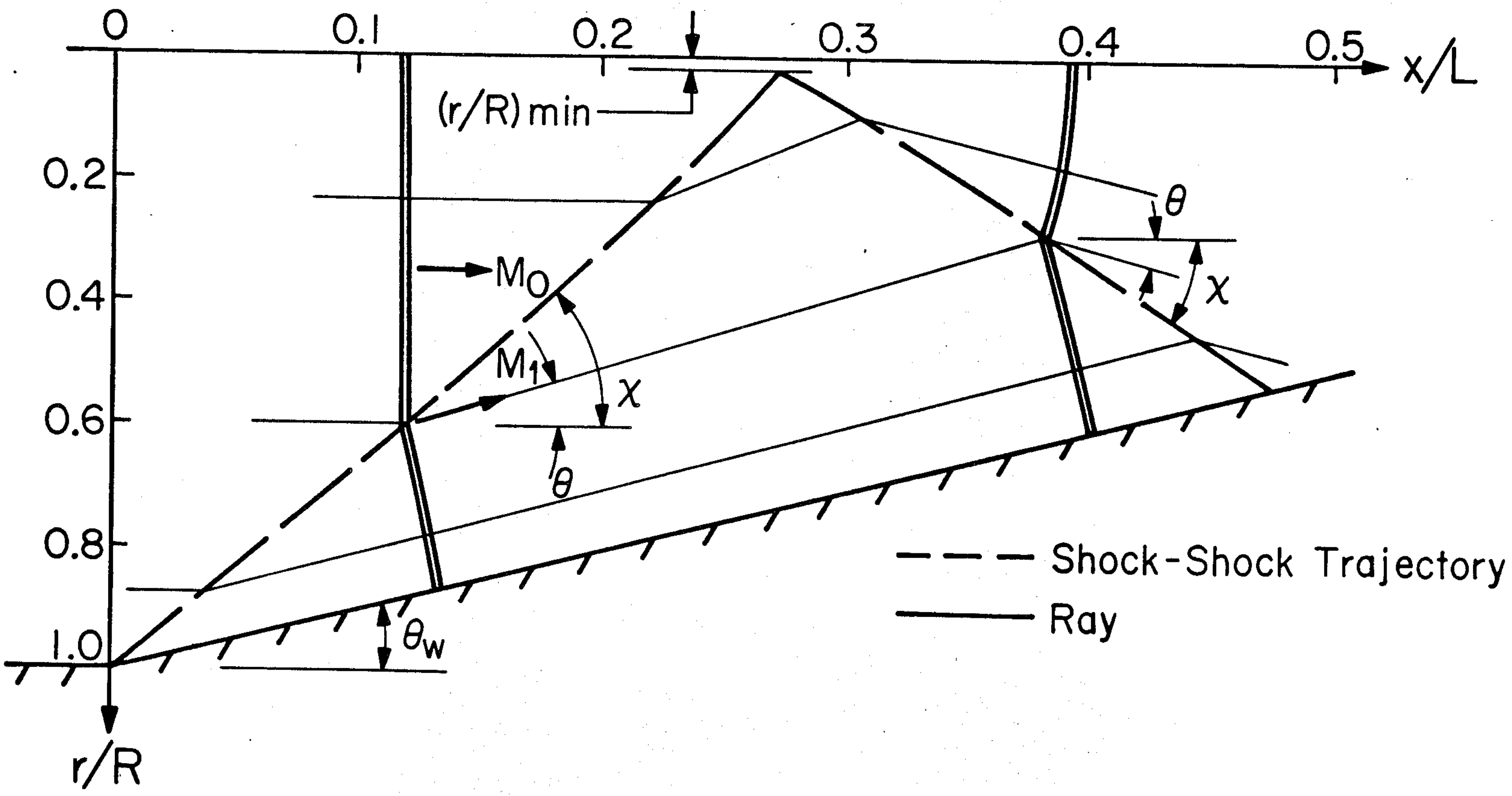

FIG. 8 AXISYMMETRIC DIFFRACTION GEOMETRY

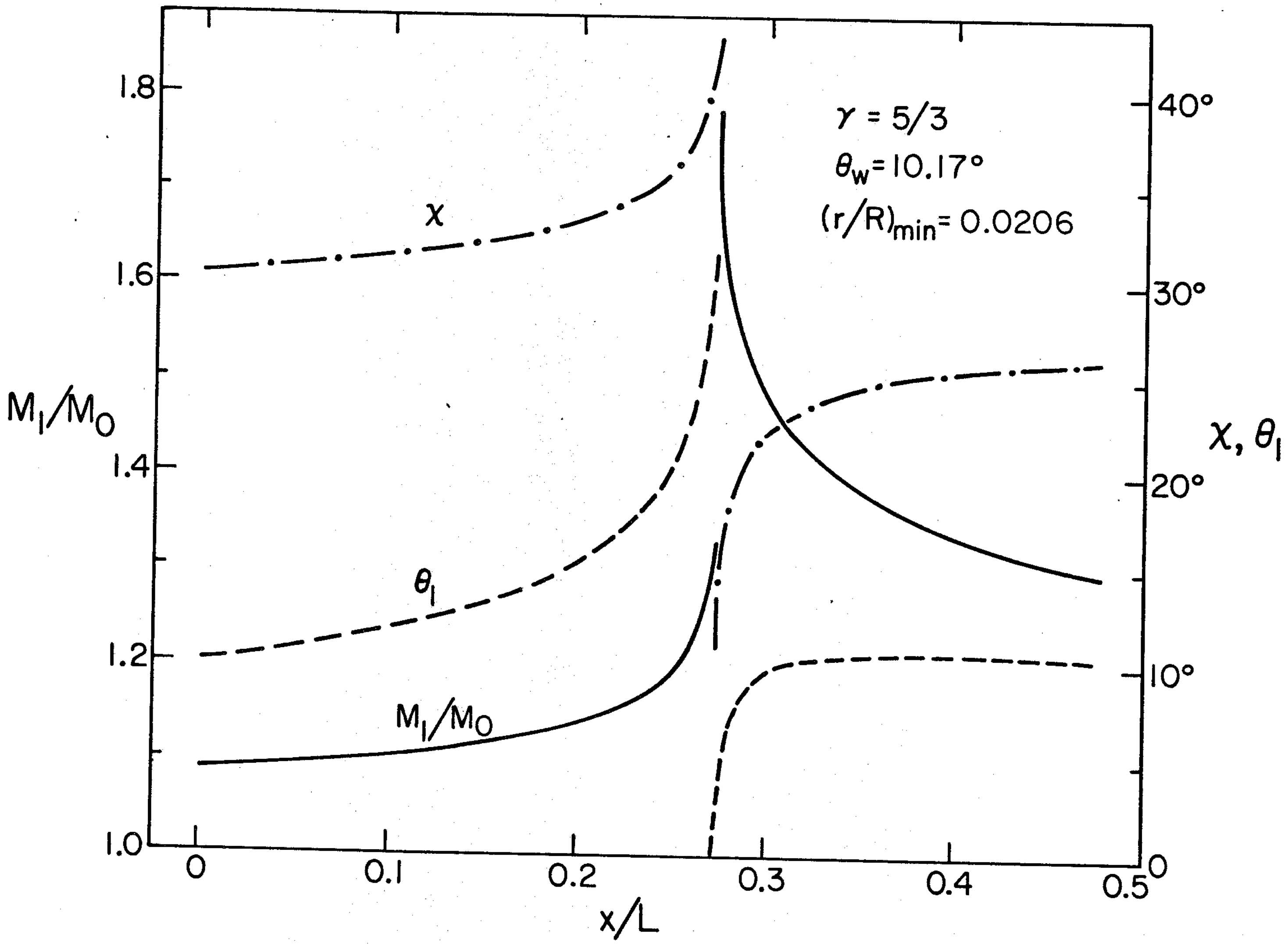

FIG. 9 AXISYMMETRIC DIFFRACTION SOLUTION

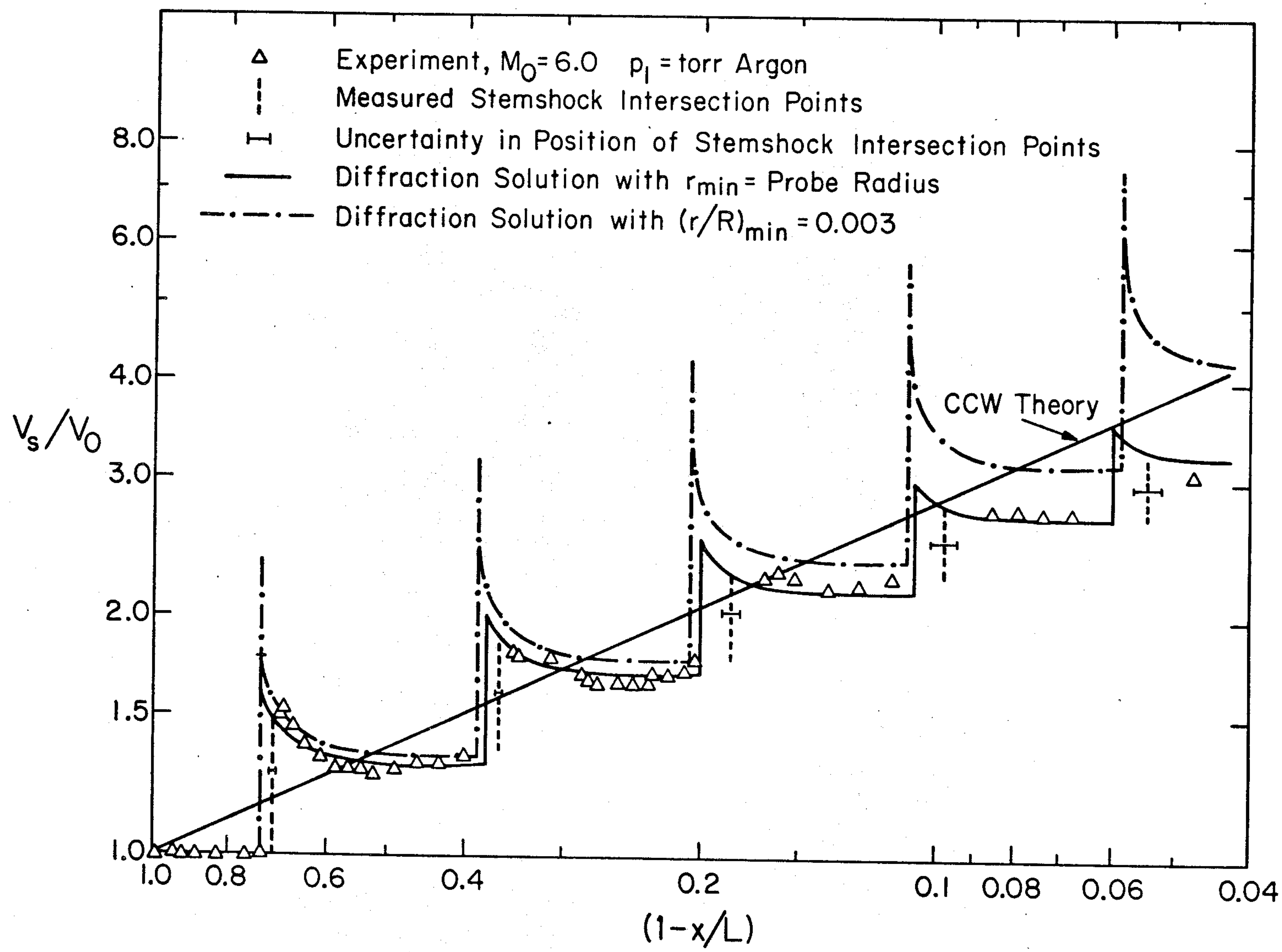

FIG. 10 INCIDENT SHOCK VELOCITY PROFILE, THEORY AND EXPERIMENT

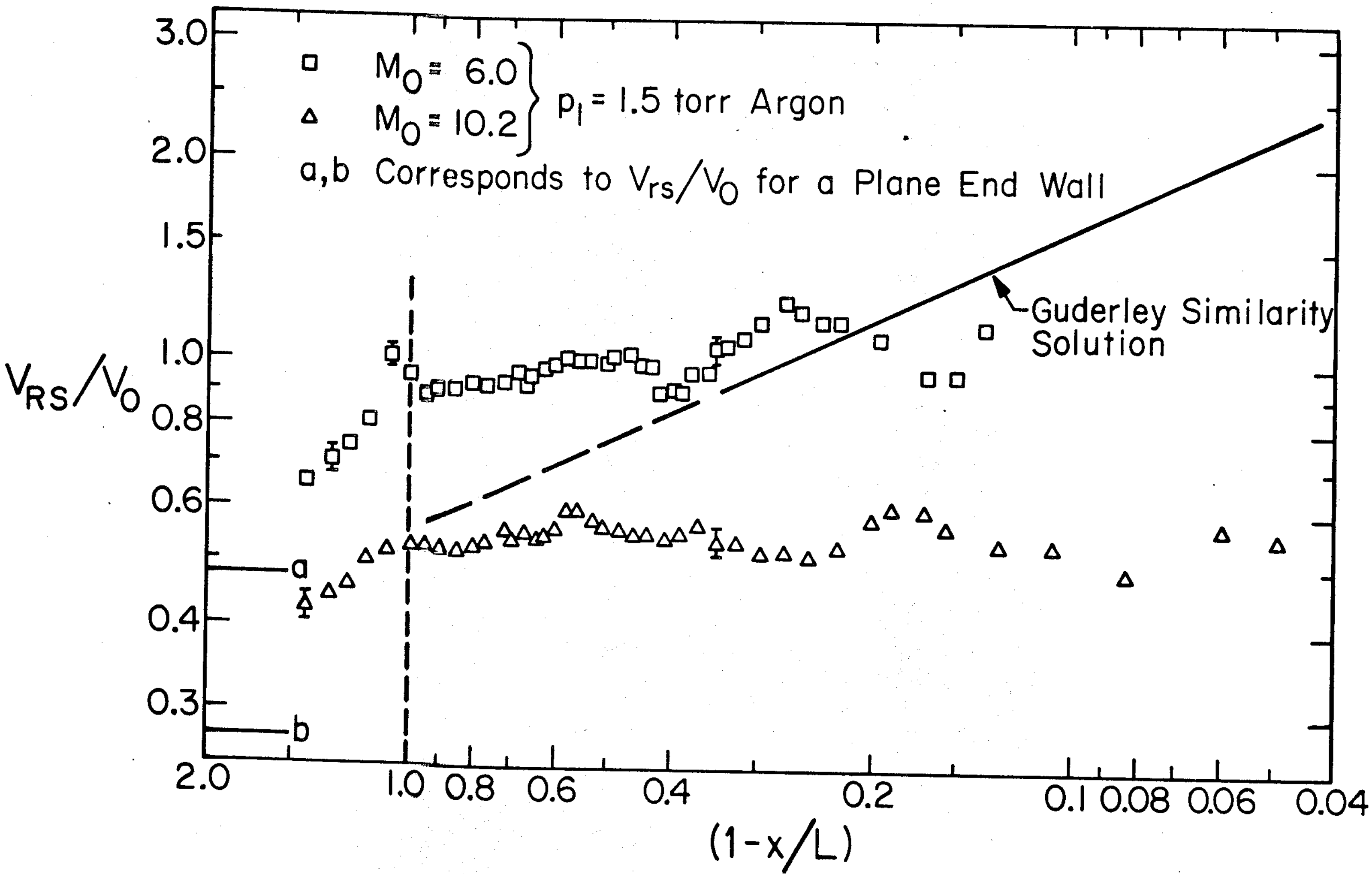

FIG. 11 REFLECTED SHOCK VELOCITY MEASUREMENTS

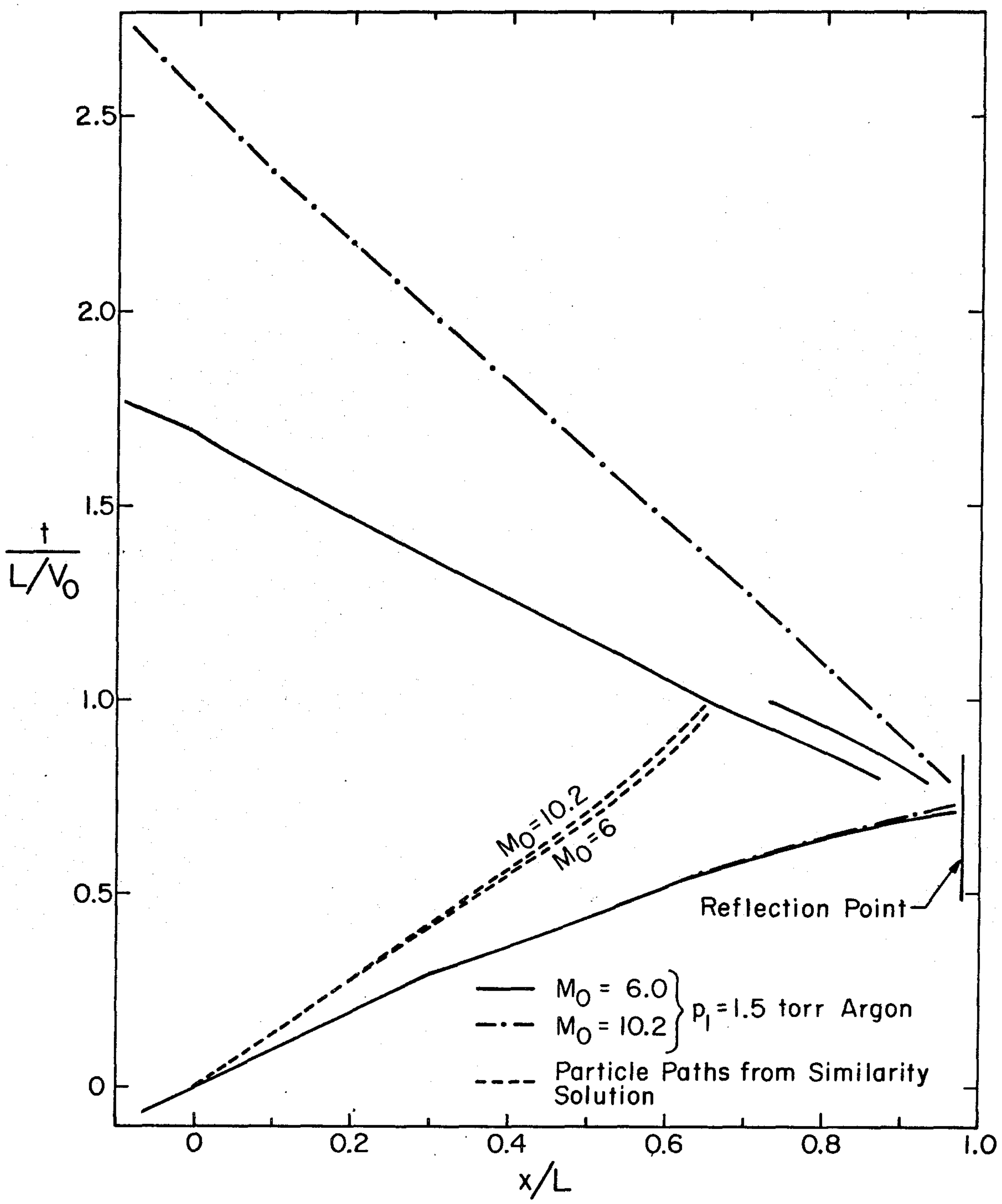

FIG. 12 INCIDENT AND REFLECTED SHOCK TRAJECTORIES

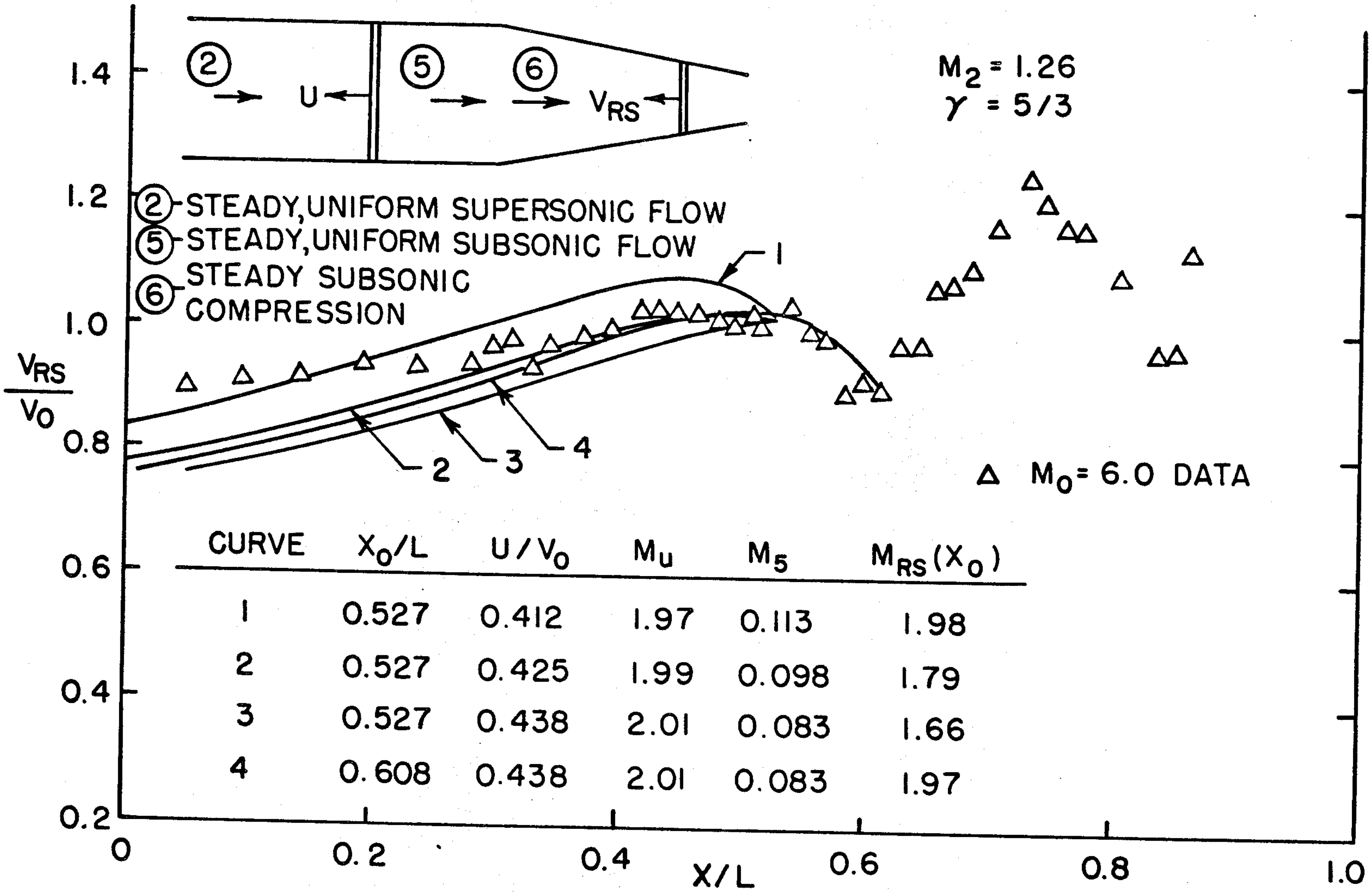

FIG. 13 REFLECTED SHOCK PROPAGATING INTO A STEADY, SUBSONIC FLOW

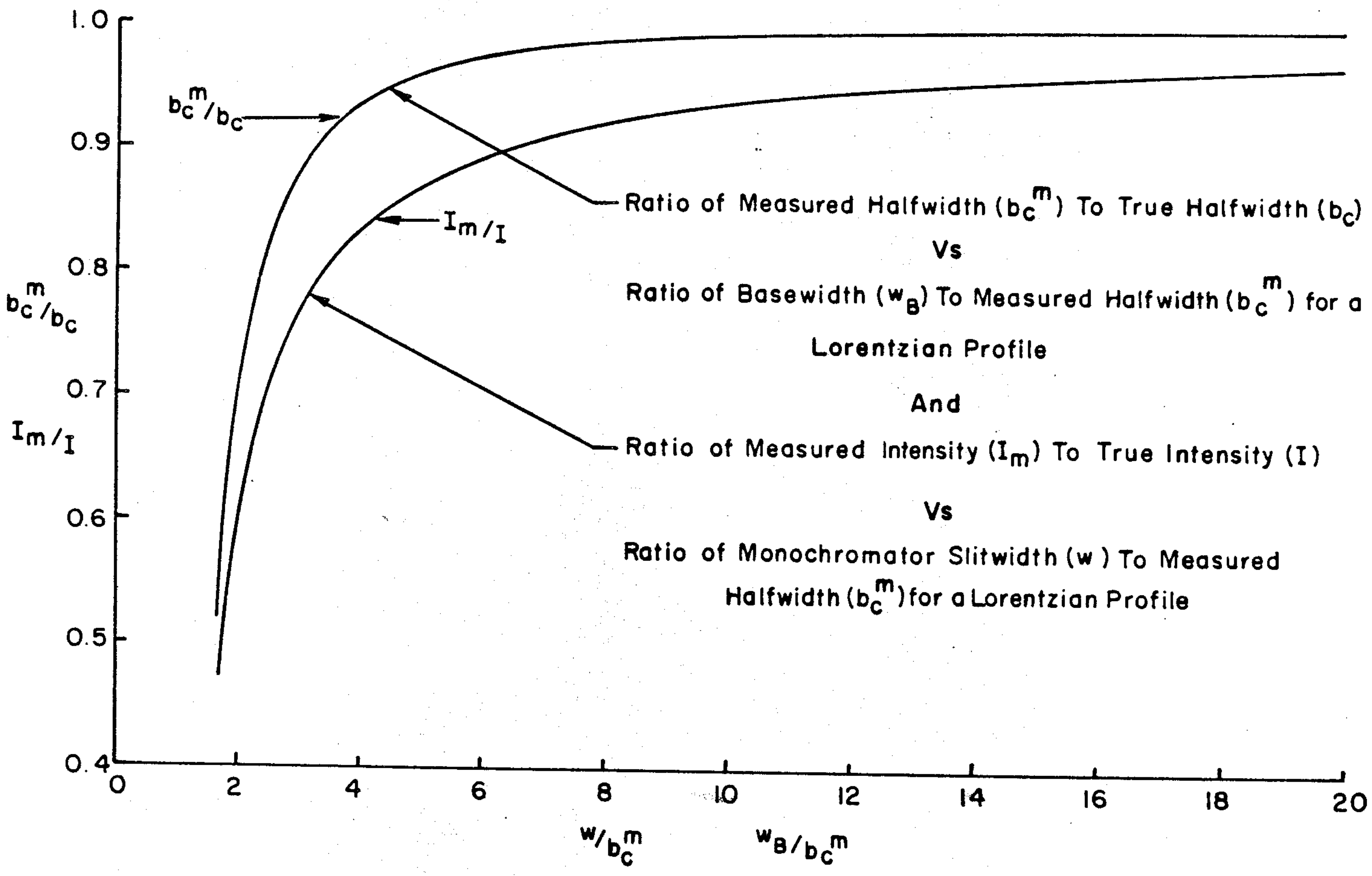

FIG. 14 THE EFFECT OF MONOCHROMATOR SLIT WIDTH AND EFFECTIVE BASE WIDTH ON EXPERIMENTALLY DETERMINED QUANTITIES FOR A LORENTZIAN PROFILE

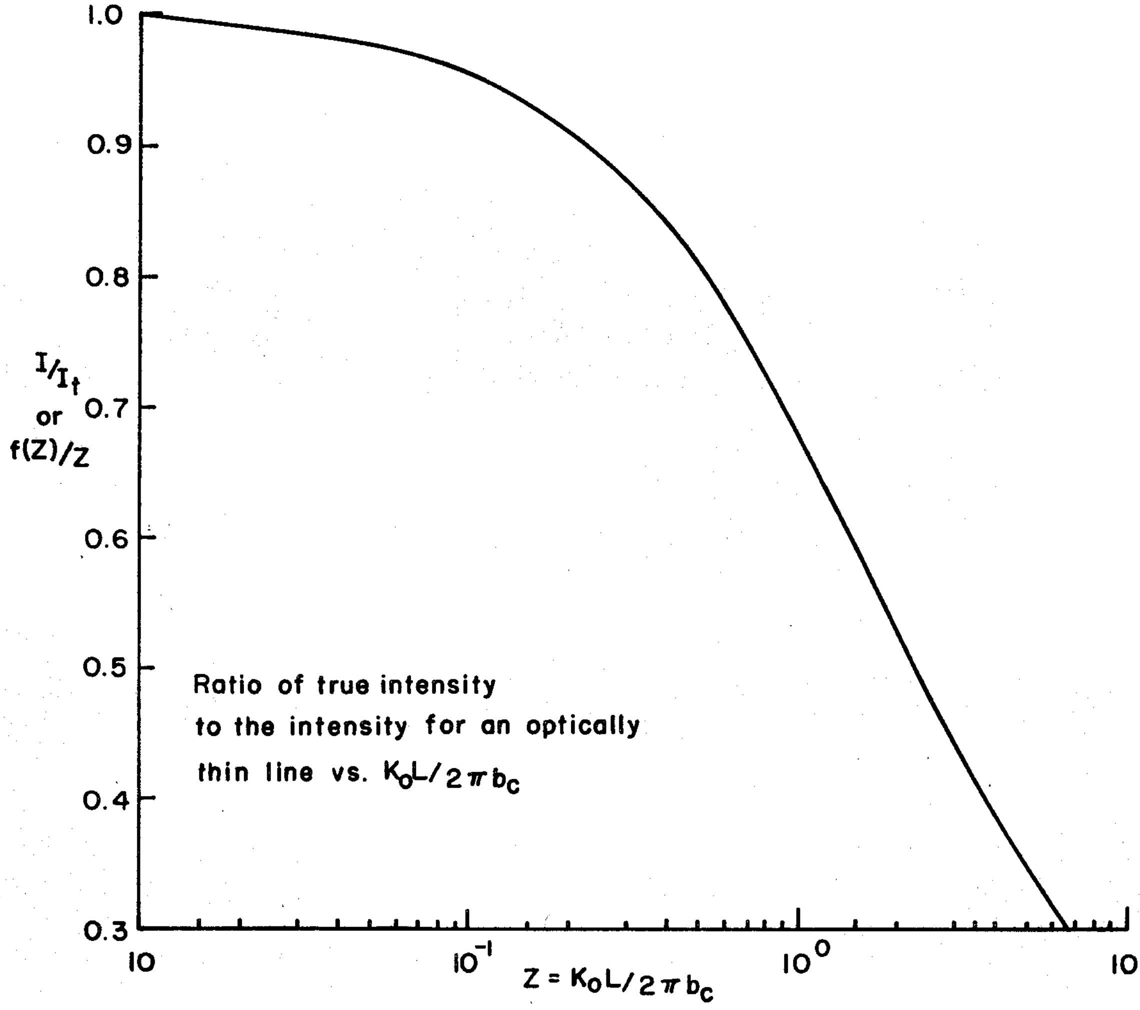

FIG. 15 EFFECT OF ABSORPTION ON SPECTRAL LINES DOMINATED BY STARK BROADENING

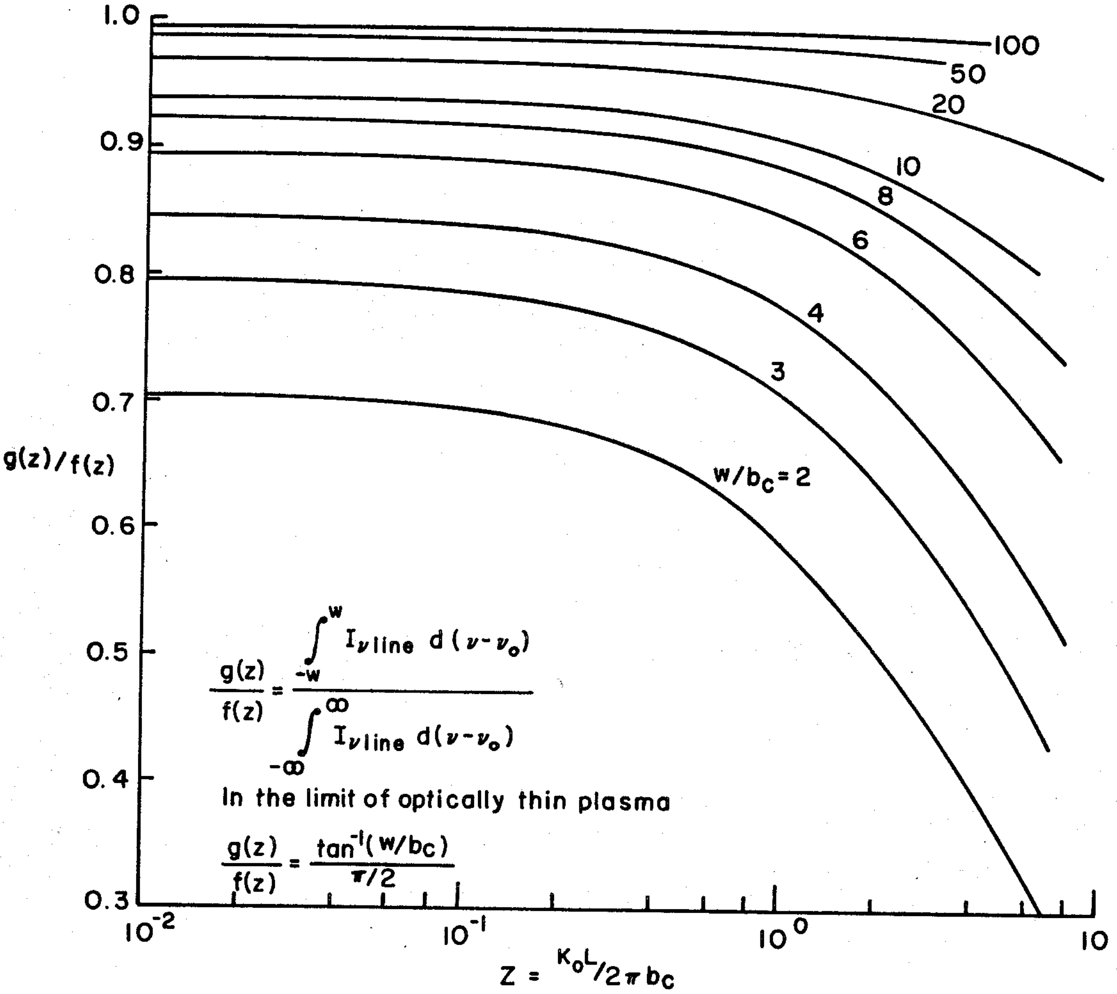

FIG. 16 THE EFFECT OF MONOCHROMATOR SLIT WIDTH ON SELF ABSORPTION AS A FUNCTION OF $K_oL/2\pi b_c$

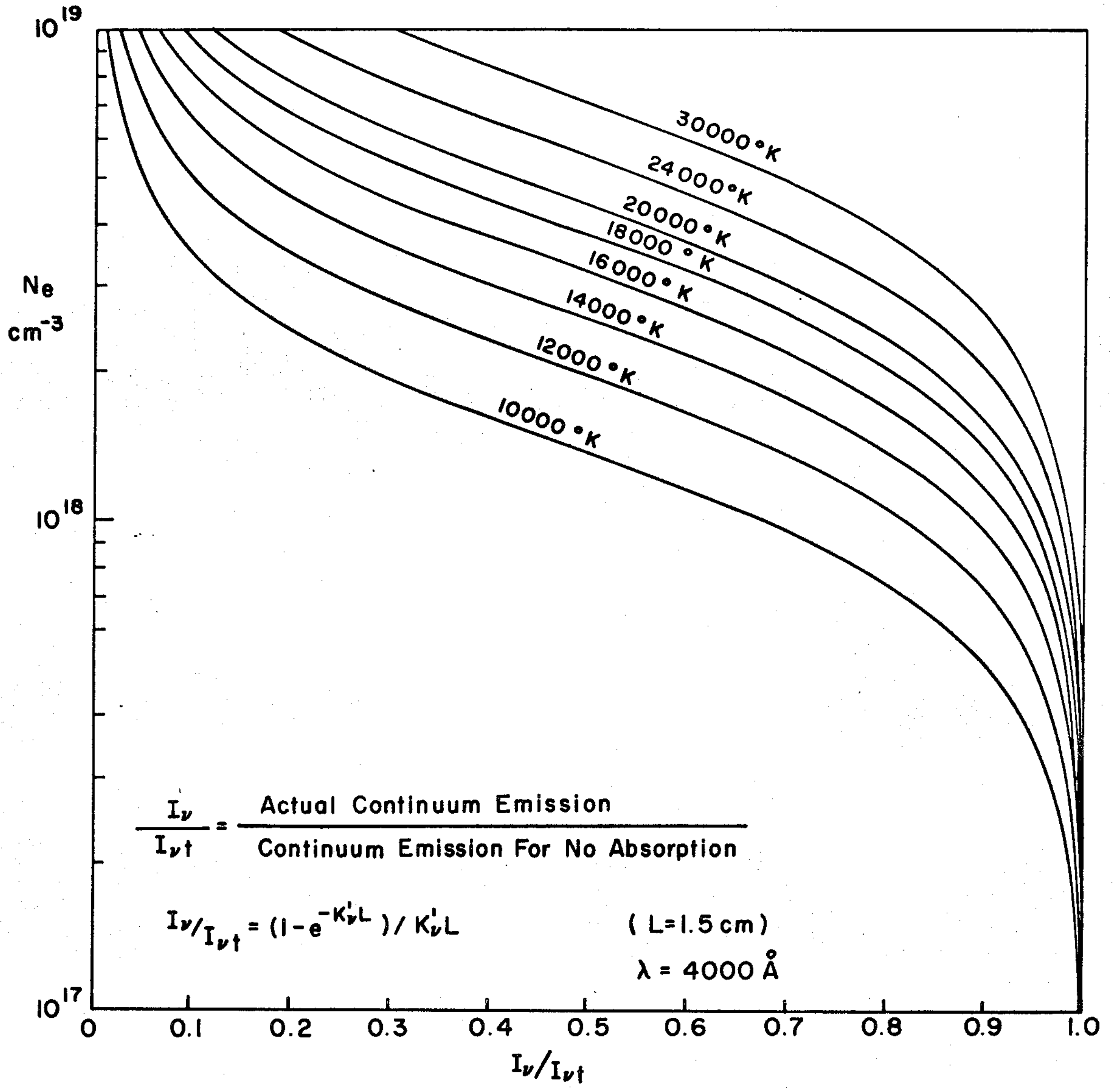

FIG. 17 EFFECT OF ABSORPTION ON CONTINUUM INTENSITY

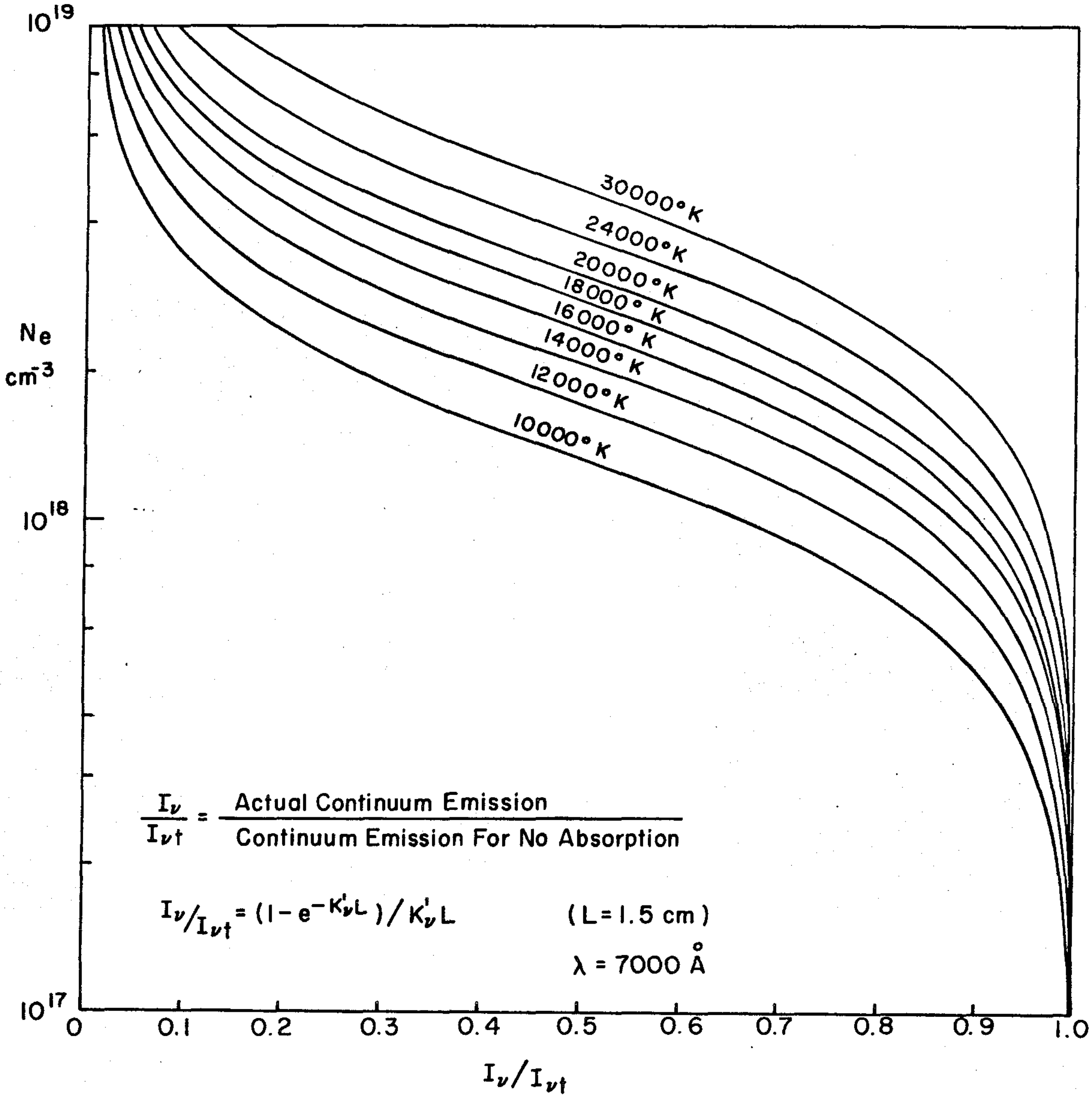

FIG. 18 EFFECT OF ABSORPTION ON CONTINUUM INTENSITY

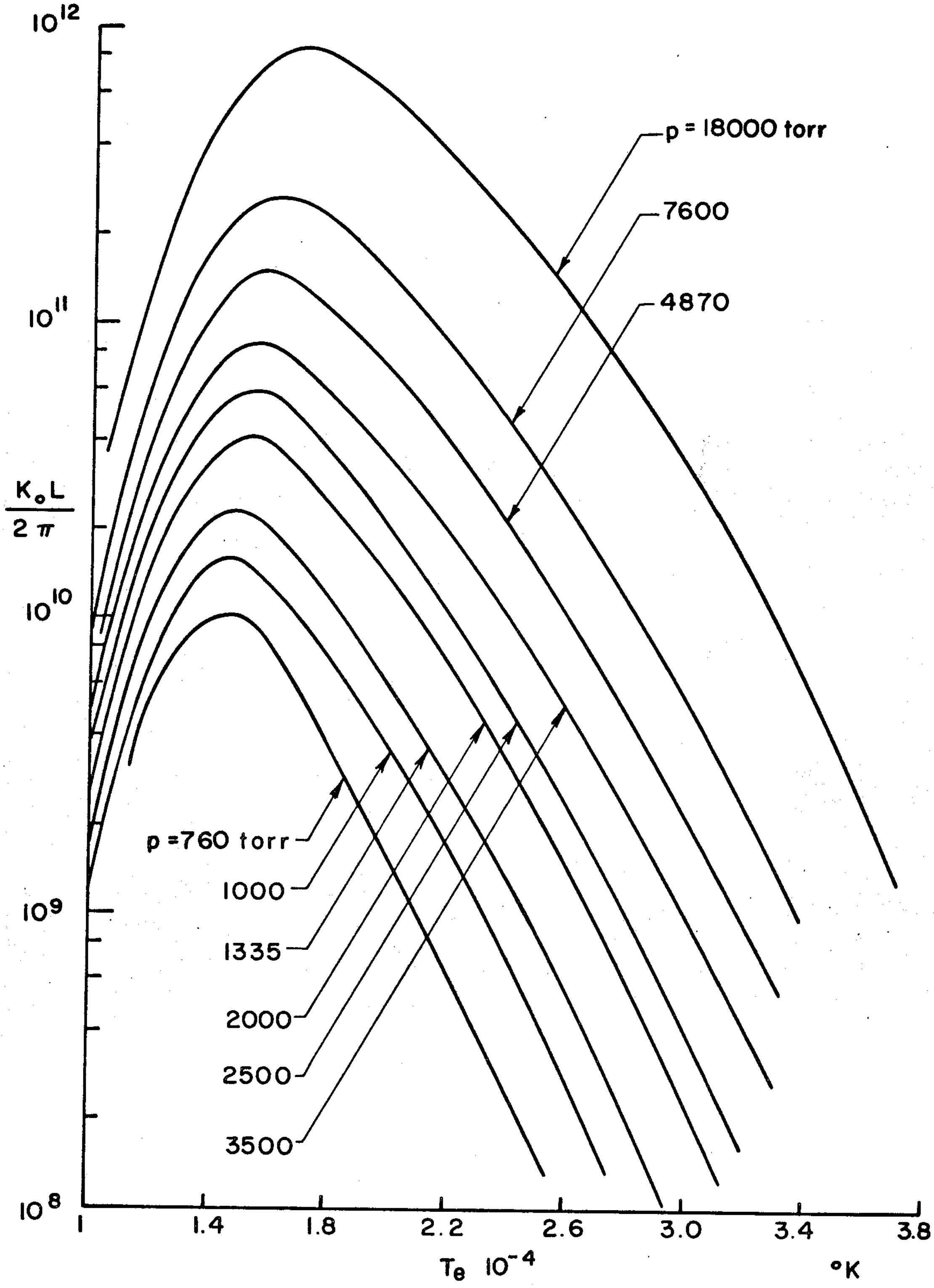

FIG. 19 INTEGRATED ABSORPTION FOR L = 1.5 cm. VS. TEMPERATURE FOR THE 6965.4 AND 7067.2 NEUTRAL ARGON LINES

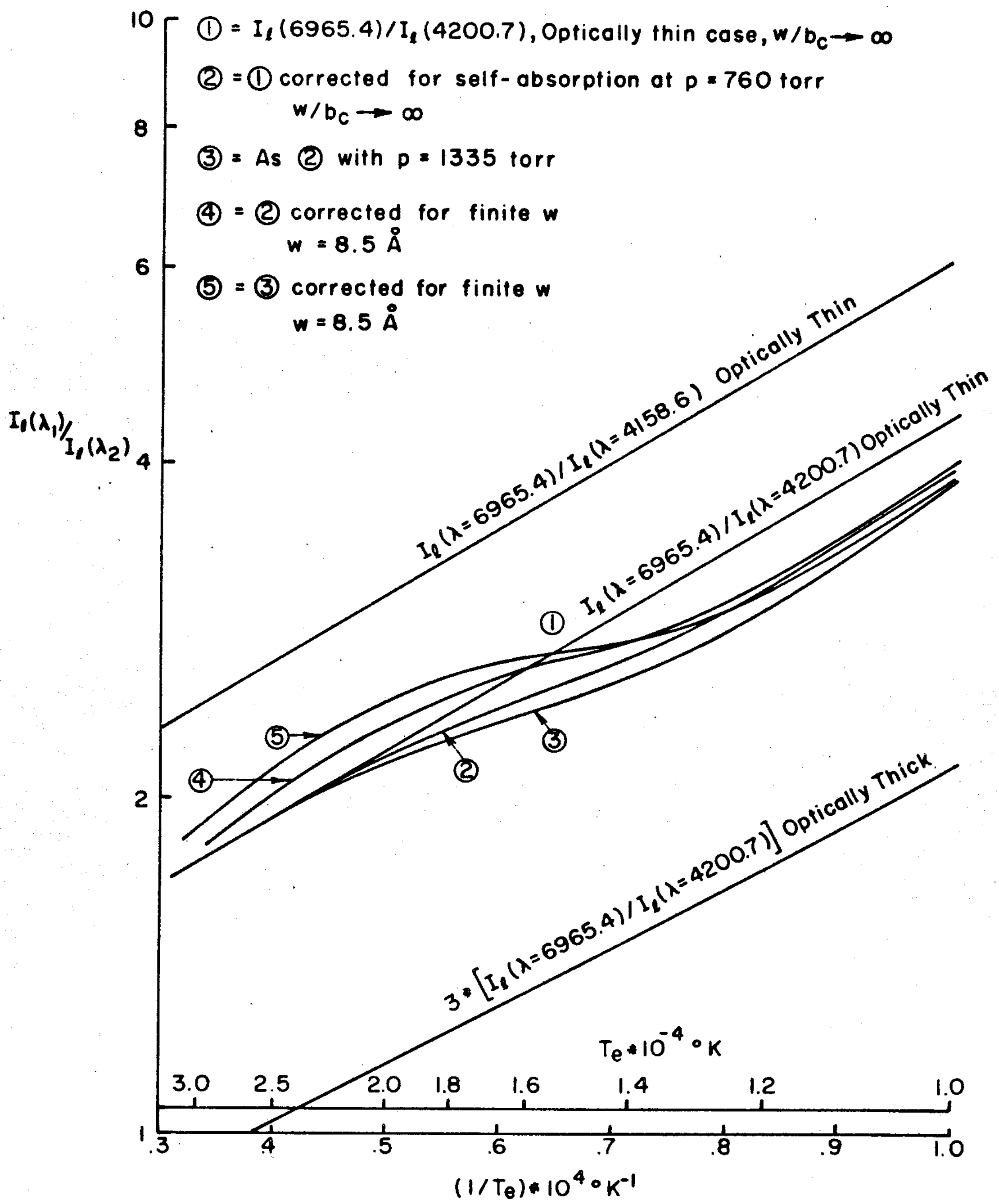

FIG. 20 RATIO OF INTEGRATED LINE INTENSITIES VS T_e

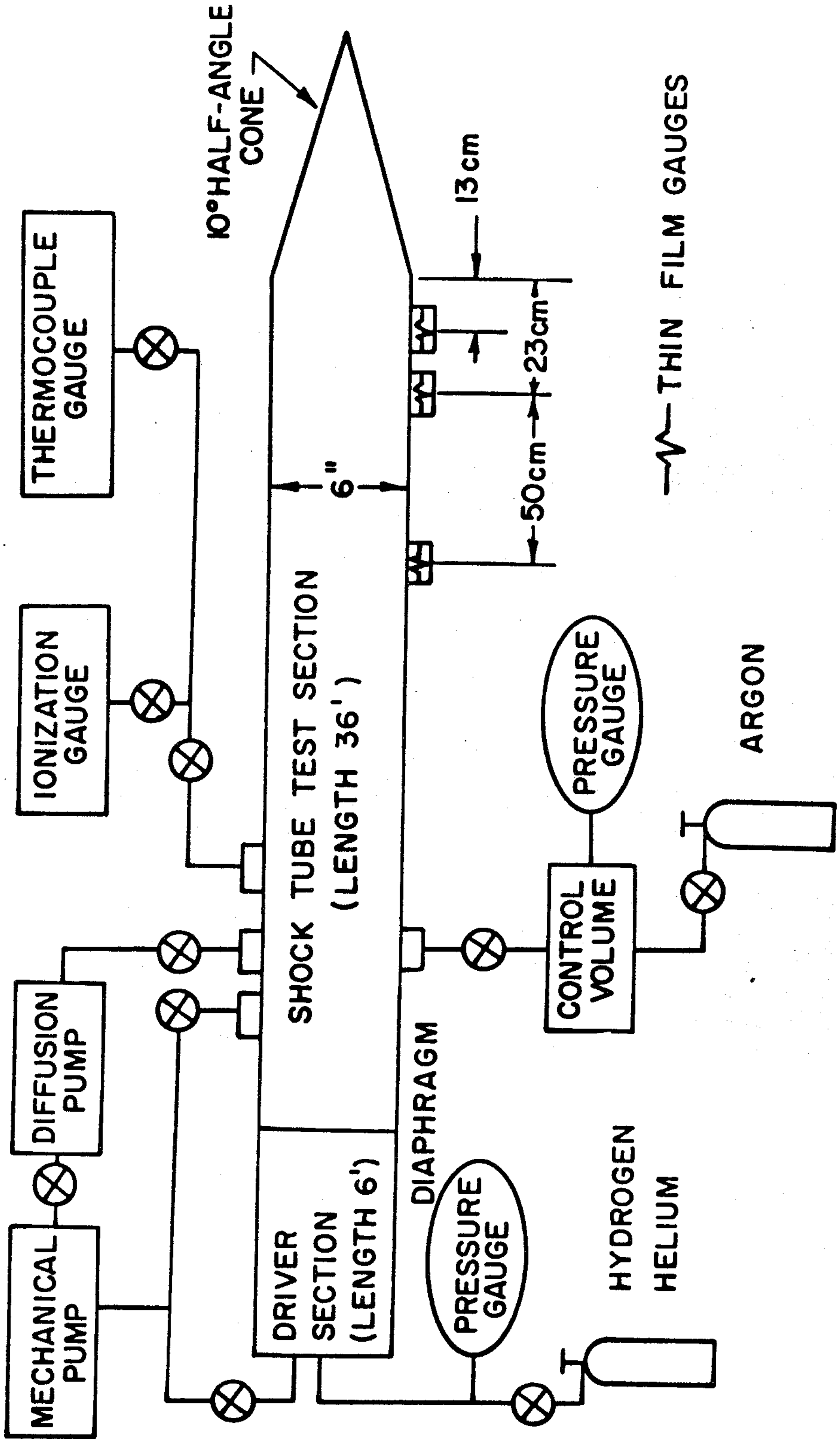

FIG. 21 GALCIT 6" SHOCK TUBE

Fig. 22 Second Section of 10° Half-Angle Cone with Windows

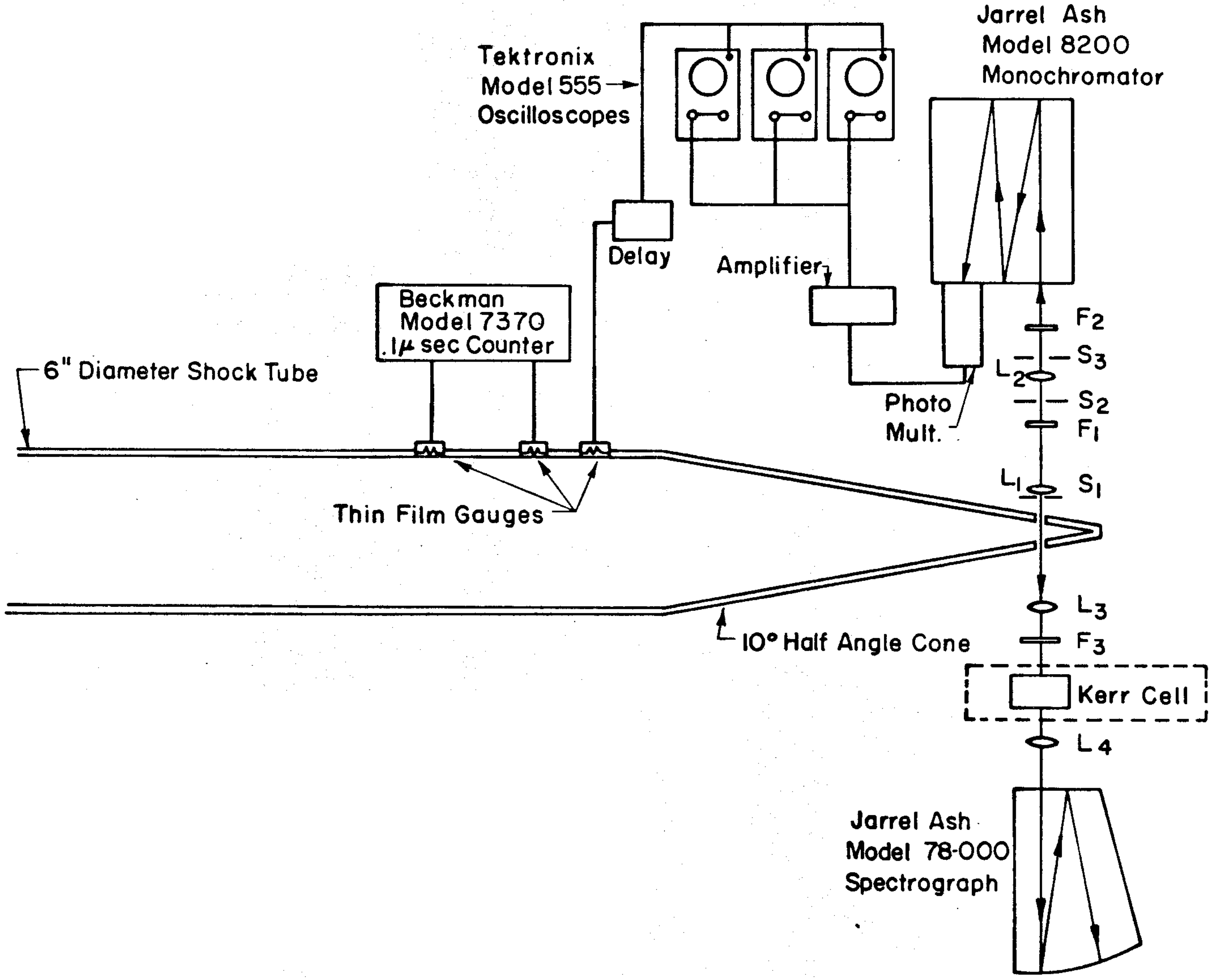

FIG. 23 OPTICAL SYSTEM

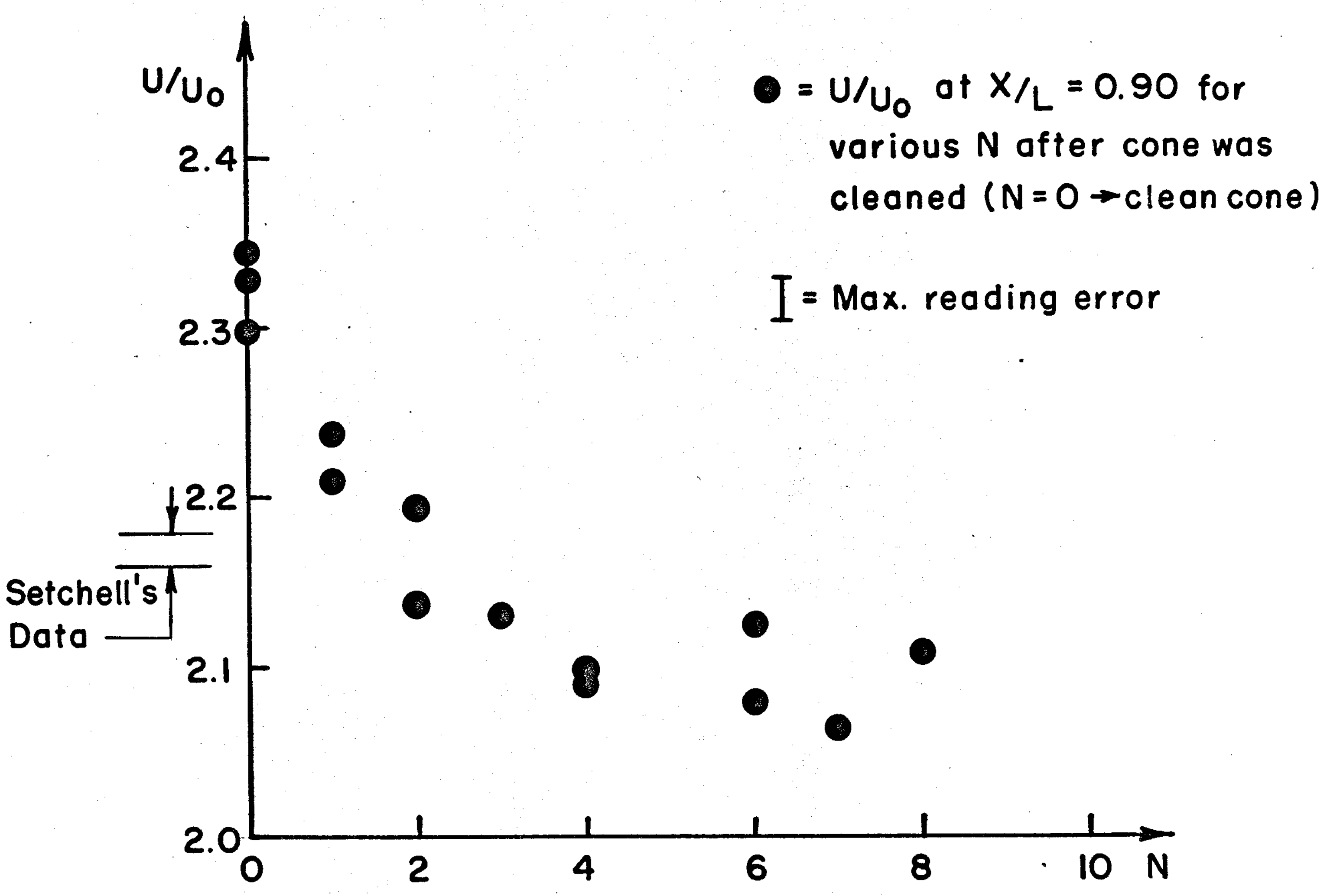

FIG. 24 THE EFFECT OF A CLEAN OR "COATED" CONE ON THE SHOCK VELOCITY AT X/L = 0.90

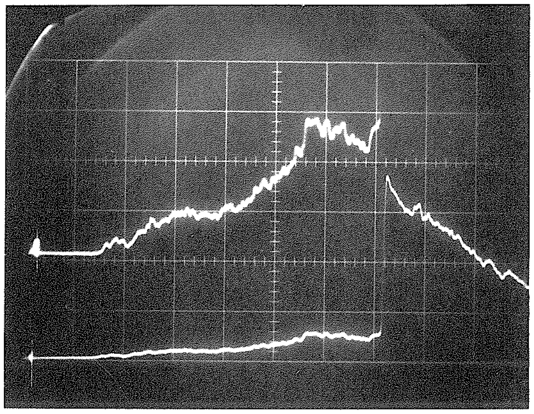

λ = 6752.8 Å

Upper beam: 0.2 v/div,
5 μsec/div

Lower beam: 0.5 v/div,
5 μsec/div

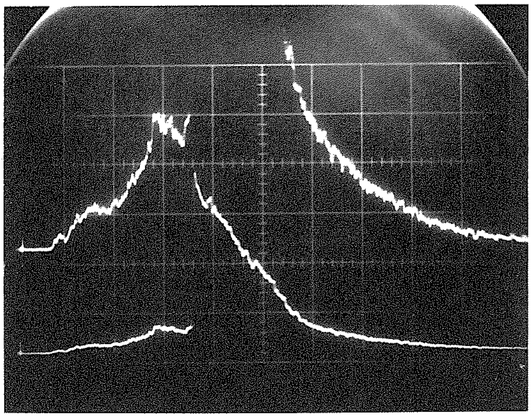

λ = 6752.8 Å

Upper beam: 0.1 v/div,
10 μsec/div

Lower beam: 0.5 v/div,
10 μsec/div

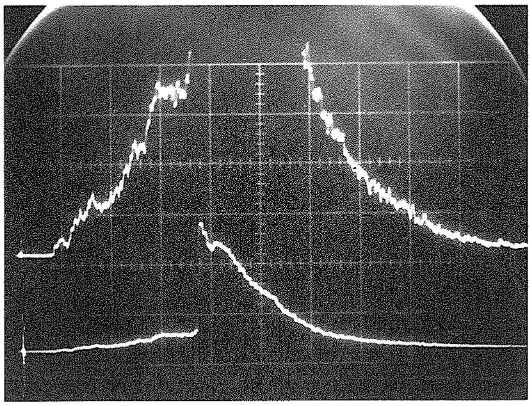

λ = 4200.7 Å

Upper beam: 0.1 v/div,
10 μsec/div

Lower beam: 1 v/div.
10 μsec/div

Fig. 25 Photomultiplier Output for Line Intensity Measurements.

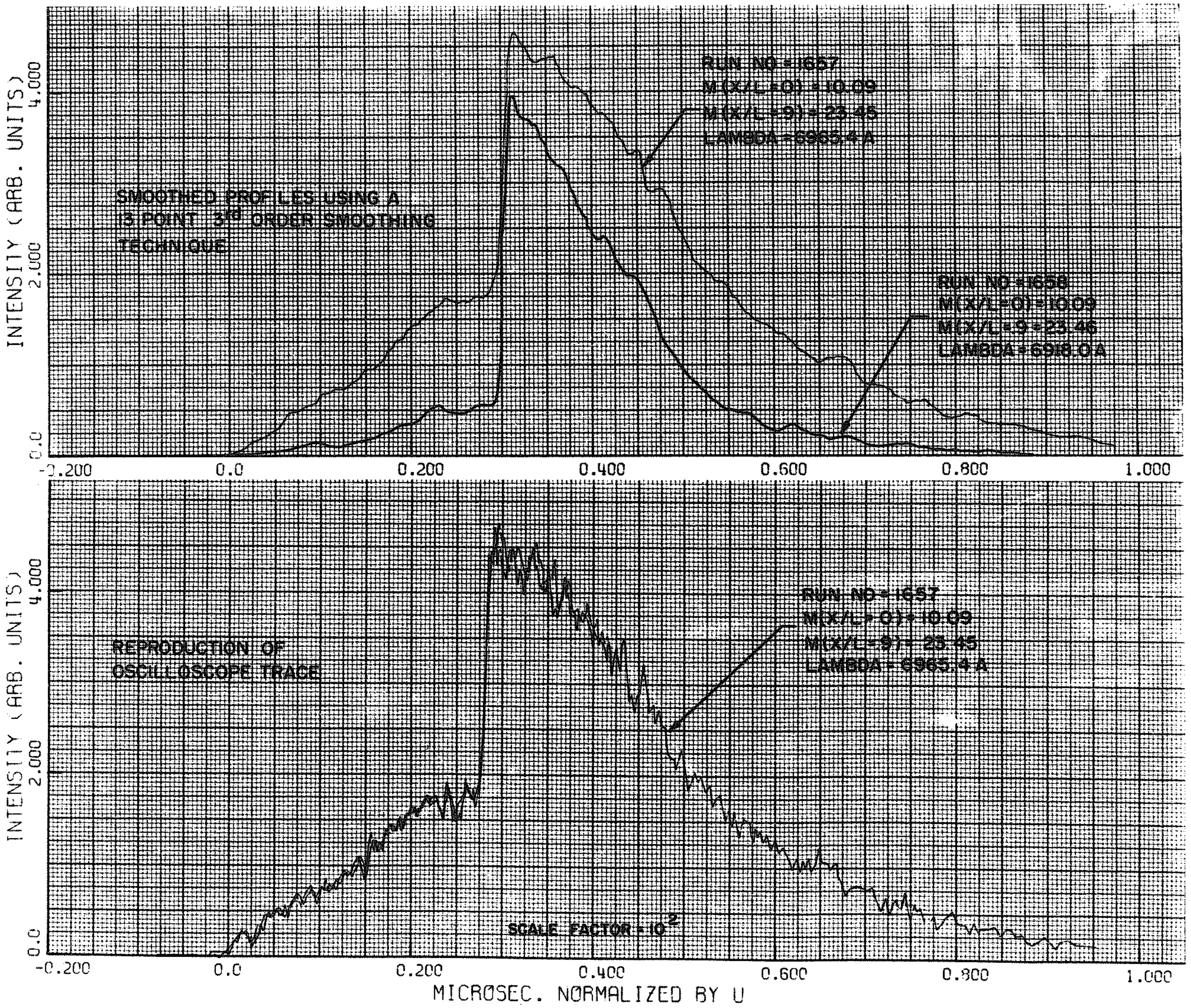

FIG. 26 CALCOMP PLOTTER RESULT OF DATA DIGITIZING PROCESS

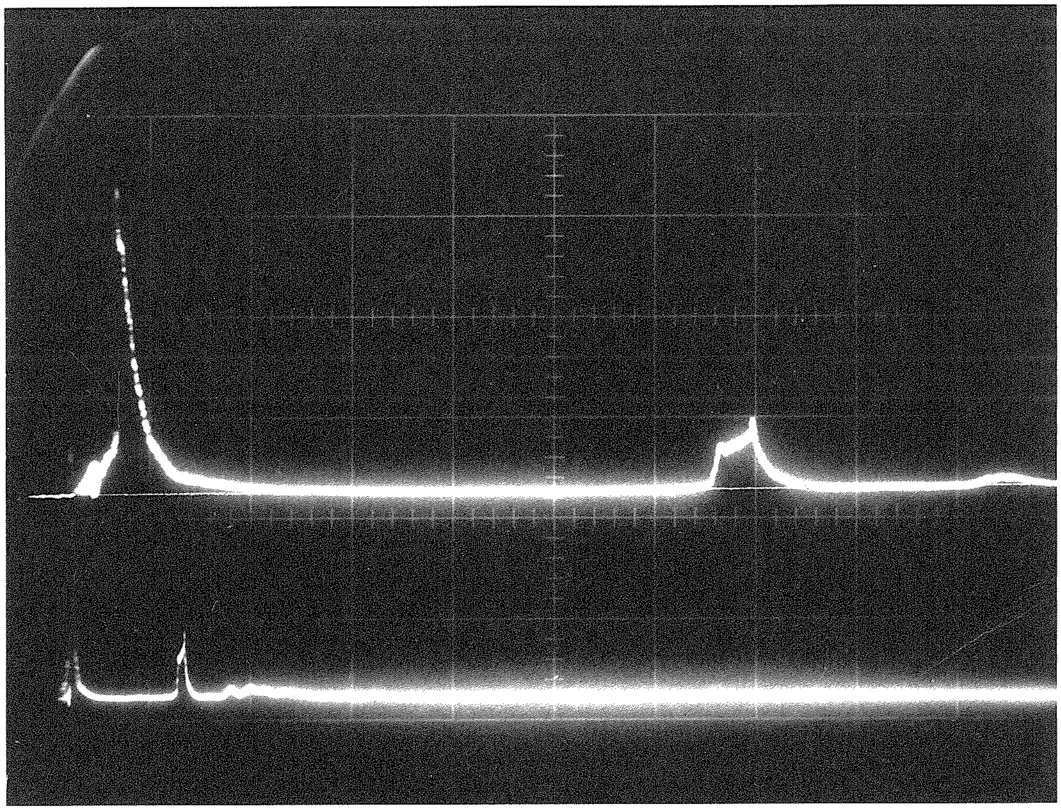

$\lambda = 6562.8$ Å (H_α)

Upper Beam: 0.5 v/div; 0.1 μsec/div

Lower Beam: 0.5 v/div; 0.5 μsec/div

Fig. 27 Emission from the H_α Line

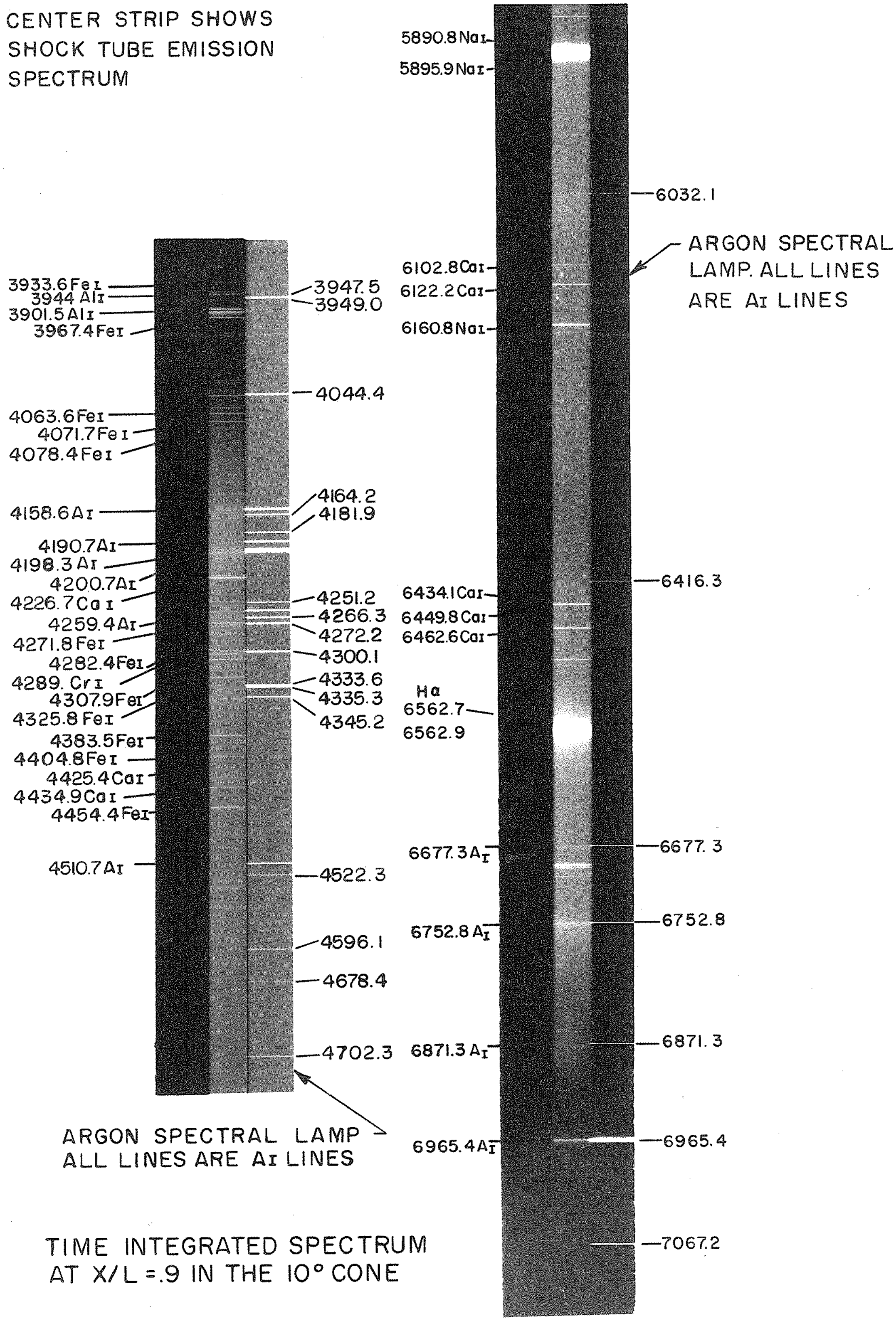

CENTER STRIP SHOWS SHOCK TUBE EMISSION SPECTRUM

TIME INTEGRATED SPECTRUM AT X/L =.9 IN THE 10° CONE

FIG. 28

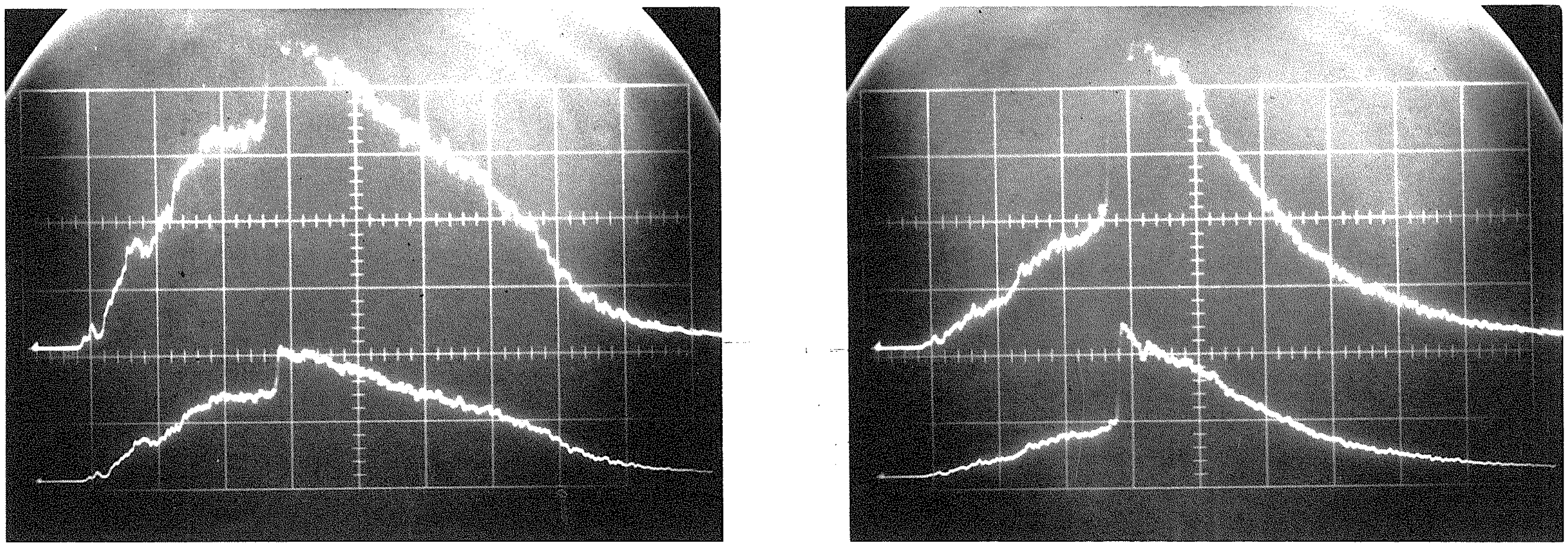

$\lambda = (6965.4 + 2.0)$ Å

$\lambda = (6965.4 - 2.0)$ Å

All traces 10 μsec/div.

Upper Beams: 0.2 v/div. Lower Beams: 0.5 v/div.

Fig. 29 Photomultiplier Output for Stark Broadening Measurements.

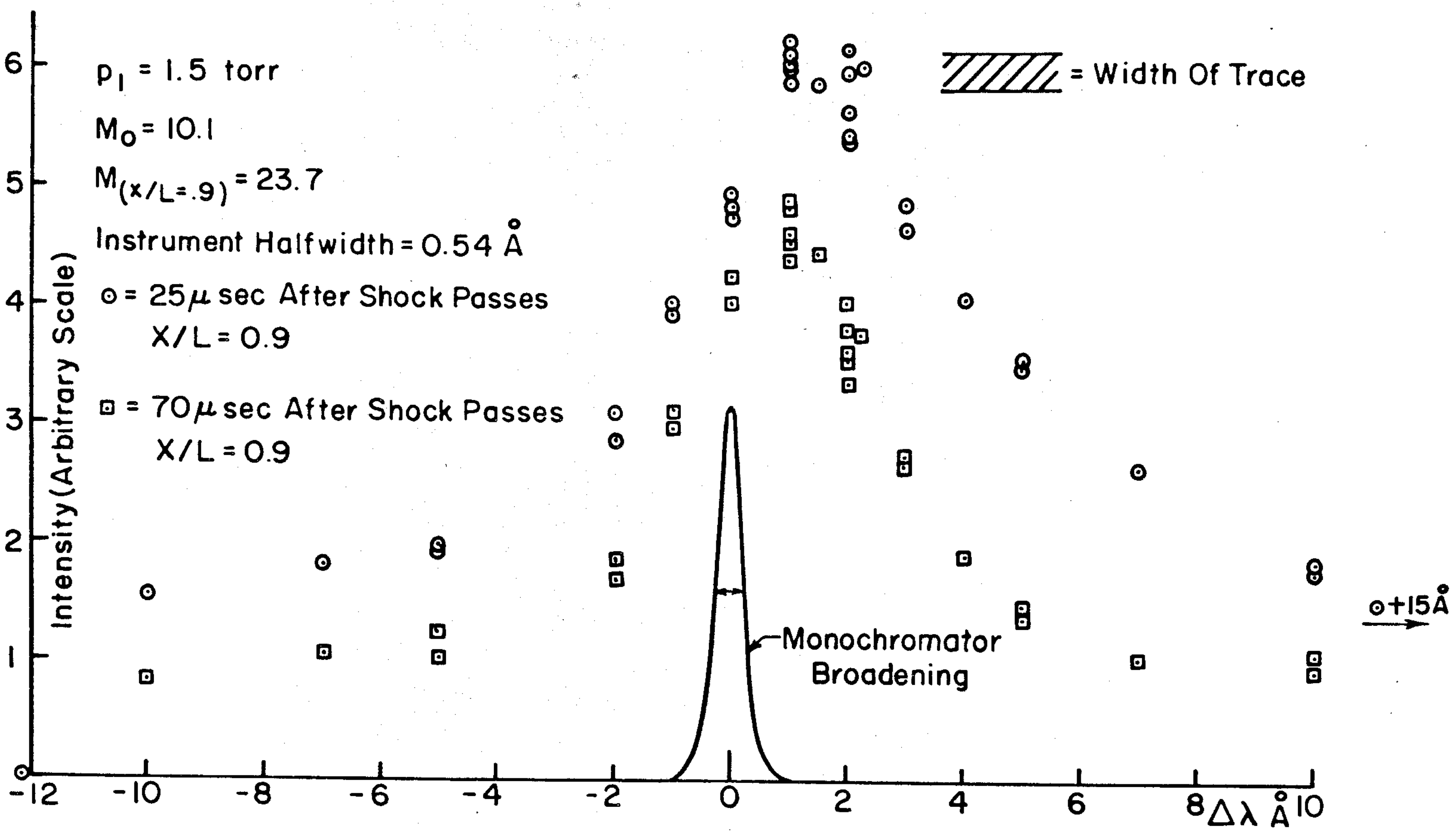

FIG.30 INTENSITY PROFILES OF THE NEUTRAL ARGON LINE 6965.4 Å AT X/L=0.9 IN THE 10°10' CONE

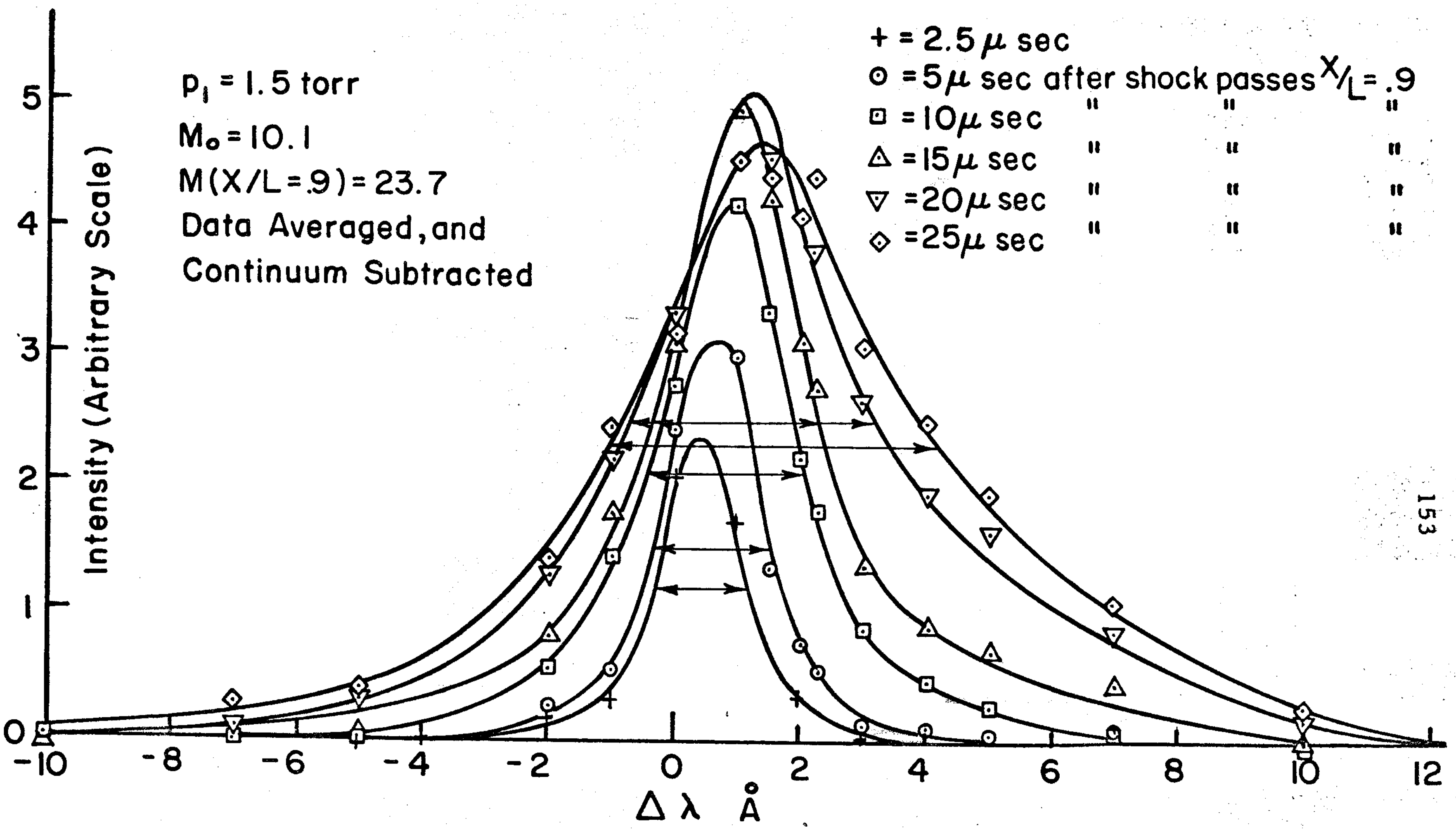

FIG. 31 INTENSITY PROFILES OF THE NEUTRAL ARGON LINE 6965.4 Å AT X/L = 0.9 IN THE 10° CONE

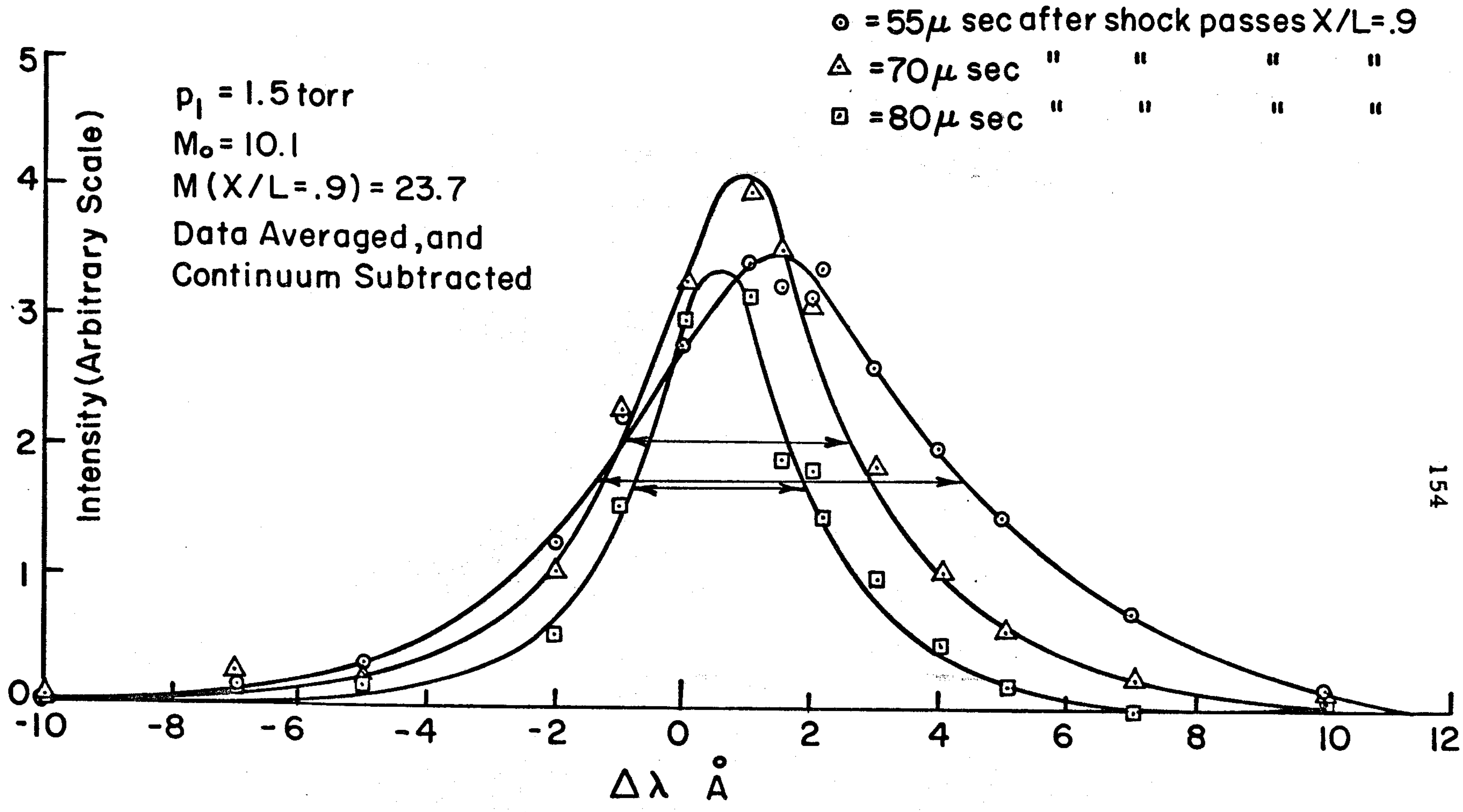

FIG.32 INTENSITY PROFILES OF THE NEUTRAL ARGON LINE 6965.4 Å AT X/L = 0.9 IN THE 10° CONE

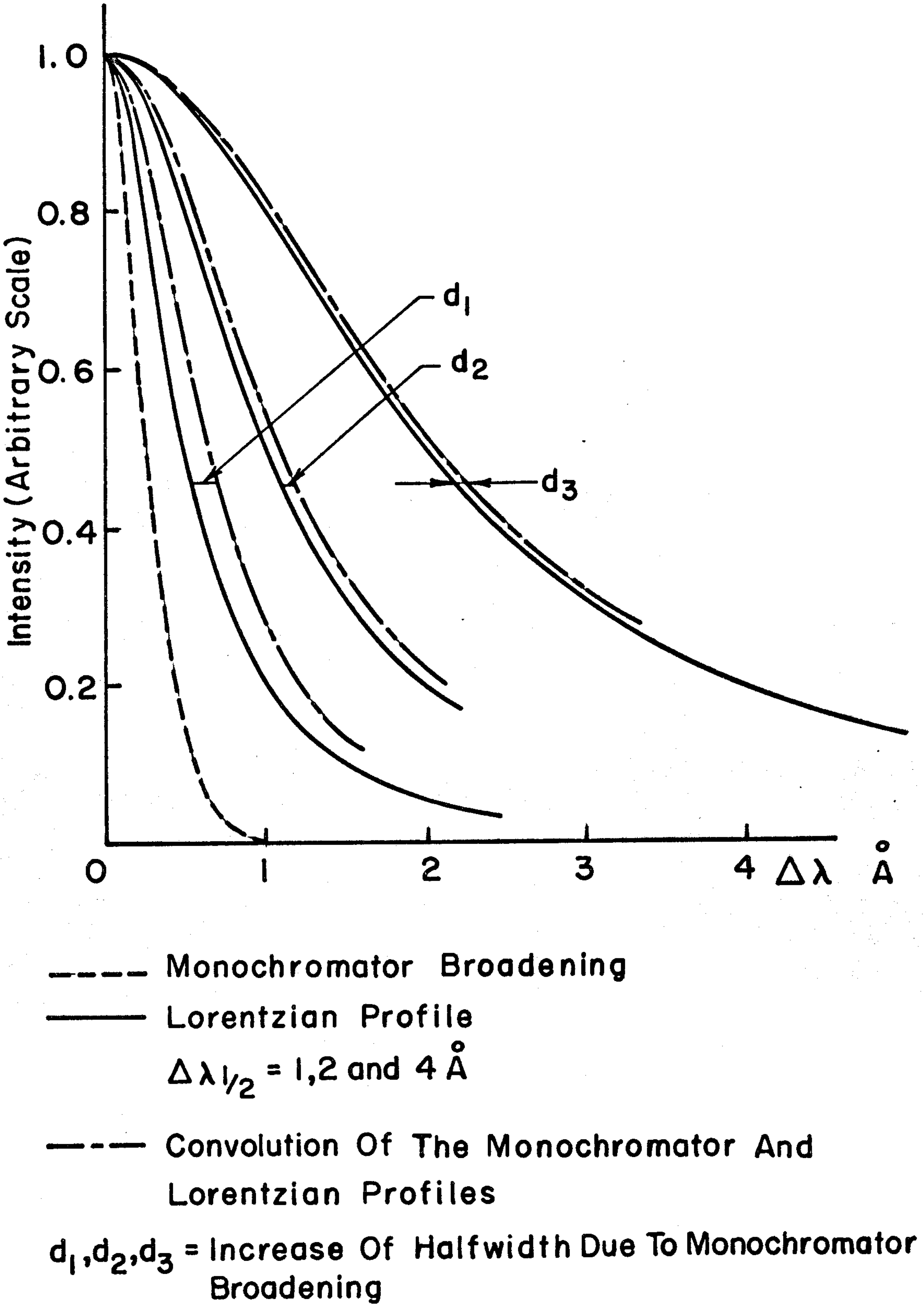

FIG.33a EFFECT OF MONOCHROMATOR BROADENING ON LORENTZIAN PROFILES

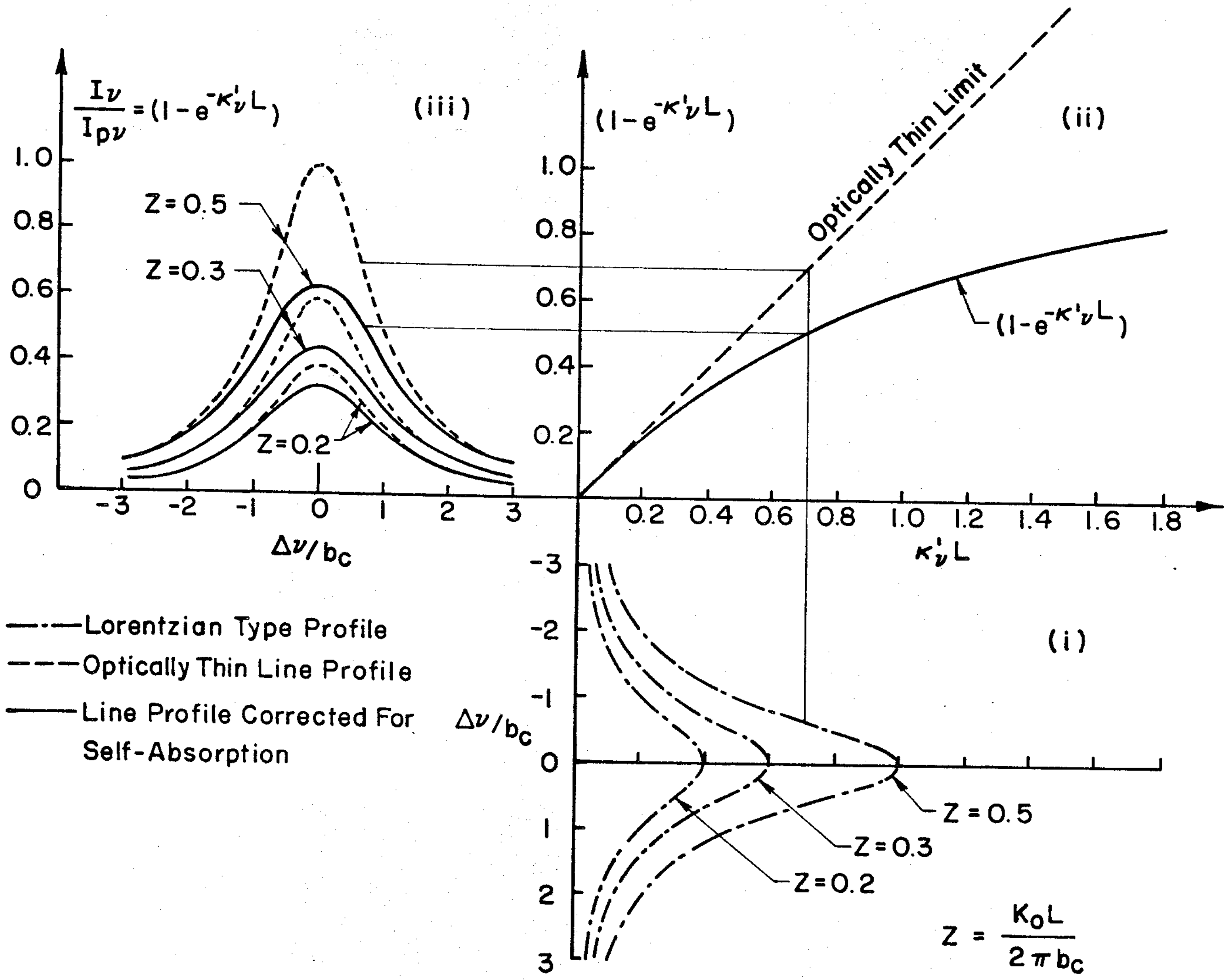

FIG. 33b EFFECT OF SELF-ABSORPTION ON LORENTZIAN LINE PROFILES

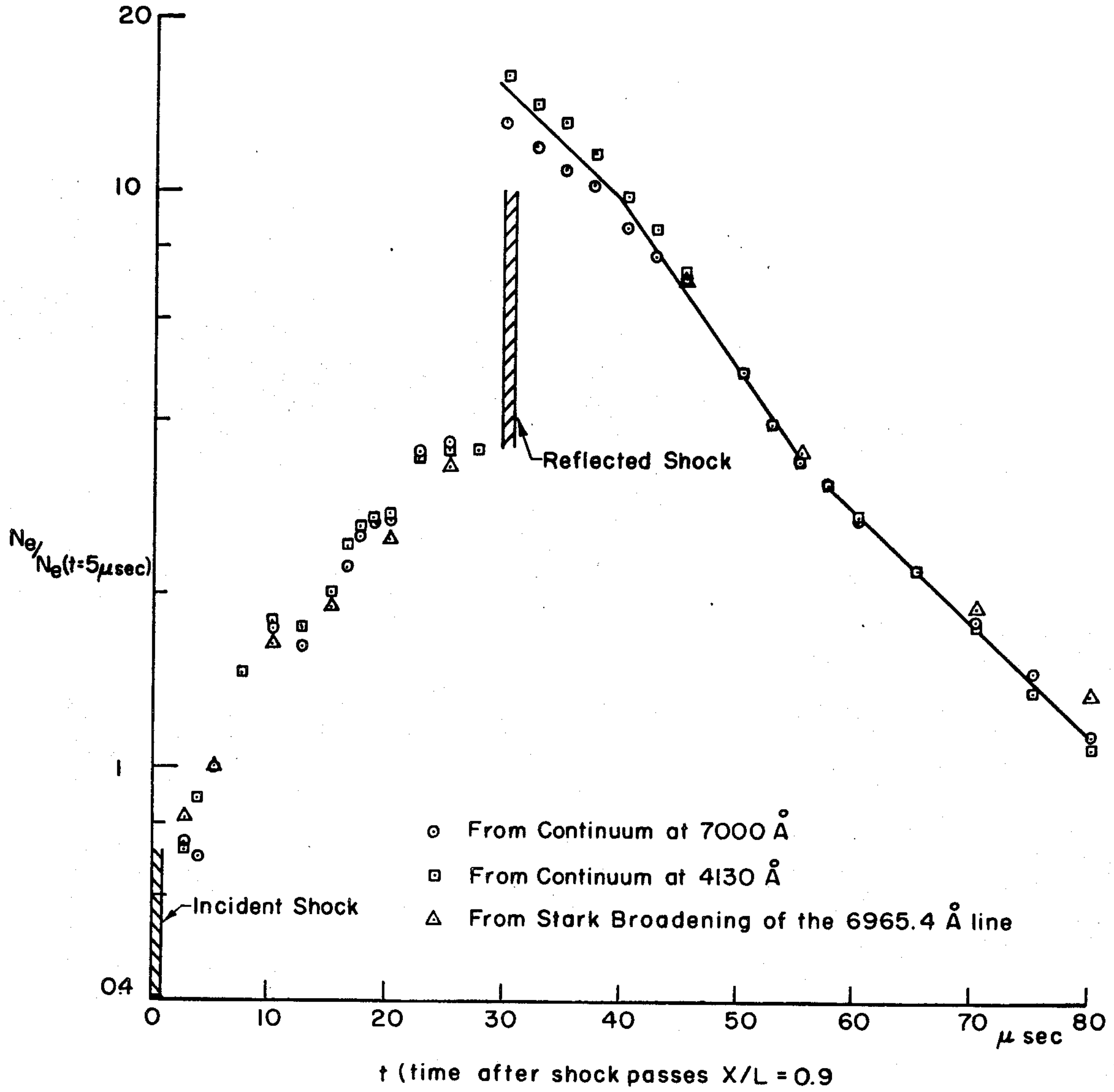

FIG.34 NORMALIZED ELECTRON NUMBER DENSITY AS DETERMINED BY STARK BROADENING AND RELATIVE CONTINUUM INTENSITY AT X/L = 0.9 IN THE 10° CONE

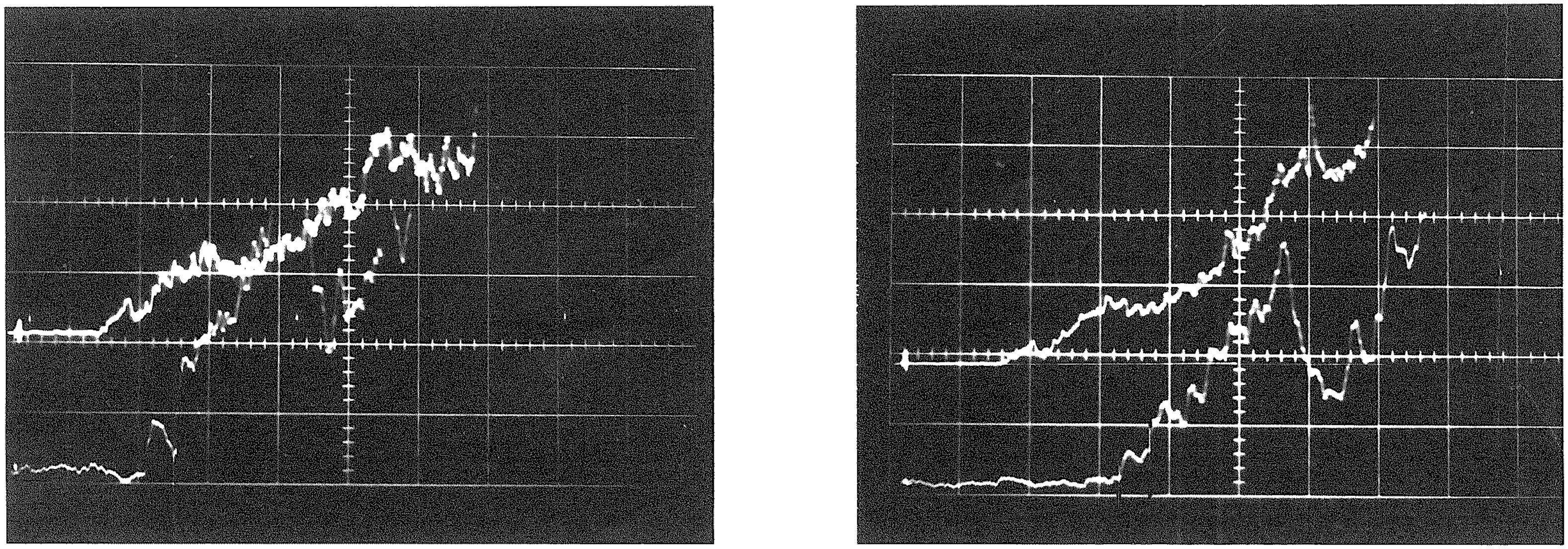

λ = 7067.2 Å

Upper beam: 0.05 v/div
Lower beam: 0.005 v/div

λ = 4158.6 Å

Upper beam: 0.1 v/div
Lower beam: 0.01 v/div

Upper beams: 5 μsec/div   Lower beams: 1 μsec/div

Fig. 35 Photomultiplier Output for Line Intensity Measurements

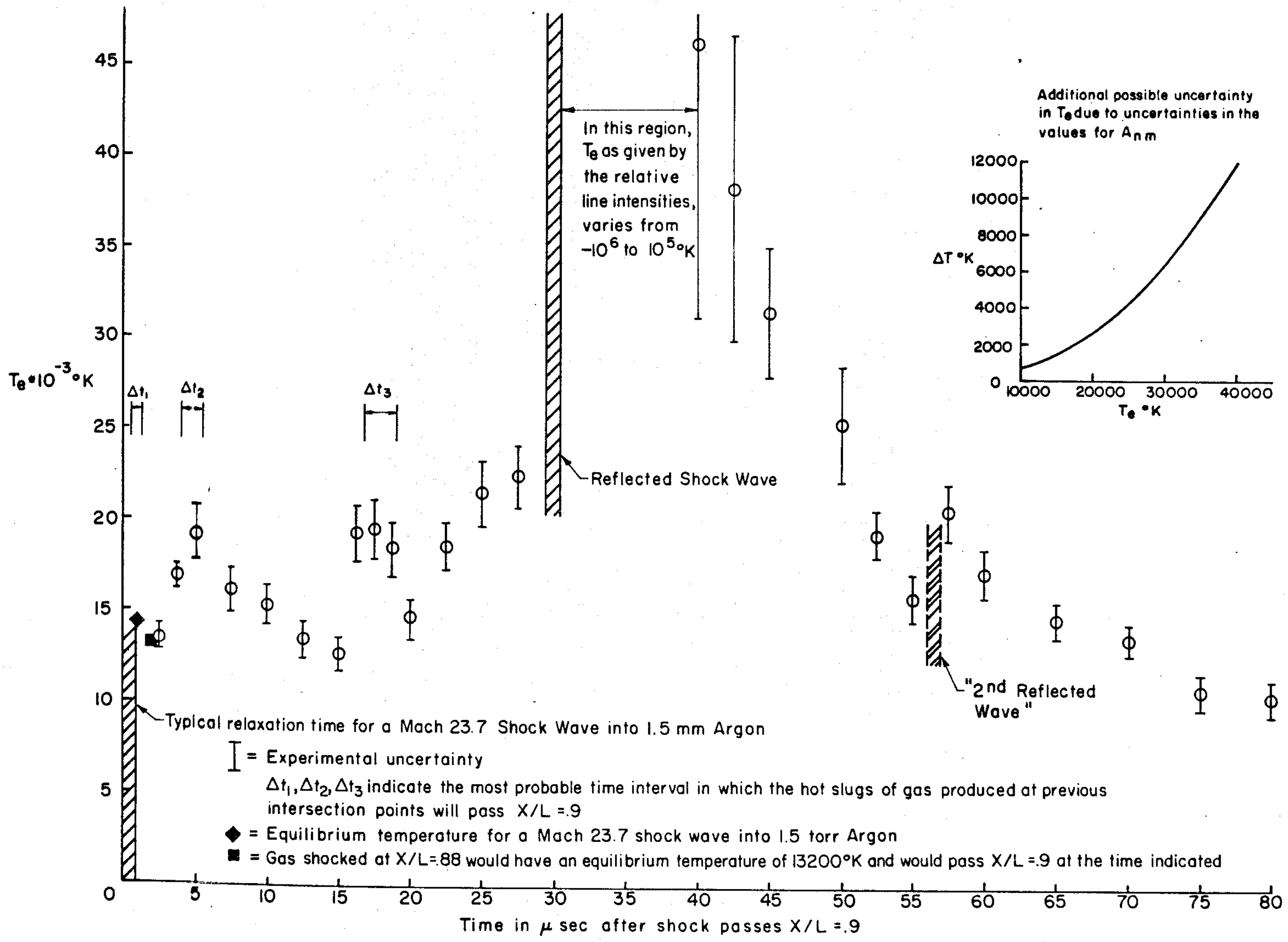

FIG 36 ELECTRON TEMPERATURE T_e AS DETERMINED BY RELATIVE LINE INTENSITY METHOD AS A FUNCTION OF TIME AFTER THE SHOCK PASSES X/L =.9 IN THE 10° CONE

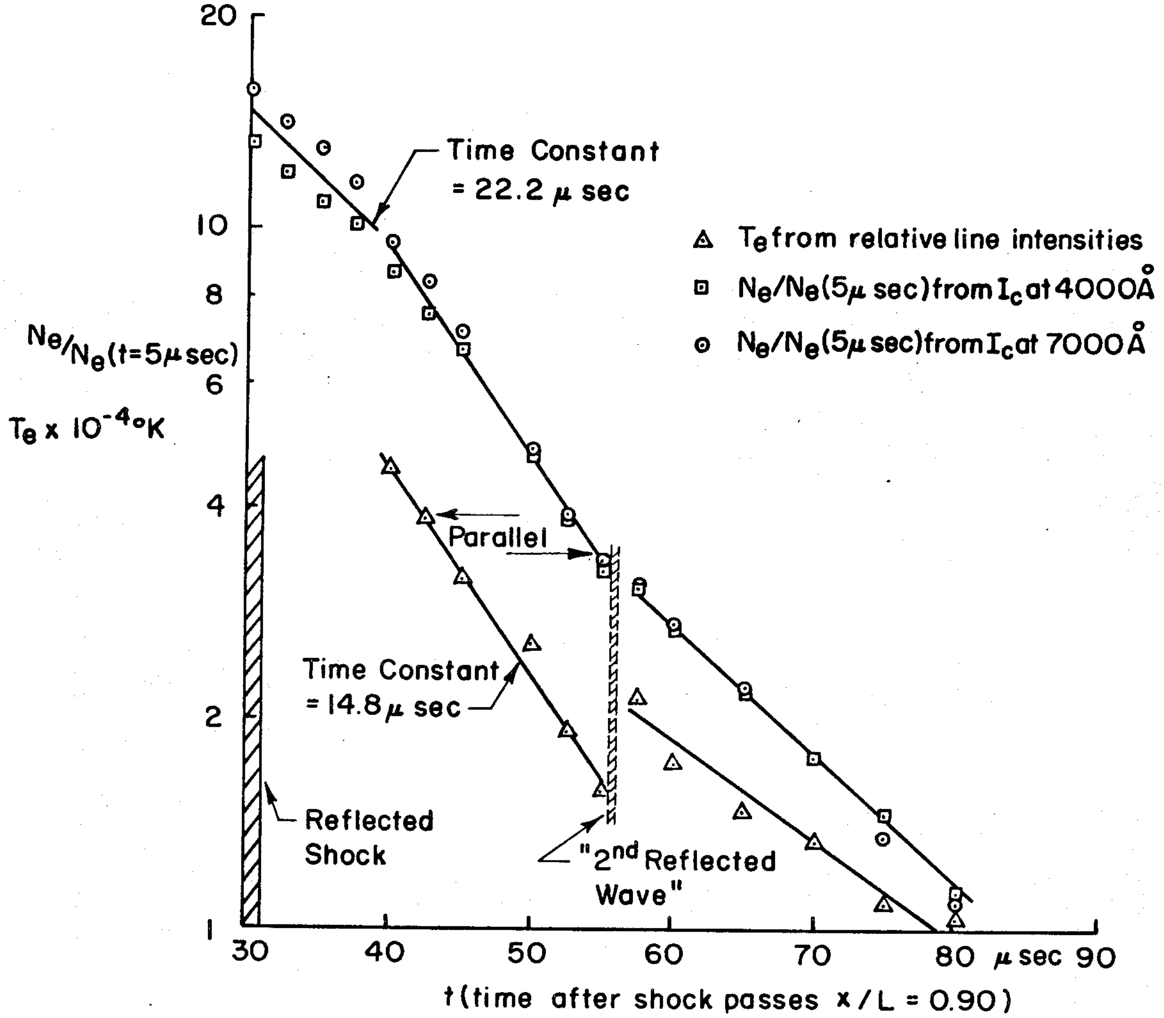

FIG. 37 NORMALIZED ELECTRON NUMBER DENSITY AND ELECTRON TEMPERATURE VS TIME AT X/L = 0.90 IN THE 10° CONE

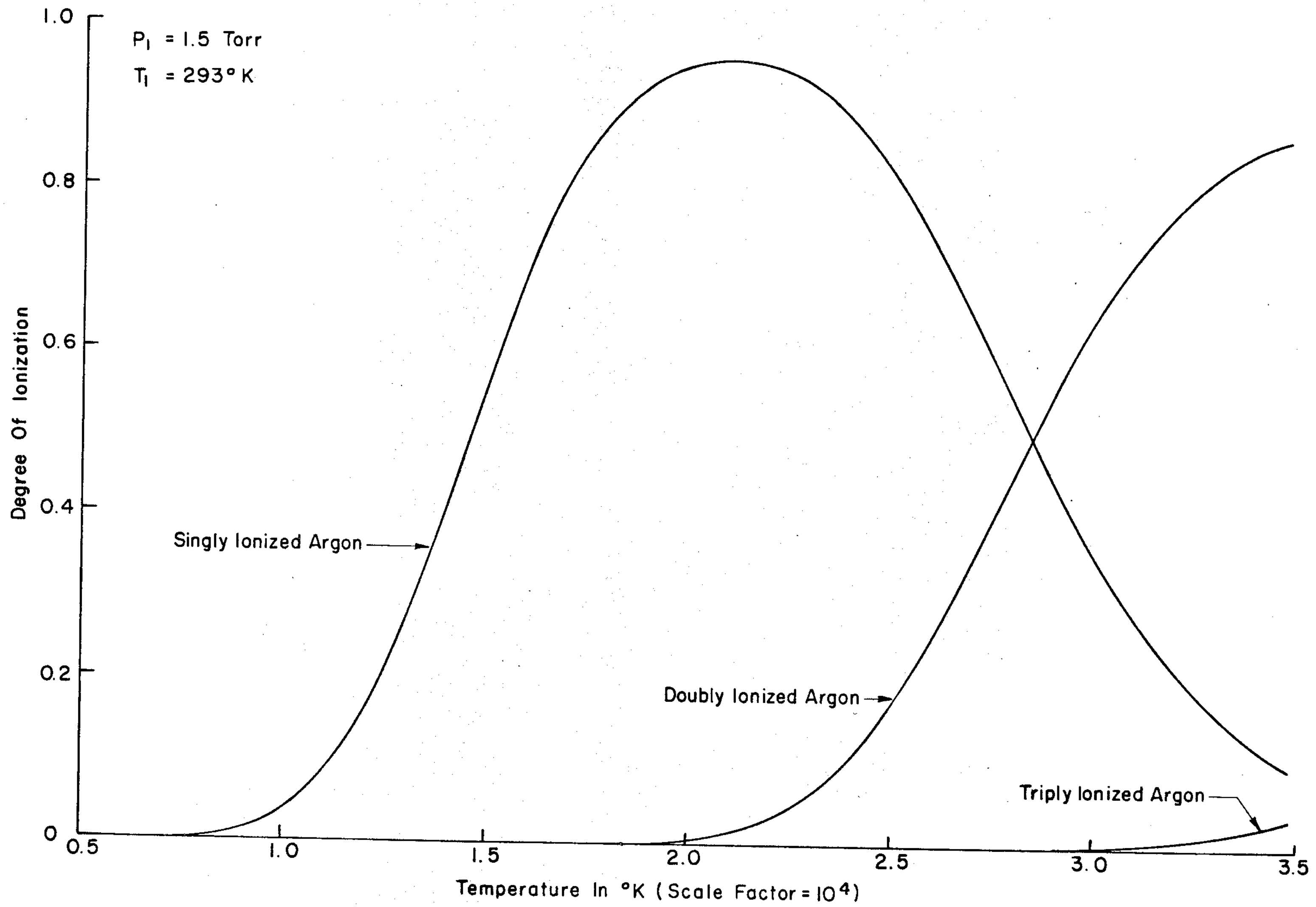

FIG. 38 DEGREE OF IONIZATION VS TEMPERATURE FOR A MULTIPLY IONIZED ARGON PLASMA

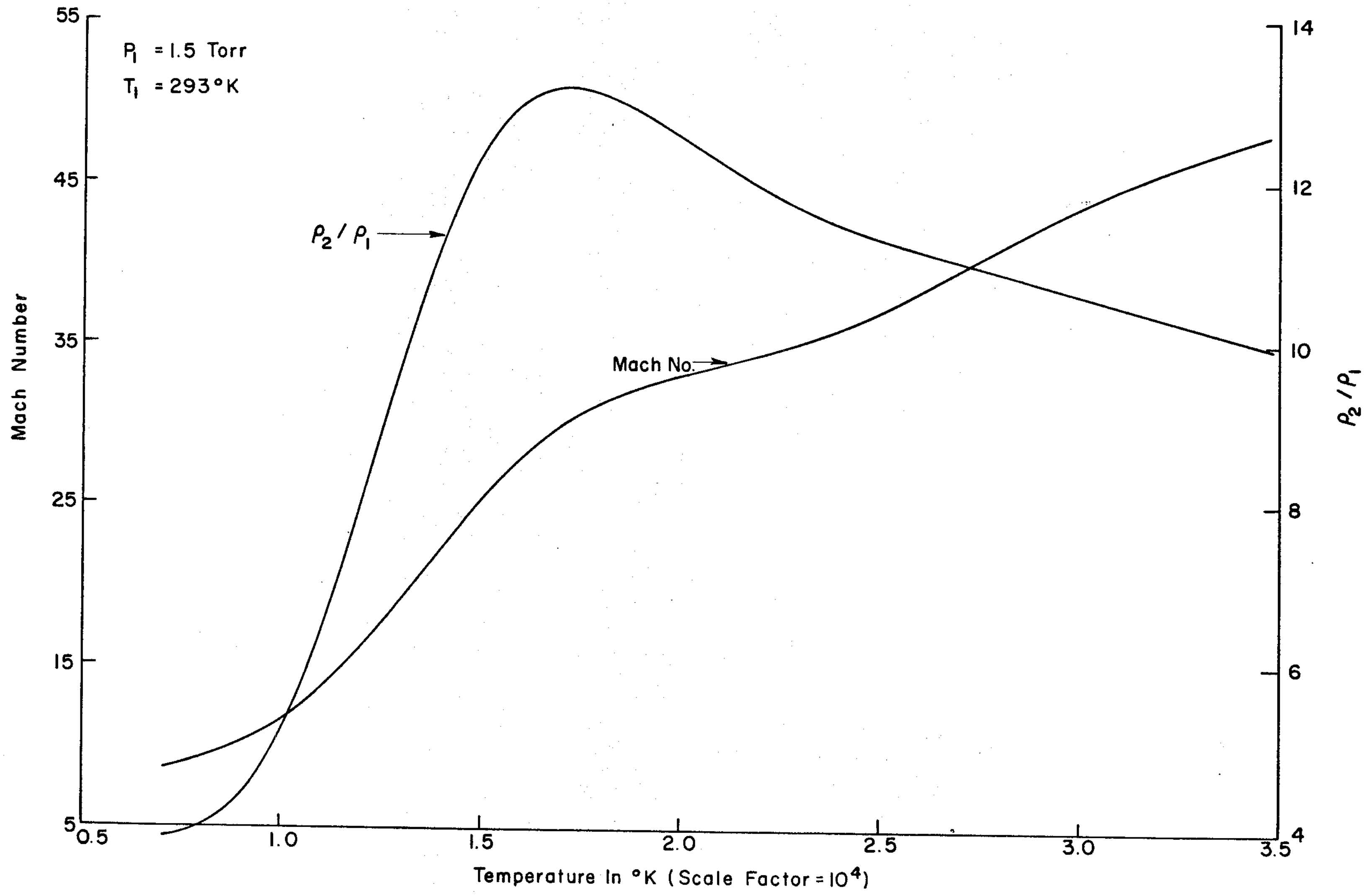

FIG. 39 MACH NUMBER AND ρ_2 / ρ_1 VS. TEMPERATURE FOR A MULTIPLY IONIZED ARGON PLASMA